2016

Rational Design and Synthesis of Pt/Silica-Alumina Metal-Acid Bifunctional Catalysts

Jadid Ettaz Samad
University of South Carolina

Rational design and synthesis of Pt/silica-alumina metal-acid bifunctional catalysts

by

Jadid Ettaz Samad

Bachelor of Science
Bangladesh University of Engineering and Technology, 2008

Master of Science
University of Alberta, 2010

Submitted in Partial Fulfillment of the Requirements

For the Degree of Doctor of Philosophy in

Chemical Engineering

University of South Carolina

2016

Accepted by:

John R. Regalbuto, Major Professor

Jochen Lauterbach, Committee member

Jason Hattrick-Simpers, Committee member

Thomas Vogt, Committee member

John Weidner, Committee member

Lacy Ford, Senior Vice Provost and Dean of Graduate Studies

Dedication

Dedicated to my wife, Minara Mowshumi. She never liked chemistry/chemical engineering until she married me. Also to my parents, Dr. Abdus Samad and Mahfuza Bulbul. They hoped that I would be a medical doctor. But they let me pursue my own interest.

Acknowledgements

I would like to begin by expressing my appreciation to my advisor, Dr. John R. Regalbuto for taking me in and believing in me. Under his supervision, scientific research has been impactful and exciting and I felt every bit of it. Also I have been honored and grateful to have worked under the supervision of Dr. Catherine Louis, Dr. Juliette Blanchard and Dr. Céline Sayag at Université Pierre et Marie Curie (UPMC) in Paris, France. Their guidance and help have broadened my research perspective, enhanced my expertise, and improved my judgment and ability to solve research problems.

I would also like to thank my committee members, Dr. Jochen Lauterbach, Dr. Jason Hattrick-Simpers, Dr. Thomas Vogt and Dr. John Weidner for agreeing to review my work and for their valuable inputs on my dissertation.

I would like to make special mention of my colleagues. For their seamless sharing of expertise, enthusiasm for research, vigilance and team work the research group has been very cohesive, interactive, and productive and definitely one of the best I have ever worked with. Last but not the least, I would like to acknowledge Dr. Shuguo Ma for his XPS expertise, Dr. Ke-Bin Low at University of Illinois at Chicago for his expertise in microscopy and a group of extremely talented undergraduate students I have worked with.

Abstract

In the domain of rational catalyst design and synthesis, Strong Electrostatic Adsorption (SEA) has been applied with tremendous potential and use. In this study, SEA method has been advanced to thick slurries as well as to mixed oxide systems with a view to synthesizing stable, active and selective catalysts fine-tuned for specific applications.

The main objective was to synthesize metal-acid bifunctional catalysts with controlled ratio and proximity between metal and acid sites in order to analyze their effects on a bifunctional reaction. At first, the difference in charging behavior of silica and alumina in solution was used to selectively deposit Pt onto different domains of silica-alumina mixed oxides (Al-Si). With cationic Pt precursor at neutral to basic pH range, well dispersed Pt/Al-Si catalysts with "atomic scale" intimacy between metal and acid sites were prepared. However, anionic Pt adsorption over Al-Si at low pH resulted in poorly dispersed Pt/Al-Si catalysts with "nanometer scale" intimacy between active sites. In this case it was found that as anionic Pt selectively deposited onto the alumina domains of Al-Si, a critical domain size of alumina was required to stabilize small Pt nanoparticles. These catalysts along with other physically mixed and layered catalysts constituted a series of bifunctional Pt/Al-Si catalysts with varying ratio and proximity between metal and acid sites which were tested in an n-heptane (n-C_7) isomerization reaction operating at 350°C and atmospheric pressure.

From the catalytic results, large (~20nm) Pt particles over acidic silica-alumina catalysts with "nanometer-scale" proximity displayed a higher degree of bifunctionality

than small Pt particles (~2nm) with “atomic-scale” intimacy. Even more significant is the ratio of acid sites to metal sites. For optimum bifunctional reactivity for n-C_7 isomerization, Pt and amorphous Al-Si based catalysts should be synthesized with a high enough ratio of acid-to-metal sites (>10 acid sites per metal site) and an intermediate degree of intimacy (not atomic-scale but nano- or micrometer-scale) between these two active sites.

Table of Contents

Acknowledgements iv

Abstract v

List of Tables x

List of Figures xii

Chapter 1: Synthesis of Pt catalysts over thick slurries of oxide supports by Strong Electrostatic Adsorption (SEA) 1

1.1 Introduction 1

1.2 Art of catalyst preparation 5

1.3 Theoretical effect of ionic strength on SEA 9

1.4 Experimental methods 14

1.5 Results 21

1.6 Discussion 33

1.7 Conclusions 38

1.8 Future work 40

Chapter 2: Determining surface composition of mixed oxides with pH 41

2.1 Introduction 41

2.2 Characterization of mixed oxide surfaces 44

2.3 EPHL method and oxide charging parameters 45

2.4 Theory behind 2-surface model 46

2.5 Materials and methods 48

2.6 Results and Discussion 51

2.7 Conclusion 58

2.8 Future work 59

Chapter 3: The controlled synthesis of metal-acid bifunctional catalysts: Selective Pt deposition and nanoparticle synthesis on amorphous aluminosilicates 60

3.1 Introduction 60

3.2 Synthesis of mixed oxides for heterogeneous catalysis 63

3.3 Metal deposition strategies over mixed oxides 63

3.4 Potential of SEA over mixed oxides 65

3.5 Materials and Methods 66

3.6 Results 73

3.7 Discussion 87

3.8 Conclusion 95

3.9 Future work 96

Chapter 4: Effect of the balance and proximity between active sites in selectively deposited Pt over silica-alumina catalysts 97

4.1 Introduction 97

4.2 Bifunctional reaction mechanism 101

4.3 Factors influencing bifunctionality: ideal bifunctional catalyst 102

4.4 Materials and methods 104

4.5 Results 107

4.6 Discussion 116

4.7 Conclusions 123

4.8 Future work 124

References 125

Appendix A : Matlab codes for theoretical models 134

Appendix B: XPS enigma: Where is the alumina 143
Appendix C: Anionic platinum adsorption on boehmite 149
Appendix D: Further characterization on aluminosilicates 151
Appendix E: Additional STEM images 153

List of Tables

Table 1.1. Experimental schemes of this study. 4

Table 1.2. Different catalyst preparation techniques addressed in this study. 8

Table 1.3. Description of materials used in this study. 15

Table 1.4. Pore volume and incipient wetness surface loading (IWSL) of supports used. 19

Table 1.5. Parameters used to study adsorption of SEA at increasing SLs..... 22

Table 1.6. Summary of theoretical (RPA) and experimental (Exp.) maximum Pt uptake (μmoles/m^2) and corresponding Pt loading (wt%) at different SLs (m^2/liter). 27

Table 1.7. Pt nanoparticle sizes of Cl^- doped Pt/silica catalysts. 31

Table 2.1. Properties of oxide materials used in this study. 49

Table 2.2. Components of physical mixtures used in this study. 49

Table 2.3. Critical parameter (PZC, ΔpK, N_s) values used in this study. 51

Table 2.4. Estimation of alumina surface coverage [area%] of composites. 57

Table 3.1. Experimental schemes of this study. 62

Table 3.2. Different materials, their specifications and purpose. 66

Table 3.3. Physico-chemical characteristics of Al-Si supports. 76

Table 3.4. Parameters obtained from Langmuir isotherm in Figure 3.8. 82

Table 3.5. Characteristics of 0.7wt% Pt/Al-Si catalysts. 84

Table 3.6. Estimation of alumina surface coverage of Al-Si by different techniques. 88

Table 4.1. Experimental schemes of this study. 100

Table 4.2. Characteristics of Pt/Al-Si catalysts and results of n-C_7 conversion. 105

Table 4.3. n-C_7 transformation data on PM and L-1 to L-3 catalysts. 113

Table B.1. List of silica and alumina samples used. 144

List of Figures

Figure 1.1. Schematics and attributes of two different SEA setups: (a) typically used thin slurry setup and (b) thick slurry setup addressed in this study. 3

Figure 1.2. Steps and purview of SEA synthesis: (a) Oxide support with excess impregnating solution, (b) Charging chemistry of metal oxides in solution, (c) pH shift of silica due to buffering effect (PZC determination: EPHL method) [6], (d) Cationic metal adsorption with hydration layers over negatively charged silica surface, (e) $Pt(NH_3)_4^{2+}$ adsorption survey over silica with RPA model predictions [6], (f) STEM image showing highly dispersed Pt over silica (scale bar 20nm) [2]. 6

Figure 1.3. Metal precursor adsorption survey versus pH_f at increasing SLs. (a) $PtCl_6^{2-}$ over alumina, (b) $Pt(NH_3)_4^{2+}$ over silica, (c) $Pt(NH_3)_4^{2+}$ over titania and (d) $Ru(NH_3)_6^{3+}$ over silica. RPA model predictions are presented with solid lines. Error in uptake measurement via ICP $\leq \pm$ 10%..... 24

Figure 1.4. RPA model prediction versus measured metal uptake using $Pt(NH_3)_4^{2+}$ at different NaCl concentrations (SL=500m^2/liter, pH_i=12.0)..... 25

Figure 1.5. UV-Vis spectra of $Ru(NH_3)_6^{3+}$ solution. Different colored lines represent different pH and concentration combinations. pH4.6/170ppm (Green), pH 12/170ppm Ru (Red), pH4.6/1700ppm Ru (Blue), and pH12/1700ppm (Black). pH=4.6 is the natural pH for $Ru(NH_3)_6^{3+}$ precursor solution. pH=12 was adjusted using NaOH. 26

Figure 1.6. XRD patterns of (a) γ-alumina supported and (b) silica supported Pt catalysts synthesized at high SLs. Pt loadings from top to bottom in (a) are 0%, 5.4% and 3.7% whereas Pt loading on (b) is 5.0wt% (see Table 1.6). SL values in the labels are in m^2/liter..... 28

Figure 1.7. XRD patterns of reduced 5wt% Pt/silica catalysts prepared at various SL with either a washing step (labeled as "SL= #") or a Cl^- free precursor (labeled as "SL = # (-OH)"). SL values are in m^2/liter. k represents ×1000. 29

Figure 1.8. A representative STEM image of 5wt% Pt/silica catalyst using $Pt(NH_3)_4(OH)_2$ precursor at SL = 25,000m^2/liter along with histogram showing particle size distribution. 29

Figure 1.9. XRD patterns of 5wt% Pt/silica catalysts synthesized via CEDI using (a) different combinations of precursor complex and base as labeled and (b) $Pt(NH_3)_4(OH)_2$ precursor, NH_4OH base and different concentrations of anions (Cl^-, NO_3^-) as labeled. 31

Figure 1.10. Representative STEM images with particle size and distributions of 5wt% Pt/silica catalysts synthesized via CEDI using $Pt(NH_3)_4(OH)_2$ precursor, NH_4OH base and with (a) 0wt% and (b) 0.25wt% Cl^-. 32

Figure 1.11. TPR profiles of different ion doped (Cl^- or NO_3^-) and $Pt(NH_3)_4(OH)_2$ adsorbed samples (5wt% Pt). 33

Figure 1.12. Particle size of silica support Pt nanoparticles with respect to the atomic ratio of Cl and Pt. Except those marked otherwise, Pt loading on all samples is 5wt%... 38

Figure 2.1. Determination of surface composition of mixed oxide using 2-surface model..... 43

Figure 2.2. Simplistic depiction of a physical mixture of alumina and silica immersed in an aqueous solution where $PZC_{silica}<pH<PZC_{alumina}$..... 47

Figure 2.3. pH shift data over pure silica and pure alumina samples at different surface loadings (500 and 12,500m^2/l) : (a) HA, (b) LA, (c) HS and (d) LS. Experimental data were best fitted with model 3P to obtain values of three surface parameters (ΔpK, N_k and PZC)..... 52

Figure 2.4. PZC vs. nominal Al_2O_3 mass fraction plots comparing simulation results with experimental data for (a) HH, (b) HL and (c) LH physical mixture sets..... 53

Figure 2.5. Actual and simulated ASC values of alumina for (a) HH, (b) HL and (c) LH physical mixtures of alumina and silica. Charging parameter (ΔpK, N_k and PZC) values were obtained from 3-parameter (3P) optimization for corresponding mixture components as listed in Table 2.3 and already used to obtain Model_3P plots in Figure 2.3. Z values obtained from Equation 2.8 for corresponding ASC are also plotted. XPS was used for LH sample only and the data is presented in (c). 54

Figure 2.6. (a) Physical mixture data obtained by Schwarz group [49] simulated using 2-surface model with N_s=2.7 , ΔpK=5.18 (for alumina) and N_k=1, ΔpK=0.68 (for silica). (b) Physical mixture of alumina and tungsten oxide data of Schwarz group [48] simulated using 2-site model with N_k=2.7, ΔpK=5.18 (for alumina) and N_k=10, ΔpK=1 (for tungsten oxide). Values of the critical parameters were extracted from the respective studies. 55

Figure 3.1. (a) Theoretical surface potential versus adsorption pH (pH_f) plot for silica (PZC = 4.25) and alumina (PZC = 8.0). Theory (pH shift model) has been elaborated in Chapter 1. (b) Simplistic depiction of selective metal ion adsorption over silica-alumina mixed oxide (Green patches are alumina domains deposited over red silica particles)..... 61

Figure 3.2. Schematic diagram showing recipe to synthesize Al-Si..... 68

Figure 3.3. Pt complex adsorption surveys over pure and physical mixtures of silica (S) and alumina (A): (a) Anionic $PtCl_6^{2-}$ over single oxides, (b) cationic $Pt(NH_3)_4^{2+}$

over single oxides, (c) Anionic $PtCl_6^{2-}$ over physical mixtures and (d) Cationic $Pt(NH_3)_4^{2+}$ over physical mixtures. Initial ppm (mg/L) concentration of Pt present in the solution for each experiment is included in the legend. Dashed lines in (c,d) represent data extrapolated from single oxide uptakes. Two red arrows indicate selected samples (open diamonds) that were analyzed with STEM. 74

Figure 3.4. STEM images of (a) $PtCl_6^{2-}$ (3.7wt% Pt, pH_f=3.9) and (b) $Pt(NH_3)_4^{2+}$ (0.7wt% Pt, pH_f=8.3) over 1:1 physical mixtures. Inset of Figure (a) shows images of contrasting sizes of model and nonporous alumina (A) and silica (S) particles. 76

Figure 3.5. (a) XRD and (b) NH_3-TPD desorption profiles of pure oxides and Al-Si samples. Patterns are ordered with respect to increasing alumina content from top to bottom. 77

Figure 3.6. (a) STEM micrograph of AlSi-50. (b-c) Elemental maps of Si (b) and Al (c) of the bounded area shown in (a). (d) ^{27}Al NMR profiles of synthesized (AlSi-380) and commercial (SIRAL 80) Al-Si. 79

Figure 3.7. Anionic $PtCl_6^{2-}$ (A) and cationic $Pt(NH_3)_4^{2+}$ (B) adsorption onto (I) AlSi-50, (II) AlSi-380 and (III) Commercial (SIRAL) supports. Initial Pt concentration = 200ppm (mg/L). SL=1000m^2/liter. For comparison, the platinum complex uptakes on 100% silica (Aerosil 380 used for part BIII) and on 100% alumina (Al-1) have also been represented. 81

Figure 3.8. (a) Raw data and (b) linear fitting plots of Langmuir isotherms for $PtCl_6^{2-}$ adsorption over pure alumina (Al-1) and over Al-Si supports. 82

Figure 3.9. XRD patterns of 0.7% Pt/Al-Si catalysts over (I) AlSi-50, (II) AlSi-380 and (III) SIRAL 80 supports from a) PTA deposition at neutral pH (series a), b) PTA SEA at high pH (series b), c) $Pt(NH_3)_4Cl_2$ deposition via DI (series c), and d) $PtCl_6^{2-}$ SEA at low pH (series d). 85

Figure 3.10. STEM images of 0.7% Pt over (a) AlSi-50 using $Pt(NH_3)_4^{2+}$ at pH_f=11.9 (series b), (b) AlSi-50 using $PtCl_6^{2-}$ at pH_f=4.4 (series d), (c) SIRAL 80 using $PtCl_6^{2-}$ at pH_f=4.2 (series d) and (d) SIRAL 20 using $PtCl_6^{2-}$ precursor pH_f=4.2 (series d). Inset of figure (b), (c) and (d) shows high magnification images (scale bar=5 nm). 86

Figure 3.11. Non-electrostatic (presumably, IE) cationic $Pt(NH_3)_4^{2+}$ uptakes (open circles) over (a) SIRAL 80, (b) SIRAL 70, (c) SIRAL 40 and (d) SIRAL 20 supports. Other data points represent acid sites by NH_3-TPD measured at different pH for each Al-Si support (metal free). 90

Figure 3.12. Al, Pt and Si elemental mapping of 0.7% Pt ($PtCl_6^{2-}$) over AlSi-50. As a guide to the eye, the contour of the platinum particle has been drawn from the Pt elemental mapping card and reported on the Al elemental mapping card (dashed green line). 92

Figure 3.13. Dispersion (chemisorption) of 0.7% Pt (prepared using $PtCl_6^{2-}$) over γ-alumina (Al-1) and Al-Si supports with respect to the size of alumina domains obtained from XRD. For the Si-rich Al-Si supports, the size of the alumina domains has been arbitrarily set to 1 nm as it could not be evaluated using XRD). Adsorption constants (K_{ads}) have been added on the secondary Y-axis. 93

Figure 4.1. Schematics of catalysts used in this study showing different degree of intimacy between active sites. Images are not drawn to scale. 99

Figure 4.2. Simplified classical mechanism for isomerization of n-alkane on a metal-acid bifunctional catalyst. 101

Figure 4.3. NH_3-TPD profiles of all Pt/Al-Si catalysts synthesized on (a) AlSi-380, (b) SIRAL 80, (c) SIRAL 40 and (d) SIRAL 20 support. 108

Figure 4.4. Total number of acid sites (NH_3-TPD) of 0.4wt% and 0.7wt% Pt/Al-Si catalysts synthesized at different conditions (precursor, pH): (a) Synthesized from AlSi-380 and (b) from Commercial SIRAL 80. 108

Figure 4.5. Product distribution (at 22 ± 3% conversion) of silica and Si-rich Al-Si catalysts using (a) Si-50, AlSi-50, (b) AlSi-380 and (c) SIRAL 80 as support. Product color coding: i-C_7 (Green), toluene (Black), cyclic (Red) and <C_7 (Blue). "o" with solid lines representing 0.7wt% and "x" with dashed lines representing 0.4wt% catalyst. 109

Figure 4.6. Product distribution for n-C_7 conversion (at 22 ± 3% conversion) of Al-rich (a) SIRAL 40 and (b) SIRAL 20 supported 0.7wt% catalysts synthesized at different conditions. 111

Figure 4.7. Product distributions obtained for different two-component catalysts based on Pt/Si-50 and SIRAL 80 (Al-Si). Schematic diagram on top of each sample data is showing components and their degree of intimacy. Yellow circles in the schematics represent acidic SIRAL 80 (Al-Si) and red circles represent Pt/Si-50. Total catalyst mass for 1:1 PM and layered catalysts were 0.4g with equal mass (~0.2g) of components. For reference catalysts, total mass of catalyst was ~0.2g (Exact masses are listed in Table 2). 113

Figure 4.8. (a) Conversion and (b) product selectivity of PM catalysts with different mass ratios of Pt/Si-50 and SIRAL 80 (Al-Si) components. Total mass of catalysts = 0.2g and selectivity data obtained for 22±3% conversion. 115

Figure 4.9. Representative high STEM images of 0.75% Pt/AlSi-50 (PTA-11) catalyst: (a) fresh catalyst, (b) after TOS=18h. Volume (D_v), surface (D_s) and number (D_n) averaged particle sizes have been included along with histograms showing distribution of metal particle size. 116

Figure 4.10. Product selectivity of all catalysts as functions of acid to metal ratio toward (a) toluene, (b) i-C_7, (c) cyclic and (d) <C_7. The legend in (a) is common to all..... 118

Figure 4.11. TOF (per active metal site) of i-C_7 products with respect to acid-to-metal ratio. TOF determined using conversion and selectivity of i-C_7 at 1.0h^{-1} space velocity, TOS=18h, H_2/n-C_7 = 33. Both axes are logarithmic..... 121

Figure 4.12. Product (i-C_7 and <C_7) selectivity and Pt dispersion of SIRAL Al-Si supported (a) CPA-4 and (b) PTA-11 catalysts with 0.7wt% Pt. 123

Figure B.1. Discrepancy in XPS estimation when HA is present in physical mixtures of silica and alumina. 144

Figure B.2. XPS estimation of surface coverage of silica-titania and alumina-titania physical mixtures. HA alumina with titania once again showed significant discrepancy. 145

Figure B.3. Discrepancy between nominal and XPS surface coverage for pretreated HA: HA-HS* = HA pretreated at 1200°C for 24h. Surface area reduced from 159 to 40m^2/g. Pellet-top/bottom/center = HA-HS physical mixtures pelletized and surface of the pellet gradually scraped off to expose surface at different depths. Meshed = HA and HS meshed between 75-105micron size and physically mixed. 145

Figure B.4. XRD patterns of different compositions of HA-HS with intensities of silica and alumina peaks commensurate with respective composition. Nominal surface compositions [wt%] are included with each label. 146

Figure B.5. XPS spectra of HA and LA alumina showing significantly low Al2p and Al2s signal intensity (Counts per second, CPS) for HA. 147

Figure B.6. SIMS plots of HA-HS (left) and LA-HS (right) physical mixtures showing low Al signal in HA-HS. 148

Figure B.7. Deconvulation of O1s peaks of (left) HA-HS (80% alumina by surface) and (right) LA-HS (40% alumina by surface) physical mixture showing contributions from Al and Si. 148

Figure C.1. XRD patterns of different Pt-free and Pt-loaded uncalcined (UC-Boh) and calcined (C-Boh) samples. 150

Figure C.2. $PtCl_6^{2-}$ adsorption uptake survey over uncalcined and calcined boehmite and γ-alumina. 150

Figure D.1. XRD patterns of uncalcined (prior to activation to γ-alumina phase) SIRAL Al-Si composites showing presence of boehmite phase. Post-calcination patterns are included in main text. 151

Figure D.2. NH_3-TPD patterns of SIRAL 80 –SIRAL 20 treated at different pH..... 151

Figure D.3. XRD patterns of Al-rich SIRAL composites and catalysts synthesized over them. 152

Figure E.1. Elemental mapping image # 1..... 153

Figure E.2. Elemental mapping image # 2..... 154

Figure E.3. Elemental mapping image # 3..... 154

Chapter 1

Synthesis of Pt catalysts over thick slurries of oxide supports by Strong Electrostatic Adsorption (SEA)

1.1 Introduction

Dominated by more of an alchemy rather than scientific approach, synthesis of supported metal catalysts has long been the most underrated aspect in the study of heterogeneous catalysis. This has often limited the reproducibility, control and understanding of such catalysts and their performance. In addition to that, different industrial catalytic processes impose contradictory demands from the catalytic materials. A carefully designed synthesis step holds key to meeting these demands as even a minor alteration in preparative detail could bring about drastic changes to the catalytic properties. Bearing these in mind, a sound emphasis on the preparation step with scientific and systematic approach could greatly assist in a catalyst manufacturer's quest for a stable, active, selective and yet least expensive catalyst.

Till date impregnation remains the simplest, cheapest and, understandably so, the most widely used method of catalyst synthesis [1]. Among several different impregnation techniques dry impregnation (DI), often referred to as incipient wetness impregnation (IWI), is the simplest and the quickest. However, with little or no interaction between support and metal, this method often falls short in delivering well-dispersed, uniformly sized, small supported metal nanoparticles [1]. Poor dispersion (a commonly used metric representing the efficiency of metal utilization) of precious metal over support can affect

the economics of the process. A modified wet impregnation approach e.g., strong electrostatic adsorption (SEA), on the other hand, excels on that front by maintaining a strong interaction between metal and support [2].

Unifying the concept of SEA and the simplistic nature of DI, a new method called charged enhanced dry impregnation (CEDI) has been introduced lately [3, 4]. While dispersion of metal nanoparticles drastically improved in this method (compared to DI) with significant reduction in catalyst preparation time and metal loss (compared to SEA), several questions remain. In Figure 1.1 schematic diagrams of thick and thin slurry SEA systems have been depicted along with factors affecting their use. In a typical SEA setup, low slurry thickness is generally used to limit the ionic strength of the impregnating solution. Moreover, an excess solution in this case makes it reasonably easier to remove residual ions via simple filtration. However, in CEDI setup maximum slurry thickness is used which increases ionic strength that could thereby retard electrostatic adsorption. Such retardation effect could be envisaged using Revised Physical Adsorption (RPA) model originally proposed to simulate SEA uptake surveys for different metal precursor-support combination [5, 6]. Keeping this in mind, so far for CEDI demonstration, only low metal loadings (lower than the metal adsorption capacity at low slurry thickness) have been used [4]. This could potentially limit the applicability of CEDI method in many applications e.g., electrochemistry where high metal loading is a requisite [3]. Moreover, due to the added complexity in removing residual ions from thick slurries, their roles on final metal particle size need to be carefully considered.

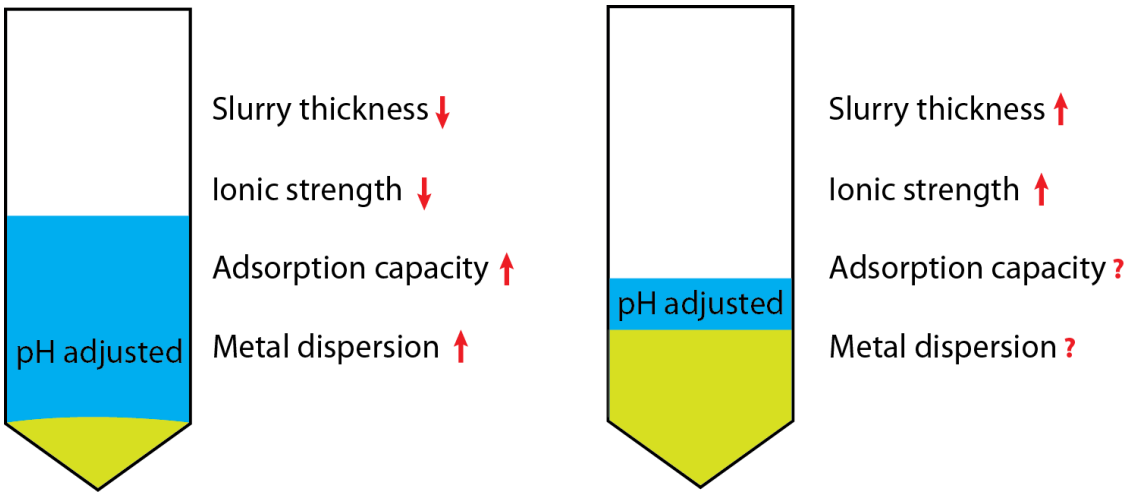

Figure 1.1. Schematics and attributes of two different SEA setups: (a) typically used thin slurry setup and (b) thick slurry setup addressed in this study.

In order to elucidate the role of high slurry thickness and residual ions in electrostatic adsorption, following objectives were considered:

1. Development of metal precursor uptake versus pH surveys using anionic and cationic metal precursors over different supports at elevated slurry thicknesses and comparison with theoretical RPA model predictions.
2. Characterization of final reduced catalysts obtained from each different slurry thickness.
3. Control the presence of residual ions and monitor the resulting effect on metal adsorption and final metal particle size.

For objective 1, two separate sets of metal precursor uptake versus pH surveys were performed using anionic and cationic Pt precursors. To favor electrostatic adsorption, supports (e.g., silica, titania) with low to intermediate point of zero charge (PZC) were used for cationic Pt adsorption whereas high PZC support (e.g., alumina) was used for anionic Pt adsorption. Uptake surveys were conducted at different slurry thicknesses quantified

using the metric represented as "surface loading (SL)" which is basically m^2 of support surface added to each liter of impregnating solution. For theoretical model predictions, the established RPA model was coded to predict adsorption uptake at different SLs. Resulting selected Pt adsorbed samples were directly reduced and characterized for metal particle size in order to accomplish objective 2. Finally, for objective 3, the role of residual ions on adsorption uptake and final metal particle size was further investigated by varying their concentrations in different samples before/after metal adsorption via salt doping/pH adjusted washing. In order to accomplish each one of the objectives, experiments were planned and performed as outlined in Table 1.1.

Table 1.1. Experimental schemes of this study.

Objective(s)	**Experiment(s)**	**Expected outcome(s)**
1	Cationic and anionic Pt precursor uptake (measured using ICP-OES) versus pH surveys over silica, titania and alumina at SL= 500-100,000m^2/liter	Experimental verification of the effect of SL on SEA adsorption as predicted by theoretical RPA model
2	Characterization of the final catalysts using (a) XRD, (b) chemisorption and (c) STEM	Evaluation of metal dispersion and particle size
3	(a) Adding controlled dosage of NaCl salt prior to metal adsorption and (b) pre-reduction washing of residual ions	Understanding the effect of residual ions on metal adsorption and particle size

<u>The main contributions of this research are:</u>

(1) Synthesis of Pt/silica catalyst with high metal loading and at high slurry thickness via SEA.

   a. Journal publication:
   Samad, J. E., Hoenig, S., & Regalbuto, J. R. (2015). Synthesis of Platinum Catalysts over Thick Slurries of Oxide Supports by Strong Electrostatic Adsorption. *ChemCatChem, 7*(21), 3460-3463.

(2) A softer approach to control metal particle size by doping salt.

1.2 Art of catalyst preparation

Significant progress in the synthesis of heterogeneous catalyst has been made since Brunelle postulated in his pioneering work that away from the point of zero charge (PZC) metal oxides would electrostatically adsorb charged noble metal complexes [3, 7-10]. Other landmark works on the fundamentals of catalyst preparation could be credited to Contescu and Vaas and Schwarz [11, 12]. With cationic/anionic Pd precursor Contescu and Vaas demonstrated electrostatic adsorption over alumina at high/low pH. Schwarz and his group reported pH dependent anionic Pt uptake over alumina for the first time in literature. All these works stand out as early contributions on the transformation of the art of catalyst synthesis into science.

1.2.1 Strong Electrostatic Adsorption (SEA)

Inspired by Brunelle's work, a scientific method to synthesize heterogeneous catalyst, known as strong electrostatic adsorption (SEA), was established where metal uptake on support can be predicted with reasonable accuracy through a simple revised physical adsorption (RPA) model [6, 13, 14]. Concept of SEA stems from the basic principle of attraction between oppositely charged ions. In the realm of catalyst synthesis via SEA, metal precursor ions and charged oxide surfaces act as opposite charges. This establishes strong metal-support interaction, which ultimately improves metal dispersion of the final catalyst. This method has been successfully applied to synthesize highly dispersed metal nanoparticles on a variety of oxide and carbon supports [15-19].

Different steps involved in SEA synthesis method have been illustrated in Figure 1.2. Overall, the concept of SEA applied in catalyst synthesis can be divided into two parts:

(a) determination of the point of zero charge (PZC) of oxide supports and (b) electrostatic adsorption of metal precursor ions on support.

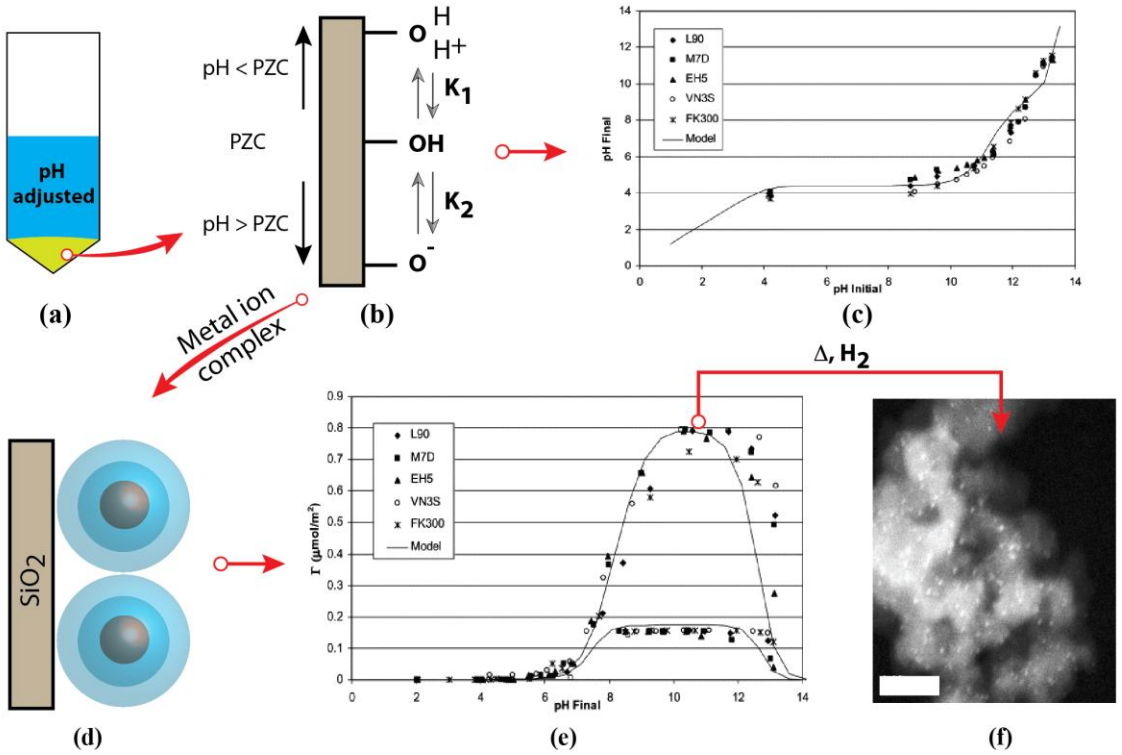

Figure 1.2. Steps and purview of SEA synthesis: (a) Oxide support with excess impregnating solution, (b) Charging chemistry of metal oxides in solution, (c) pH shift of silica due to buffering effect (PZC determination: EPHL method) [6], (d) Cationic metal adsorption with hydration layers over negatively charged silica surface, (e) $Pt(NH_3)_4^{2+}$ adsorption survey over silica with RPA model predictions [6], (f) STEM image showing highly dispersed Pt over silica (scale bar 20nm) [2].

The concept of charging of metal oxide surfaces stems from the fact that these oxides have terminal hydroxyl groups (Figure 1.2b). This enables them to buffer aqueous solution to their (oxides) respective point of zero charge (PZC), which represents charge neutrality of the surface. As a result, for an initial pH (pH_i) higher/lower than the PZC these hydroxyl groups deprotonate/protonate which ultimately shifts the final pH (pH_f) of the solution towards the PZC. If a pH_f versus pH_i plot is developed for different oxides, due to the aforementioned buffering ability of the oxides, a plateau forms at the PZC. This plot is

commonly referred to as a pH shift plot (Figure 1.2c). However, the buffering ability of oxide surface is also proportional to oxide loading in solution. Higher the mass or, in other words, thicker the slurry, the pH of solution would more easily and accurately approach the PZC. As a result, pH shift plot at high oxide loadings or high slurry thicknesses yields a much wider plateau, more accurately placed at the PZC [20]. This has been shown to be quite a useful technique for PZC determination of oxides and is known as Equilibrium pH at high oxide loading (EPHL) method.

However, to facilitate electrostatic adsorption, oxide surface should be charged and understandably so, it is necessary for the pH_f to be away from PZC. This renders the study of pH shift along with PZC vital for catalyst preparation via SEA. Nevertheless, as the hydroxyl groups on oxide surface deprotonates/protonates and becomes negatively/positively charged at pH above/below the PZC, it enables cationic/anionic metal precursor to adsorb electrostatically on the charged oxide surface. As the pH is increased/decreased further away from PZC, surface charge is enhanced and so does the adsorption of metal precursor ions. Eventually the adsorption capacity reaches a maximum, the value of which is dictated by the closed packed geometry of metal ion precursor retaining one or two hydration sheaths (Figure 1.2d) [21]. It was initially suggested that cationic and anionic metal precursor ions retain two and one layers of hydration respectively. However, cationic precursors e.g., $Ru(NH_3)_6^{3+}$ (single hydration sheath [22]) and anionic precursors e.g., $PdCl_4^{2-}$, $PtCl_4^{2-}$ (double hydration sheaths [23, 24]) show opposite trend. These observations suggest that geometry of the metal precursor complex could have further influence on the number of hydration sheaths that the complex retains. In this vein of thought, both $PtCl_6^{2-}$ and $Ru(NH_3)_6^{3+}$, albeit being oppositely charged, retain

single hydration sheath due to their similar octahedral geometry. On the other hand, square planar complexes e.g., $PtCl_4^{2-}$, $PdCl_4^{2-}$, $Pt(NH_3)_4^{2+}$ all retain two hydration sheaths. Nevertheless, cationic Pt precursor e.g., $Pt(NH_3)_4^{2+}$ retaining double hydration sheaths exhibits a maximum adsorption capacity of ~0.84μmoles/m^2 [21]. On the other hand, anionic Pt precursor, $PtCl_6^{2-}$ retains single hydration sheath and hence the maximum adsorption capacity could be as high as 1.6μmole/m^2 [21]. At extreme pH values, however, adsorption is lowered due to high ionic strength at those pHs. Finally, if metal adsorption uptake is normalized by surface area of support, one could see the applicability and reproducibility of SEA method as same oxide with different surface areas would exhibit fairly indistinguishable metal uptake versus pH plots (Figure 1.2e). Finally, due to strong metal-support interaction the resulting catalysts become well dispersed with small metal nanoparticles (Figure 1.2f).

1.2.2 Dry Impregnation (DI)

The catalyst preparation method that is most commonplace in literature and in industry is dry impregnation (DI). In this method, impregnating solution (containing metal precursor ions) sufficient to fill the pore volume of the support is used. This method does not guarantee strong metal-support interaction. However, it is the quickest and simplest method of catalyst preparation with no loss of metals. Table 1.2 compares the characteristics and advantages/disadvantages of different methods.

Table 1.2. Different catalyst preparation techniques addressed in this study.

Features	**SEA**	**DI**	**CEDI**
SL (m^2/liter)	Low (≤1000)	Maximum	Very high
Metal dispersion	High	Not guaranteed	High
Counter-ions	Mostly filtered out	Cannot be filtered, requires HT calcination	May affect adsorption and dispersion
Loss of metal	Yes	No	No

Metal loading	Limited	Unlimited	< SEA (theoretically)
Synthesis difficulty	Consists of several steps	Simplest and quickest	Simpler and quicker than SEA

1.2.3 Charge Enhanced Dry Impregnation (CEDI)

Recently, a simple modification of the DI method which essentially incorporates the concept of SEA has been proposed [4]. The modification appears in the form of pH adjustment prior to support addition in order to charge the oxide surface for electrostatic interaction with the precursor ion. This method, referred to as Charged Enhanced Dry Impregnation (CEDI), offers a number of advantages of DI while maintaining a similar level of performance as SEA (Table 1.2). In several reports, CEDI has been utilized with great success over a series of oxide and carbon supports [3, 23]. However, several questions/disadvantages remain as outlined in Table 1.2. At high surface loadings, as described earlier, due to the greater susceptibility of pH to reach the PZC, extreme pH_is are often required in CEDI to keep the surface charged [23]. Higher concentration of counter-ions appearing from acid/base or the precursor complex and the difficulty of removing them would, in turn, enhance the ionic strength and hence theoretically retard the capacity of the support to electrostatically adsorb precursor metal ions. The theoretical aspect of the influence of this ionic strength over adsorption uptake will be discussed at length next. Nevertheless, because of this underlying cause, significantly lower metal loading than that obtained from SEA (with low SL) had often been aimed with CEDI [23].

1.3 Theoretical effect of ionic strength on SEA

James and Healy first introduced double layer concept to model metal complex ion adsorption over oxide surface in aqueous solution [25]. In the original model, physical interaction was primarily considered and surface potentials for various oxides were

described with Nernstian equation. Free energy term used to describe adsorption was composed of coulombic term (attraction), solvation term (repulsion) and a large adjustable "chemical" free energy term. Several adjustment was later made on the originally proposed model and has been introduced as the Revised Physical Adsorption (RPA) model [26]. Firstly, surface potential of oxide surfaces was described using a more realistic non-Nernstian treatment. Secondly, further revisions that were proposed to determine solvation energy terms were incorporated. With these modifications and further comparing experimental data it was suggested that the coulombic term dominates all other contributions of free energy terms. This term can even be used solely (no solvation energy term) to represent free energy of adsorption with very good agreement with experiment for many systems which renders this RPA model essentially parameter-free [5].

In order to model an SEA system, equations describing both pH shift and RPA model need to be considered (Equation 1.1-1.11). Matlab codes associated to the theory have been included in the appendix (Appendix A.1).

1.3.1 pH shift with CO_2 adsorption

The charging mechanism applied here to simulate pH shift after adsorption has been detailed in the original work of Park and Regalbuto [20]. Four nonlinear equations are used to solve for four variables: surface charge (σ_o), surface potential (Ψ_o), equilibrium concentration of $[H^+]$ and mole fraction of dissolved CO_2 (x_{CO_2}). As described earlier, mineral oxides contain terminal hydroxyl groups which accumulate charge as they come into contact with aqueous solutions. A surface site balance which describes the surface charge as difference between positive and negative charge can be represented by the following equation:

$$\frac{\sigma_o}{F\Gamma_t} = \frac{\frac{[H^+]\exp(-y_o)}{K_1} - \frac{K_2\exp(y_o)}{[H^+]}}{\frac{[H^+]\exp(-y_o)}{K_1} + 1 + \frac{K_2\exp(y_o)}{[H^+]}}$$ **Equation 1.1**

Where,

σ_o = charge on surface k

ε = dielectric constant of solution

$y_o = \frac{e\Psi_o}{2kT}$

k = Boltzman constant

e = electron charge (1.6×10^{-19} C)

T= temperature

Ψ_o=surface potential

Γ_t= density of charged sites (moles/m^2)=$\frac{10^{-5}N_s}{6.02}$

N_s = density of OH groups

K_1, K_2 =ionization constant = $10^{(-PZC \pm 0.5\Delta pK)}$

F=Faraday constant (9.649×10^4 C/mole)

$[H^+]$=equilibrium concentration of H+

Next equation comes from Gouy-Chapman's describing the relation between surface charge and potential:

$$\sigma_o = (8\varepsilon\varepsilon_o kTn_o)^{0.5}\left[\exp\left(\frac{ze\Psi_o}{2kT}\right) - \exp\left(-\frac{ze\Psi_o}{2kT}\right)\right]$$ **Equation 1.2**

Where,

ε_o= permittivity of vacuum (8.854×10^{-12} $C^2/N.m^2$)

n_o = number of ions per unit volume

z = charge of ionic species

Third equation is a proton balance of the liquid phase:

$$\sigma_o = \frac{F}{SL}\frac{\left\{[H^+]_o - [OH^-]_o + 10^{-(14-pH)} - 10^{-pH}\right\}c_o}{\gamma} \quad \textbf{Equation 1.3}$$

Where,

$[H^+]_o$, $[OH^-]_o$ = initial concentration of $[H^+]$, $[OH^-]$

$\gamma = 10^{-0.510\left(\sqrt{I}/(1+\sqrt{I})\right)}$ from extended Debye-Huckel equation

Co = standard concentration (1mol/liter)

I = ionic strength

$$I = \frac{1}{2}\sum (z_i)^2 C = \frac{1}{2}\left([H^+]_o + [OH^-]_o + [H^+] + [OH^-] + 2C_{initial} + z^2 C_i + \sqrt{0.01 x_{CO_2} \times C_{tot} \times K_{H_2CO_3}}\right)$$

Equation 1.3a

K_{H2CO3}=equilibrium constant of H_2CO_3 dissociation

C_{tot}=total concentration of solvent [mol/liter]

x_{CO2}= mole fraction of CO_2

$C_{initial}$ = initial concentration of metal complex in solution

C_i = Equilibrium concentration of metal complex in solution

Fourth equation comes from the fugacity of CO_2 (vapour), which is related to the ionic strength of the solution.

$$f_{CO_2,vap} = x_{CO_2} P_{sat} . \gamma \quad \textbf{Equation 1.4}$$

1.3.2 Adsorption equations: RPA model [6]

RPA model assumes Langmuir isotherm to describe the physical adsorption of cations or anions onto oxide surfaces by the following equation:

$$\Gamma_t = \frac{\Gamma_{max} K_i C_i}{1 + K_i C_i} \qquad \textbf{Equation 1.5}$$

Where,

Γ_{max} = maximum adsorption density based on steric close-packed layer of the adsorbates retaining one (anion) or two (cation) hydration sheaths

K_i = adsorption equilibrium constant

$$\Gamma_{max} = \frac{1}{N_o \pi (r_i + 2nhsr_w)^2} \qquad \textbf{Equation 1.6}$$

Where,

N_o=Avogadro's number

r_i = radius of species i

r_w = radius of water

nhs=number of hydration sheaths retained

Adsorption equilibrium concentration is described by the following equation:

$$K_i = \exp\left(-\frac{\Delta G_{ads}}{RT}\right) \qquad \textbf{Equation 1.7}$$

Where, ΔG_{ads} is simply represented by the columbic term in the parameter-free RPA model:

$$\Delta G_{ads} = z_i F \Psi_{x,i} \qquad \textbf{Equation 1.8}$$

Where,

$\Psi_{x,i}$=potential of i at some distance x found by a Laplace solution of Gouy and Chapman assuming a simple electric double layer according to Equation 9

$$\psi_{x,i} = \left[\frac{2RT}{ZF}\right] \ln\left[\frac{(Y+1)+(Y-1)e^{-\kappa x_i}}{(Y+1)-(Y-1)e^{-\kappa x_i}}\right] \qquad \textbf{Equation 1.9}$$

Where,

$x_i = r_i + 2nhsr_w$

$$Y = \exp\left(\frac{ZF\psi_o}{2RT}\right)$$

κ = Debye-Huckel reciprocal double layer length

κ = function of ionic strength (See Equation 10)

$$\kappa = 3.31 \times 10^9 \sqrt{I} \qquad \textbf{Equation 1.10}$$

Theoretically, as the SL or slurry thickness in SEA system increases, the 1st ($[H^+]_o$) and 2nd ($[OH^-]_o$) terms (representing counter-ions from acid/base) as well as the 5th ($2C_{initial}$) term (representing counter-ions associated with metal complex) in the ionic strength equation (Equation 3a) will increase significantly which in turn will raise ionic strength. Following two limiting conditions could be presented to explain the effect of ionic strength on adsorption according to the RPA model.

[1] (High SL case) **As I** $\rightarrow \infty$, $\kappa \rightarrow \infty$ (Equation 1.10), $\boldsymbol{\Psi_{x,i}} \rightarrow 0$ (Equation 1.9), $\boldsymbol{\Delta G_{ads}} \rightarrow 0$ (Equation 1.8), $\mathbf{K_i} \rightarrow 1$ (Equation 1.7), $\boldsymbol{\Gamma_t} << \Gamma_{max}$ (Equation 1.5)

[2] (Low SL case) **As I** $\rightarrow$ **0**, $\kappa \rightarrow 0$ (Equation 1.10), $\boldsymbol{\Psi_{x,i}} \rightarrow \Psi_o$ (Equation 1.9), $\boldsymbol{\Delta G_{ads}} >> 0$ (Equation 1.8), $\mathbf{K_i} >> 1$ (Equation 1.7), $\boldsymbol{\Gamma_t} \rightarrow \Gamma_{max}$ (Equation 1.5)

1.4 Experimental methods

Experimental schemes for this study have been outlined in Table 1.1. In the next few paragraphs, details about the materials, methods and characterization instruments will be discussed.

1.4.1 Materials

Three different commercial oxide supports in their powder form and without any further purification were used in this study. Chemicals include Pt and Ru complexes (metal

precursor), acid/base (pH adjustment) and 10% in-house gas mixture of H_2 and He. Detail descriptions of these materials are provided in Table 1.3.

Table 1.3. Description of materials used in this study.

Commercial name	**Formula**	**Purpose**	**Supplier, Assay**
SBa200 alumina	Al_2O_3	Support	Sasol, SA=189m^2/g
Aerosil®300 silica	SiO_2	Support	Evonik, SA=330m^2/g
Aerosil®380 silica	SiO_2	Support	Evonik, SA=380m^2/g
Hombikat UV 100	TiO_2	Support	Sachtleben, SA=330m^2/g
Platinum tetraammine chloride hydrate	$Pt(NH_3)_4Cl_2.xH_2O$	Cationic Pt precursor	Aldrich Chem Co., 98%
Platinum tetraammine hydroxide hydrate	$Pt(NH_3)_4(OH)_2.xH_2O$	Cationic Pt precursor	Aldrich Chem Co.,
Chloroplatinic acid	$H_2PtCl_6.6H_2O$	Anionic Pt Precursot	Aldrich Chem Co.,
Ruthenium(III) hexaammine chloride	$Ru(NH_3)_6Cl_3$	Cationic Ru precursor	Aldrich Chem. Co., 98%
Sodium Hydroxide	NaOH	Adjust pH (base)	Ricca Chemical Co., 10N
Ammonium Hydroxide	NH_4OH	Adjust pH (base)	BDH, 5N
Hydrochloric Acid	HCl	Adjust pH (acid)	Sigma Aldrich
Sodium chloride	NaCl	Adjust ion conc.	Fisher Scientific, 1kg, 99.9%

1.4.2 Characterization instruments

1.4.2.1 pH meter

A standard pH electrode (Orion 3-star benchtop) was used with 3-point calibration to record solution pH. Three HACH color-coded pH buffer solutions (pH = 4.0, 7.0, 10.0) were used for calibration. Acceptable electrode slope was set to be 95% or higher. For a slope less than that buffer solutions were discarded and replaced with new solutions and the pH meter was recalibrated. For measurement of pH of the thicker slurries, a special

type of Fisher Scientific accumet® spear tip probe (accuCap) electrode was used along with same as previous buffer solutions for calibration.

1.4.2.2 Inductively Coupled Plasma (ICP-OES)

Pt concentration in solution was measured using a Perkin Elmer Optima 2000DV ICP-OES apparatus with an AS90plus (Parkin Elmer) autosampler. Concentrations measured before and after support addition were used to determine amount of Pt adsorbed (eventually, metal loading of catalyst) on the support[1]. During concentration measurements a 5ppm Y solution was used as internal standard. Mn solution was used for optical alignment. Analysis for each solution was replicated 3x times using an autosampler to obtain concentration with standard deviation. Sampling time and washing time (in between samples) were 1min and 0.75min respectively. For calibration for Pt concentration, three Pt calibration standards (100, 200 and 500ppm) were carefully prepared from standard solution (10,000ppm Pt ICP solution in 20% HCl, Ricca Chemical Co.). Calibration for Ru was performed similarly using 10,000ppm Ru plasma standard solution ($RuCl_3$ in 20% HCl, Alfa Aesar). Intensity at specific peak position (Pt = 265.896nm, Ru =240.272nm) for each metal were used to determine concentration using WinLab32 (version 2.2) software. Acceptable goodness of fit for calibration was set to be ≥0.999. For a lower goodness of fit, fresh standard solutions for calibration were prepared. Also, after each calibration a quality check (QC) was performed with a 200ppm standard solution. Acceptable limit of error in concentration for QC was set at ≤ ±10%. QC was performed

[1]Determination of Pt uptake using ICP-OES
Initial (pre-adsorption) and final (post-adsorption) Pt concentration C_i and C_f ppm (ICP)
Molecular weight Pt = MW_{Pt}
Pt uptake in μmoles/m^2 = $\frac{(C_i - C_f)[ppm] \times 1000}{MW_{Pt} \times SL\ [m^2/liter]}$

after sampling of 10 analytes for consistency. Concentrations up to 500ppm were measured using ICP. Higher concentration analytes were diluted within 500ppm concentration range before measurement.

1.4.2.3 X-Ray Diffraction (XRD)

High resolution Powder XRD apparatus using a Rigaku MiniFlexII bench-top system fitted with a Rigaku D/tex Ultra silicon strip detector was used to measure metal particle size of final catalyst. The radiation source was Cu Kα radiation (λ = 1.5406 Å) at operating condition of 30kV and 15mA. All spectra were taken at a scan rate of 1.0°/min and sampling width of 0.02°. Pt particle size was calculated using Scherrer formula with a shape factor of 0.94.

1.4.2.4 Pulse Chemisorption

Chemisorption was performed using hydrogen pulse titration of oxygen pre-covered metal (Micromeritics Autochem II 2920 automated analyzer). At first, approximately 0.05-0.1g of catalyst sample was reduced *in situ* by flowing 10% H_2/Ar (50ml/min) gas mixture at 250°C for 1h. This was followed by flow of pure Ar (50ml/min) at 250°C for 0.5h. Following cooling of the catalyst to 40°C in Ar flow, the catalyst was exposed to 10% O_2/He (50ml/min) for 0.5h to ensure saturation with adsorbed atomic oxygen and then purged with pure Ar for 0.5h to remove residual O_2. Pulses of H_2/Ar were initiated at this point to replace adsorbed oxygen with atomic hydrogen and form H_2O. Hydrogen consumption was quantified via a calibrated, high sensitivity thermal conductivity detector (TCD). H_2 Pulsing was continued until no further H_2 uptake. The overall stoichiometry of Pt to H_2 was assumed to be 0.667:1 [27]. Particle sizes were estimated assuming hemispherical geometry.

1.4.2.5 Scanning Tunneling Electron Microscopy (STEM)

STEM analysis was conducted using an aberration-corrected JEOL 2100F instrument. In this particular study, STEM images were used to measure metal particle size. ImageJ software was used to redraw and admeasure ~1000 Pt particles which yielded a representative statistical distribution of particle size. Both surface ($d_{s,EM} = \Sigma n_i d_i^3/\Sigma n_i d_i^2$) and volume ($d_{v,EM} = \Sigma n_i d_i^4/\Sigma n_i d_i^3$) average particle sizes were calculated from STEM images which were subsequently compared with chemisorption ($d_{s,chemi}$) and XRD ($d_{v,XRD}$) particle sizes respectively.

1.4.2.6 UV-Vis

UV-Vis analysis was performed using a Shimadzu UV spectrophotometer (Model: UV-1800) in absorbance mode. Light source change wavelength was 340.8nm and sampling interval 1. Approximately 4ml of the sample solution was placed in UV quartz cuvettes. DI water was used as reference standard. UV probe spectrum (version 2.31) software was used.

1.4.2.7 Temperature Programmed Reduction (TPR)

TPR analysis was performed using Micromeritics Autochem II 2920 automated analyzer equipped with a TCD. At first, At first, Pt adsorbed silica samples were dried *in situ* under He flow (50ml/min) for 2h at 120°C to remove moisture. After that, 10% H_2/Ar was flown through the sample (50ml/min) starting from room temperature up to 500°C at a ramp rate of 5°C/min.

1.4.2.8 Modeling software

Theoretical RPA model was coded using simulation packages of Matlab 7.0.

1.4.3 Methods

1.4.3.1 Pore volume and PZC determination

Pore volume of each support (no metal) was determined by adding water (De-ionized) drop wise (≤100µl) to a fixed mass (e.g., 1gm) of support placed in a 50ml polypropylene centrifuge tube. After addition of each drop, the centrifuge tube was vigorously tapped to ensure proper mixing. The volume of water that was required to barely wet the surface was recorded as the pore volume (ml/g) of that support. Using the surface area, SA (m^2/g) pore volume could be translated to incipient wetness surface loading, IWSL (m^2/liter), which is the maximum SL achievable for that particular support. Table 1.4 reports the IWSL value recorded for each support under consideration.

Table 1.4. Pore volume and incipient wetness surface loading (IWSL) of supports used.

Support	**Pore volume (ml/g)**	**IWSL (m^2/liter)**	**PZC (± 0.5)**
SBa 200 alumina	0.85	222,350	8.3
Aerosil®300 silica	2.8	117,900	4.1
Hombikat titania	0.82	420,700	6.3

Following determination of pore volume, PZC of each support was measured using Equilibrium pH at High Oxide Loading (EPHL) method [20]. For this, three pH solutions (pH_i = 3, 6, 9) were prepared. Each of these solutions was then added dropwise to known mass of support contained in 50ml polypropylene centrifuge tube up to the pore filling (pore volume) of the support. Final pH of the resulting three pore filled supports were then measured using spear tip pH probe electrode. Due to high slurry thickness, final pH for all three samples was at the PZC of the support (standard deviation ±0.5). This method is also known as 3-point pH shift method. Table 1.4 lists the determined PZC for support using this method.

1.4.3.2 SEA method

For each uptake survey at a specific surface loading, at first, a stock solution was prepared by mixing metal precursor complex in De-ionized water. Initial Pt concentration of this stock solution was selected so that there was more than enough metal in solution to achieve a theoretical maximum uptake of 1.6μmoles/m^2 for anionic $PtCl_6^{2-}$ and cationic $Ru(NH_3)_6^{3+}$ precursor and 0.84 μmoles/m^2 for cationic $Pt(NH_3)_4^{2+}$ precursor[2].

A series of 25ml solutions with different initial (pre-adsorption) pH (pH_i) was prepared from the stock solution by adding NaOH or HCl, as required and stored in 50ml centrifuge tubes. For $PtCl_6^{2-}$ solutions additional pre-adsorption aging for 48hrs was performed whereas for $Pt(NH_3)_4^{3+}$ and $Ru(NH_3)_6^{3+}$ freshly prepared solutions were used for adsorption.

Support was then added in powder form to each solution and the resulting slurry was thoroughly mixed for 1h in an orbital shaker. After 1h of mixing the final pH (adsorption pH) was recorded, followed by filtering the slurry in vacuum. The filtered sample remained under vacuum and was dried overnight at room temperature. After that, selected samples were reduced at 250°C for 1hr with 2.5°C/min ramp rate in a Lindberg furnace with a 10% in-house gas mixture (total flow rate = 200scc/min) of H_2 and He (Airgas). Prior to reduction a washing treatment was used as required. These reduced samples were characterized for metal dispersion and particle size.

[2] Example calculation for initial ppm for SL = 50,000m^2/liter
Maximum theoretical uptake with $Pt(NH_3)_4^{2+}$ on silica = 0.84μmoles/m^2
Initial Pt concentration used at this SL, $C_i \geq \frac{0.84\left[\frac{\mu mole}{m^2}\right]\times 50{,}000\left[\frac{m^2}{liter}\right]\times MW_{Pt}}{1000} \geq 8{,}200 ppm$

1.4.3.3 CEDI method

For CEDI method impregnating solution containing metal precursor complex with concentration that would yield the desired metal loading was prepared. pH of this impregnating solution was adjusted so that the final pH after adsorption is at the pH of maximum adsorption. This pH could be determined using RPA model [4]. Following pH adjustment, the impregnating solution was added dropwise to support placed in a 50ml centrifuge tube. After adding each drop of impregnating solution, the centrifuge tube was vigorously tapped for proper mixing and pH equilibration. Once the impregnating solution has been completely added the resulting sample was dried for 3h at 120°C in an oven and subsequently reduced at 250°C for 1h in flow of 10% H_2/He.

1.4.3.4 Washing treatment

A NaOH washing treatment was applied to remove residual ions remaining on metal adsorbed samples. For this a basic solution at the adsorption (final) pH was prepared with NaOH. In this solution, metal adsorbed support was added (1g/300ml) and left under mild stirring for 15min. After wards, the resulting thin slurry was filtered under vacuum. Recovered solid washed samples were dried and reduced for further characterization and filtrate was collected for ICP-OES analysis for possible Pt leaching.

1.5 Results

1.5.1 SEA adsorption survey versus pH

Different metal cationic and anionic precursors were used to study the effect of SL on SEA adsorption over a series of supports. High PZC (PZC 8.3) of alumina made it an ideal candidate for SEA adsorption study with anionic Pt precursor complex i.e., $PtCl_6^{2-}$. On the other hand, for the study of cationic $Pt(NH_3)_4^{2+}$ uptake, Aerosil®300 silica (PZC

4.1) and Hombikat titania (PZC 6.3) due to their low PZCs were the rational choices. Furthermore, cationic $Ru(NH_3)_6^{3+}$ complex adsorption study was performed over Aerosil®300 silica.

Adsorption survey plots using these precursor complexes over different supports at increasing SLs have been presented in Figure 1.3 (a-d). Theoretical RPA model predictions were also included in the same figures for comparison. Table 1.5 lists the parameters used for modeling/experimental purpose. Anionic $PtCl_6^{2-}$ adsorption over alumina (Figure 1.3a) showed decreasing trend with SL as predicted by the RPA model. On the contrary, cationic $Pt(NH_3)_4^{2+}$ adsorption onto both silica and titania (Figures 1.3 b and c) was unperturbed with SL. Finally for $Ru(NH_3)_6^{3+}$ adsorption onto silica the adsorption capacity decreased with SL initially (up to SL=5000m^2/liter), then remained unchanged at higher SLs. It should be noted that due to high pore volume of Aerosil®300 silica, as listed in Table 1.4, SL > 50,000m^2/liter was not possible in this case as the resulting slurry (after metal adsorption) became too thick to recover any filtrate (for final Pt concentration) via filtration or even centrifugation.

Table 1.5. Parameters used to study adsorption of SEA at increasing SLs.

Parameter	**CPA/A[2]**	**PTA/S[2]**	**PTA/T[2]**	**RuHA/S[2]**
PZC (support only)	8.3	4.1	6.3	4.1
Ionization constant (Δpk)[1]	5.0	7.25	5.0	7.25
Density of OH groups (Ns, sites/nm^2)[1]	8.0	5.0	8	5.0
Size of CPA ions (r_i,A^o)	2.95	2.41	2.41	3.0
No. of hydration sheaths	1	2	2	1
SL (m^2/l)	500-100,000	500-50,000	500-100,000	500-50,000
Initial Pt Conc. (C_i,ppm)	180-32,800	100-8,200	100-16,000	120-7,950

[1]Typical values obtained from literature [28]. [2]CPA=$PtCl_6^{2-}$, PTA=$Pt(NH_3)_4^{2+}$, RuHA=$Ru(NH_3)_6^{3+}$, A=alumina, S=silica and T=titania.

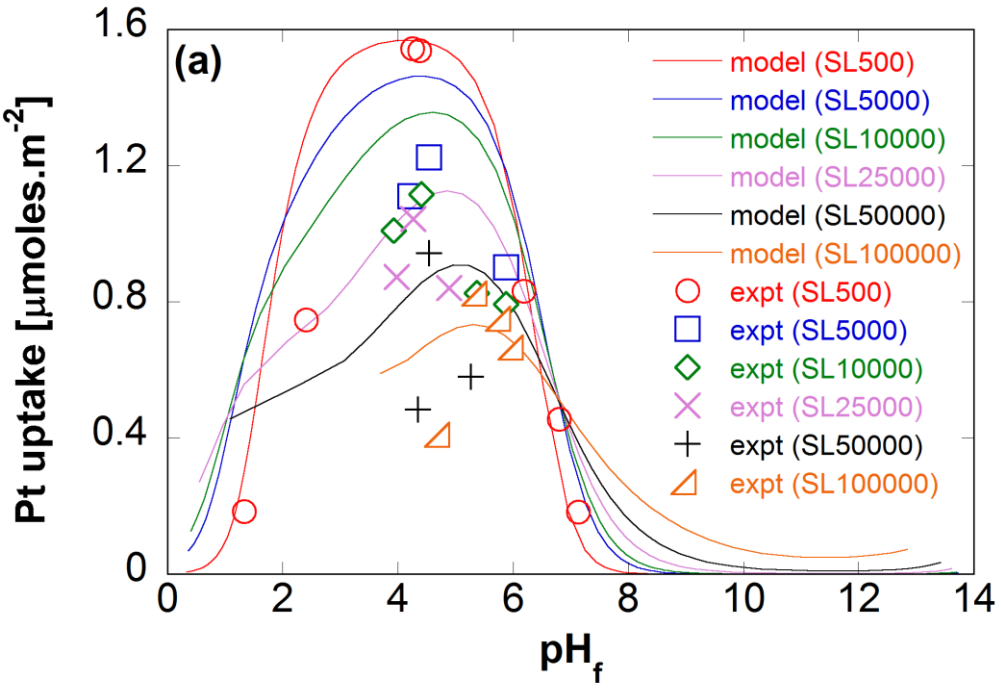
(a)
Pt uptake [μmoles.m-2]
pHf
model (SL500)
model (SL5000)
model (SL10000)
model (SL25000)
model (SL50000)
model (SL100000)
expt (SL500)
expt (SL5000)
expt (SL10000)
expt (SL25000)
expt (SL50000)
expt (SL100000)

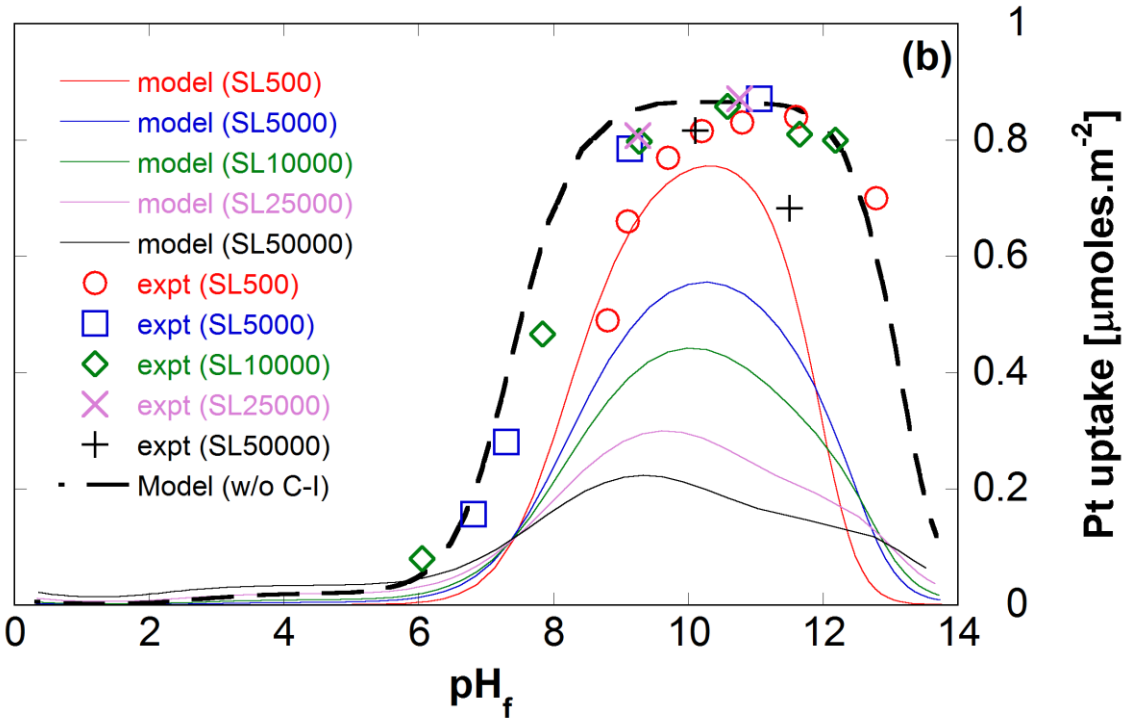
(b)
Pt uptake [μmoles.m-2]
pHf
model (SL500)
model (SL5000)
model (SL10000)
model (SL25000)
model (SL50000)
expt (SL500)
expt (SL5000)
expt (SL10000)
expt (SL25000)
expt (SL50000)
Model (w/o C-I)

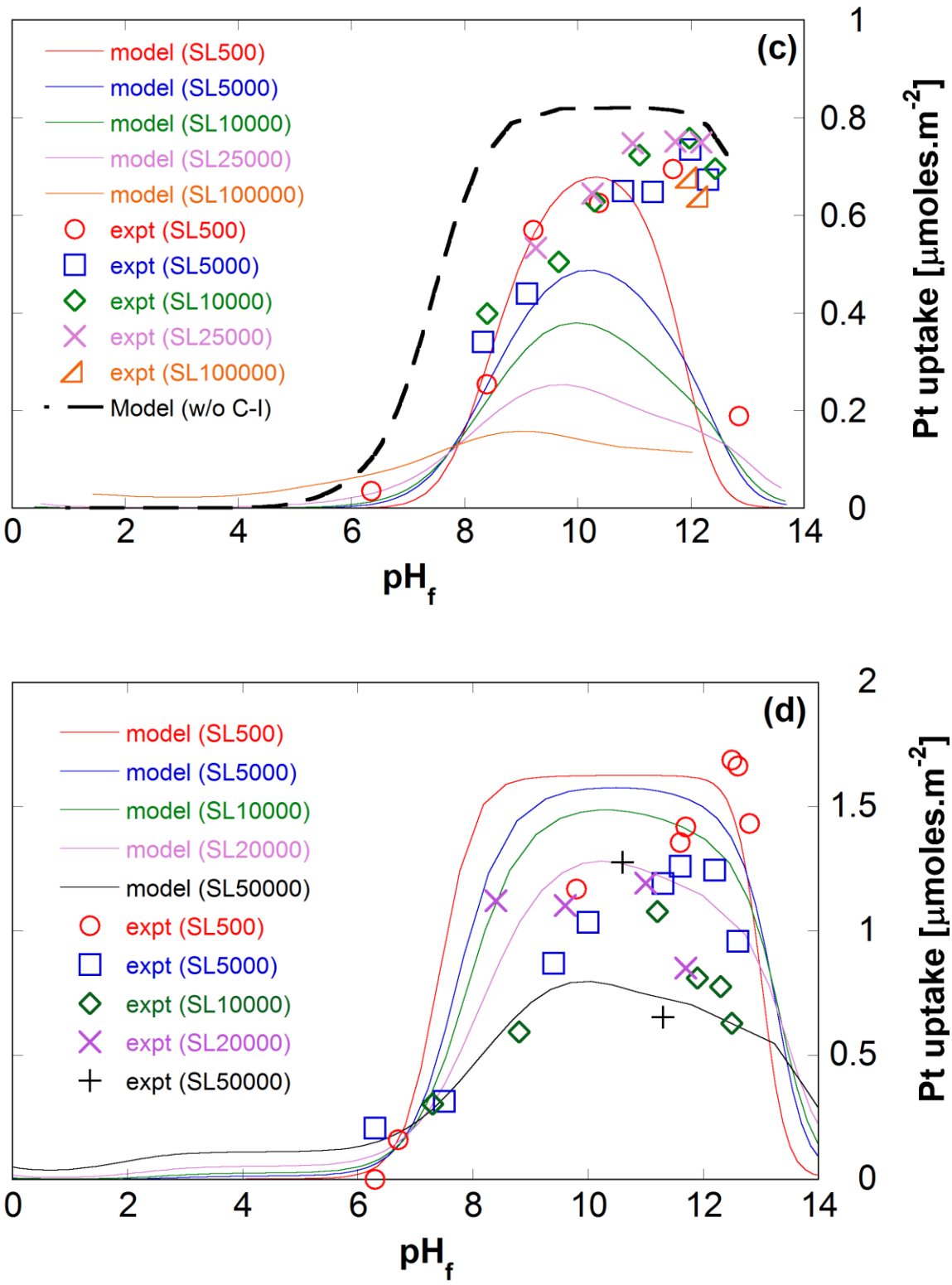

Figure 1.3. Metal precursor adsorption survey versus pH_f at increasing SLs. (a) $PtCl_6^{2-}$ over alumina, (b) $Pt(NH_3)_4^{2+}$ over silica, (c) $Pt(NH_3)_4^{2+}$ over titania and (d) $Ru(NH_3)_6^{3+}$ over silica. RPA model predictions are presented with solid lines. Error in uptake measurement via ICP $\leq \pm$ 10%

1.5.1.1 Effect of ionic strength on adsorption at low SL

In order to further elucidate the role of ionic strength on adsorption, an adsorption study was performed with $Pt(NH_3)_4^{2+}$ over Aerosil®300 silica at minimum slurry thickness (SL=500m^2/liter) and with ionic strength controlled by doping NaCl salt in the impregnating solution. Accordingly, a series of 100ppm $Pt(NH_3)_4^{2+}$ solution doped with various amounts of NaCl were adsorbed on to Aerosil®300 silica support at the same pH_i (12.0) and same low SL (500m^2/liter). With increasing NaCl concentration in solution the final pH (pH_f) was slightly changed from 11.6 (0N NaCl) to 10.9 (1N NaCl), which could also be predicted using the RPA model. The Pt adsorption uptake results are included in Figure 1.4 along with RPA model predictions in these conditions. As seen from the figure, a quite obvious discrepancy exists between experimental results and that predicted by RPA model.

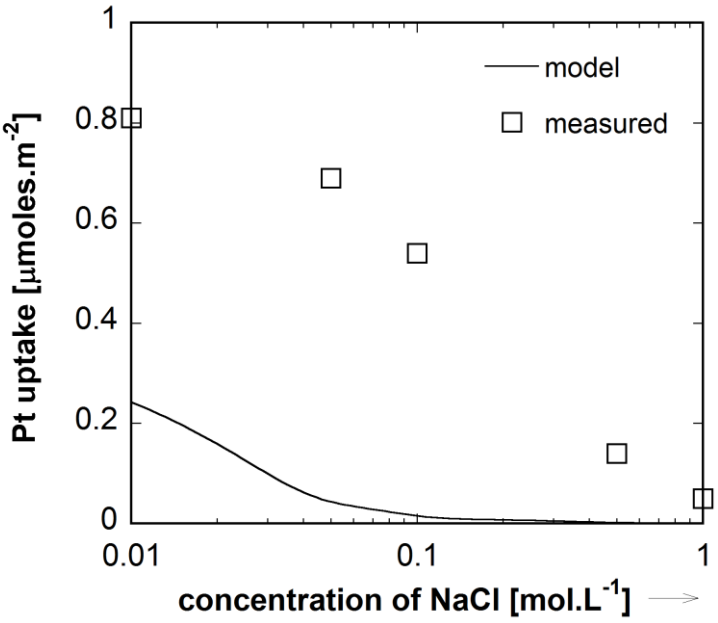

Figure 1.4. RPA model prediction versus measured metal uptake using $Pt(NH_3)_4^{2+}$ at different NaCl concentrations (SL=500m^2/liter, pH_i=12.0).

1.5.1.2 UV-Vis on $Ru(NH_3)_6^{3+}$ solution

UV-Vis spectra for four different $Ru(NH_3)_6^{3+}$ solution at different pH and concentration combinations have been presented in Figure 1.5. This experiment was performed to verify the stability of Ru(III) complexes in solution at different pH. Sample analysis was performed almost immediately after (within 10minutes) solution preparation and pH adjustment. High pH-high concentration solution had to be diluted 10x after preparation to obtain spectrum within the absorbance limit. From Figure 1.5, $Ru(NH_3)_6^{3+}$ at natural pH (pH=4.6) and low concentration (170ppm) showed two major peaks (~280nm and ~325nm). At higher pH and/or higher concentration the peak at 280nm shifts towards 300nm. Also at high pH, new peaks at 390nm and 550nm showed.

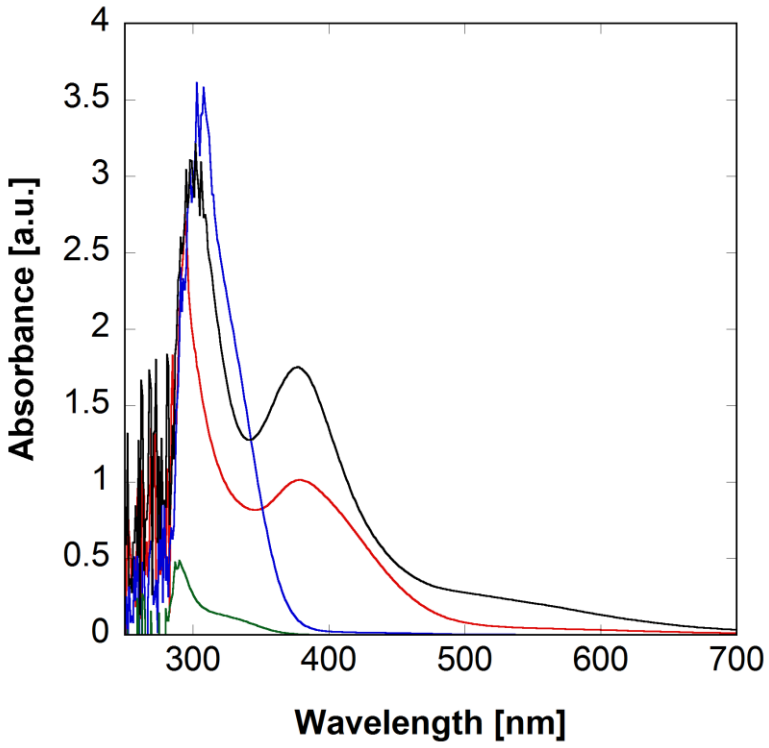

Figure 1.5. UV-Vis spectra of $Ru(NH_3)_6^{3+}$ solution. Different colored lines represent different pH and concentration combinations. pH4.6/170ppm (Green), pH 12/170ppm Ru (Red), pH4.6/1700ppm Ru (Blue), and pH12/1700ppm (Black). pH=4.6 is the natural pH for $Ru(NH_3)_6^{3+}$ precursor solution. pH=12 was adjusted using NaOH.

1.5.2 Metal loading and particle size of final catalyst

The reduced Pt-adsorbed silica and alumina samples with maximum metal uptake (for each SL) were characterized with XRD. Metal loading in each catalyst was calculated from the respective adsorption survey data and presented in Table 1.6.

Table 1.6. Summary of theoretical (RPA) and experimental (Exp.) maximum Pt uptake (μmoles/m^2) and corresponding Pt loading (wt%) at different SLs (m^2/liter).

SL	$PtCl_6^{2-}$/alumina		$Pt(NH_3)_4^{2+}$/silica		$Pt(NH_3)_4^{2+}$ /titania	$Ru(NH_3)_6^{3+}$ /silica
	RPA/Exp.	*Pt[1] wt%*	*RPA/Exp.*	*Pt[1] wt%*	*RPA/Exp.*	*RPA/Exp.*
500	1.57/1.55	5.4	0.77/0.84	5.1	0.68/0.7	1.63/1.70
5,000	1.46/1.22	4.3	0.63/0.87	5.3	0.49/0.74	1.58/1.26
10,000	1.36/1.10	3.9	0.54/0.86	5.3	0.38/0.76	1.49/1.08
25,000	1.13/1.04	3.7	0.4/0.87	5.3	0.25/0.75	1.28/1.23*
50,000	0.91/0.98	3.5	0.2/0.82	5.0	-	0.8/1.27
100,000	0.73/0.8	2.9	-	-	0.16/0.67	-

[1]Error in metal loading determination by ICP-OES ±10%

XRD patterns of reduced $PtCl_6^{2-}$over alumina samples revealed very small Pt particles (<1.5nm) with Pt peaks not distinguishable from the alumina peaks (Figure 1.6a). However, for reduced $Pt(NH_3)_4^{2+}$ over silica catalysts, strong influence of slurry thickness over final particle size could be observed as growth of Pt particle size increased with increasing SL (Figure 1.6b). In order to investigate the SL effect on particle size in silica supported catalysts two pretreatment procedures were applied in this case. These procedures were applied ahead of the reduction of $Pt(NH_3)_4^{2+}$ adsorbed silica samples, particularly those that were prepared using thicker (SL>10,000) slurries. These procedures were:

[1] Washing with a pH-controlled NaOH solution and

[2] Using a Cl^- free $Pt(NH_3)_4^{2+}$ precursor (e.g., $Pt(NH_3)_4(OH)_2$).

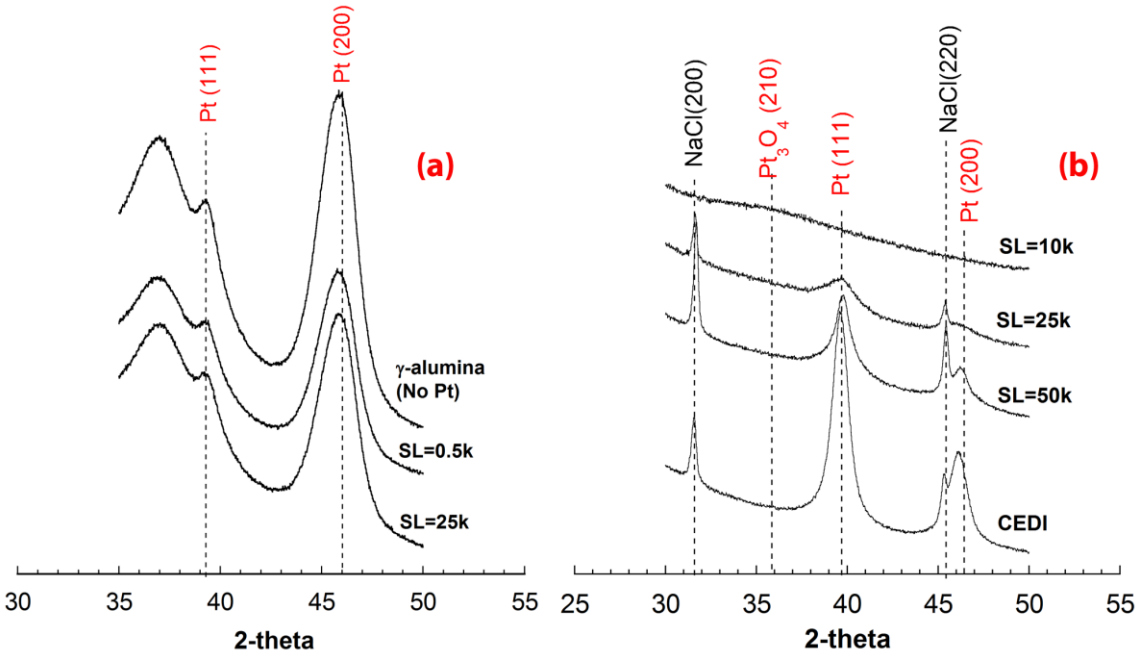

Figure 1.6. XRD patterns of (a) γ-alumina supported and (b) silica supported Pt catalysts synthesized at high SLs. Pt loadings from top to bottom in (a) are 0%, 5.4% and 3.7% whereas Pt loading on (b) is 5.0wt% (see Table 1.6). SL values in the labels are in m^2/liter.

Both these pretreatment procedures yielded very small particle size (<1.5nm) for Pt-adsorbed samples at thicker slurries after reduction as can be seen in Figure 1.7. ICP-OES analysis also revealed negligible Pt (<2%) loss after washing. Selected catalysts were characterized using STEM and chemisorption and the results showed excellent agreement with those measured using XRD. A representative STEM image has been included in Figure 1.8 along with average particle size and distribution. Pulse chemisorption was performed for the washed CEDI sample and Pt dispersion was found to be 75% (1.5nm active particle size).

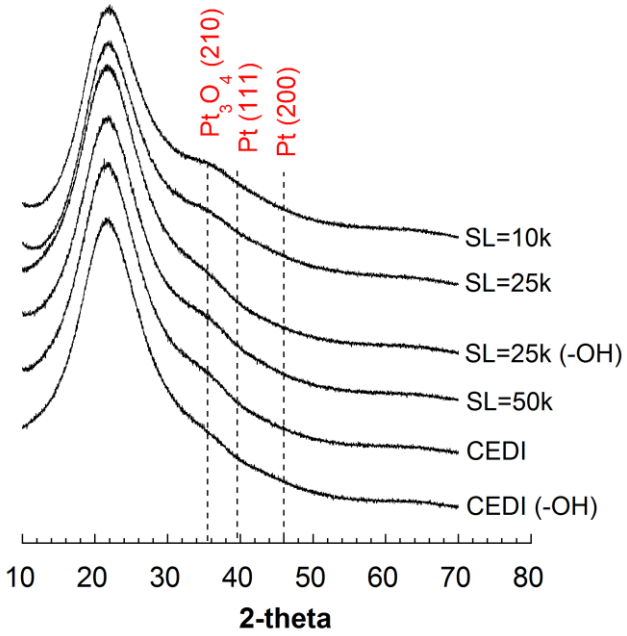

Figure 1.7. XRD patterns of reduced 5wt% Pt/silica catalysts prepared at various SL with either a washing step (labeled as "SL= #") or a Cl^- free precursor (labeled as "SL = # (-OH)"). SL values are in m^2/liter. k represents ×1000.

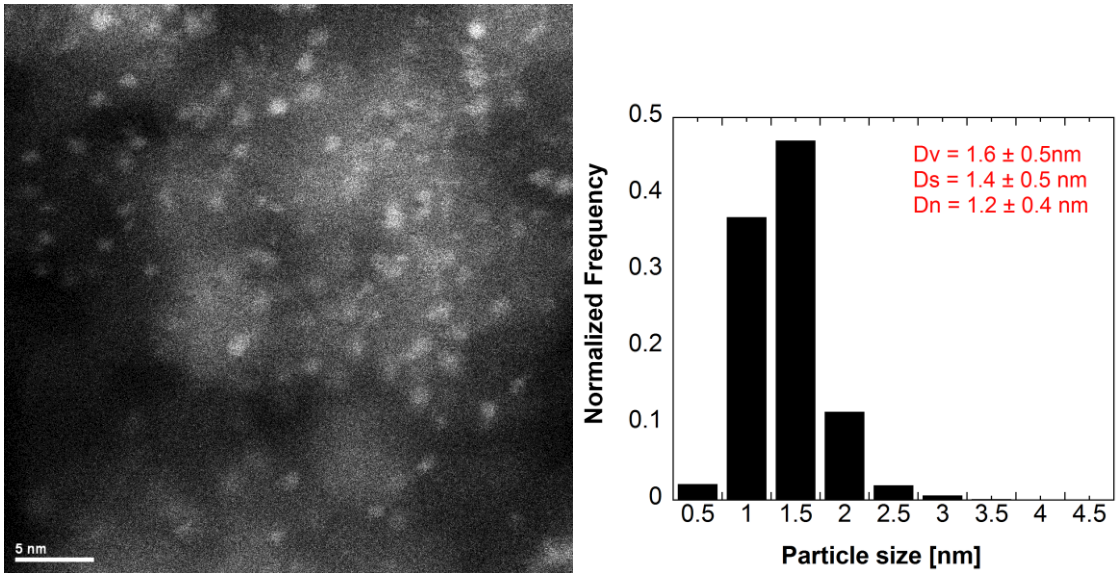

Figure 1.8. A representative STEM image of 5wt% Pt/silica catalyst using $Pt(NH_3)_4(OH)_2$ precursor at SL = 25,000m^2/liter along with histogram showing particle size distribution.

1.5.3 Metal particle size of ion doped catalysts

A series of ion doped CEDI catalysts was synthesized and characterized to elucidate the role of ions on the growth of supported metal nanoparticles. Due to very high slurry thicknesses in the CEDI setup, all the residual ions arriving from the acid/base or precursor ion remained on the support and were not removed prior to reduction. In the first set of experiments, three different combinations of cationic $Pt(NH_3)_4^{2+}$ and base (NaOH or NH_4OH) were used to isolate the contributions from each residual ion on final metal particle size. XRD patterns from the resulting catalysts are presented in Figure 1.9a. From this figure the presence of large Pt peaks is only apparent when residual Cl^- was present in the system. In the second set of experiments, different amounts of NaCl or $NaNO_3$ salt were dissolved in a series of impregnating solutions containing $Pt(NH_3)_4(OH)_2$ complex (concentration equivalent to 5wt% Pt loading). Then pH of the resulting solution was adjusted to 11.8 using NH_4OH and then added drop wise to a series of specific mass of Aerosil®300 silica support powder to complete the experiment. These CEDI-derived samples with different salt content were characterized after reduction using XRD for particle size (Figure 1.9b). In this figure, the gradual increase in Pt nanoparticle size (determined using Scherrer equation and included with each XRD pattern) with Cl loading is clearly apparent. However, such pronounced effect was not visible with NO_3^- as the size of Pt nanoparticles remained reasonably intact even with 0.8wt% NO_3^-.

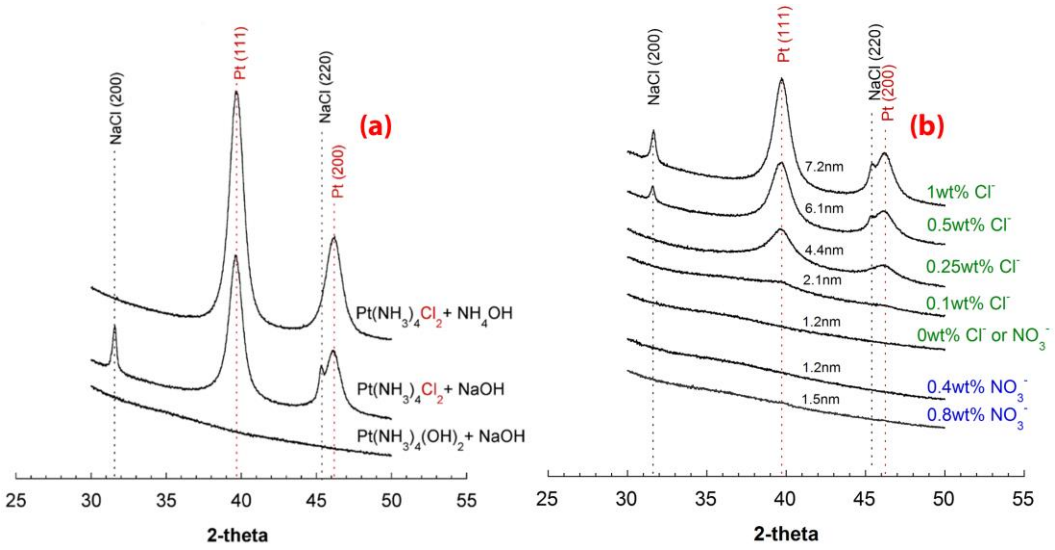

Figure 1.9. XRD patterns of 5wt% Pt/silica catalysts synthesized via CEDI using (a) different combinations of precursor complex and base as labeled and (b) $Pt(NH_3)_4(OH)_2$ precursor, NH_4OH base and different concentrations of anions (Cl^-, NO_3^-) as labeled.

Pulse chemisorption and STEM was performed on selected Cl^- doped size controlled Pt/silica catalysts showed in Figure 1.9b. The resulting particle sizes are compiled in Table 1.7. Two representative STEM images are presented in Figure 1.10 to visualize the effect Cl^- on particle size. Although average particle size in the Cl^- loaded Pt catalysts (Figure 1.10b) was larger than Cl^- free catalysts (Figure 1.10a), much wider distribution of particle size was observed in the Cl^- loaded catalyst.

Table 1.7. Pt nanoparticle sizes of Cl^- doped Pt/silica catalysts.

Pt wt%	**Cl wt%**	**Particle size (nm)**			
		D_{XRD}	$D_{V,STEM}$	$D_{chemisorption}$	$D_{S,STEM}$
5	0	1.2	1.9	1.5	1.8
5	0.1	2.1	-	2.0	-
5	0.25	4.4	4.3	3.6	3.5
5	0.5	6.1	-	4.6	-
5	1	7.2	-	6.6	-
2	0.25	6.4	-	4.0	-
3.5	0.1	2.8	-	2.1	-

$D_{V,STEM}$, $D_{S,STEM}$ are volume and surface averaged particle sizes respectively

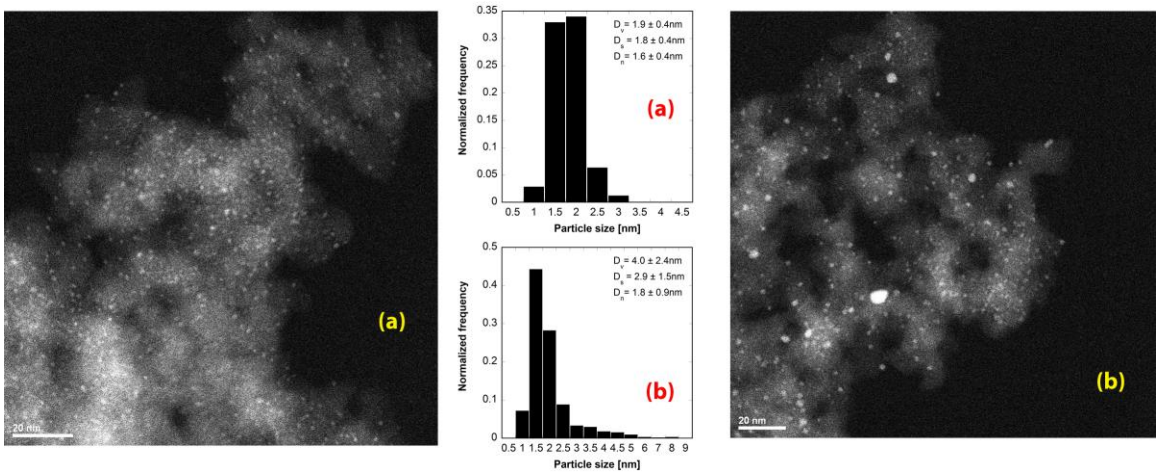

Figure 1.10. Representative STEM images with particle size and distributions of 5wt% Pt/silica catalysts synthesized via CEDI using $Pt(NH_3)_4(OH)_2$ precursor, NH_4OH base and with (a) 0wt% and (b) 0.25wt% Cl^-.

1.5.4 TPR of ion doped Pt adsorbed samples

TPR of the ion (Cl^- or NO_3^-) doped metal adsorbed samples were conducted to identify the characteristic reduction peaks of these samples. The resulting TPR profiles have been included in Figure 1.11. At first, the Cl^- or NO_3^- free samples showed two reduction peaks (220°C and 350°C). With addition of Cl^- low temperature reduction peaks (100-150°C) appeared with the disappearance of the peak at 350°C. These low temperature reduction peaks became more prominent with Cl^- content. The low temperature reduction peaks might be an indication of the formation of large Pt particles in Cl^- doped samples. The absence of such low temperature peaks for the NO_3^- (0.8% NO_3^-) doped sample for which the resulting Pt particle size was fairly small (Figure 1.10b) corroborates such possibility.

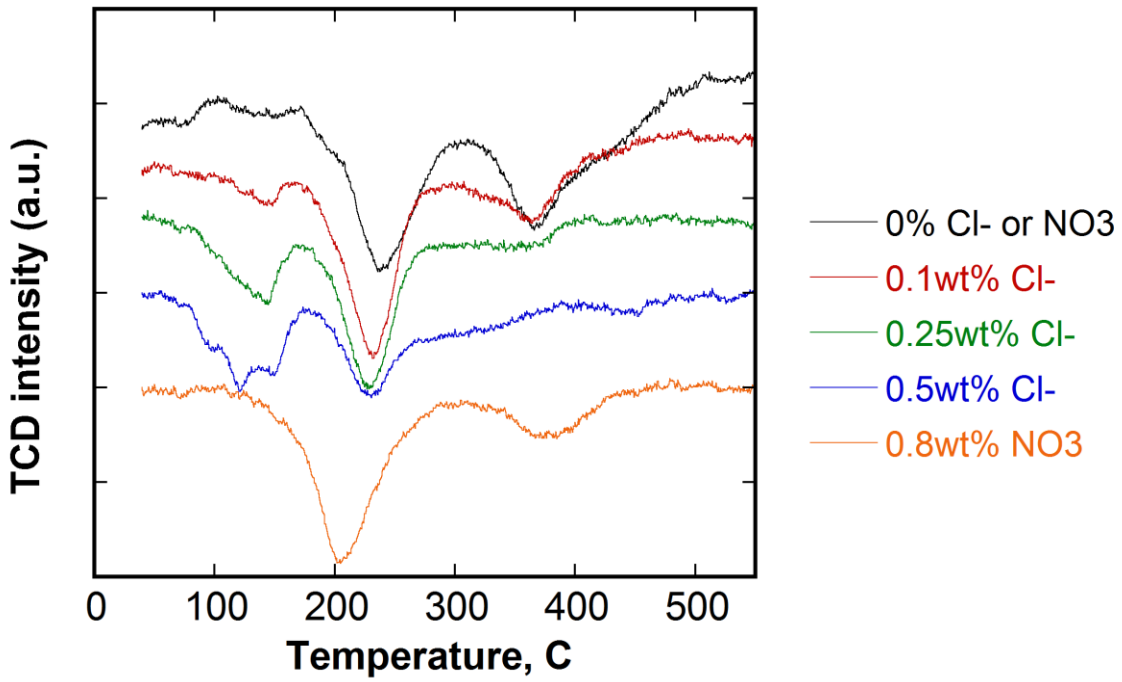

Figure 1.11. TPR profiles of different ion doped (Cl^- or NO_3^-) and $Pt(NH_3)_4(OH)_2$ adsorbed samples (5wt% Pt).

1.6 Discussion

Since RPA model primarily considers coulombic interaction between metal ions and support, it predicts retardation in adsorption with increasing slurry thicknesses caused by higher concentration of residual ions. This effect, often referred to as "electric screening", was experimentally verified using anionic $PtCl_6^{2-}$ adsorption over alumina (Figure 1.3a). Trend of adsorption uptake of $PtCl_6^{2-}$ indeed showed drop-off as predicted by the RPA model in the same Figure. From Figure 1.3 the maximum adsorption for each SL was translated to metal loading and the resulting values were listed in Table 1.6. From catalyst synthesis standpoint, due to the retardation effect of SL on SEA uptake, significant loss of metal adsorption capacity and metal loading would occur if a $PtCl_6^{2-}/Al_2O_3$ catalyst is synthesized via SEA using thick slurries. Despite loss of metal loading, metal particle

size of the final catalyst seemed to be unaffected by slurry thickness as particle size remained small and undistinguishable via XRD (Figure 1.6a).

On the contrary, similar agreement between RPA model and experimental measurements was not observed with $Pt(NH_3)_4^{2+}$adsorption over silica or titania. On both these supports, SEA adsorption capacity was seemingly unperturbed by slurry thickness although RPA model predicted, in both instances, a significant drop-off (Figure 1.3b,c). An additional dashed line, labelled as "model (w/o C-I)" has been added in Figure 1.3b and c, showing RPA model prediction when no influence of counter-ion concentration on Pt uptake is assumed. The observation that measured Pt uptake data points in Figure 1.3b,c at all SLs clustered at/near this zero influence line hints towards significantly reduced influence of ionic strength on cationic Pt uptake over these supports. As a result, a Pt/silica catalyst could be prepared at maximum SL (CEDI) setup without having to compromise metal loading.

From the study presented in Figure 1.4, the effect of ionic strength could be isolated from the effect of slurry thickness. All experiments, shown in this figure, were performed at constant low SL. However, ionic strength was varied using different salt concentrations. The results were consistent with the observations in Figure 1.3b,c. Ionic strength did not affect adsorption capacity until after a significant concentration (>0.025N NaCl). Up to this concentration (0-0.025N NaCl), the measured uptake remained unchanged although theoretically a drastic reduction in uptake was anticipated.

The discrepancy between the RPA model and experiment for cationic adsorption at high SLs is yet unresolved. One possibility stems from the degree of hydration of $Pt(NH_3)_4^{2+}$ and $PtCl_6^{2-}$ precursor. The latter retains one hydration sheath, whereas

$Pt(NH_3)_4^{2+}$ retains two [6, 29]. It is hypothesized that the two hydration sheaths brought to the adsorption plane by the metal precursor act to dilute the counter-ion concentration at the adsorption plane, thereby lowering the local ionic strength and eliminating the retardation of adsorption.

In order to verify this hypothesis, similar adsorption study over silica was performed using $Ru(NH_3)_6^{3+}$ which, unlike $Pt(NH_3)_4^{2+}$, retains a single hydration sheath [22]. As a result, maximum adsorption capacity of $Ru(NH_3)_6^{3+}$ precursor over Aerosil®300 silica was measured to be 1.6μmoles/m^2 at low SL. Also if the hypothesis were to be correct, the effect of ionic strength on adsorption would be more pronounced than that observed with $Pt(NH_3)_4^{2+}$. Indeed, at higher SLs, $Ru(NH_3)_6^{3+}$ adsorption capacity was lowered until SL=20,000m^2/l. However, at SL>20,000m^2/l adsorption capacity surprisingly did not follow any particular trend as seen in Figure 1.3d. Similar trend was observed with a different silica (Aerosil®380). For comparison, adsorption capacity of $Ru(NH_3)_6^{3+}$ and corresponding RPA model predictions are listed in Table 1.6.

This unusual behavior could be attributed to the speciation of $Ru(NH_3)_6^{2+}$ complex at high pH and high concentrations as confirmed from the UV-Vis study (Figure 1.5). At natural pH and low concentration, two peaks corresponding to $Ru(NH_3)_6^{3+}$ complex can be observed at 275 and 325nm [30]. At high pH (pH typically used for SEA adsorption of cationic precursor complex over low PZC support) the peak at 265nm shifts to 300nm which is most likely due to the formation of $Ru(NH_3)_5(OH)^{2+}$[31]. As can be seen from Figure 1.5 that at high concentration and/or high pH, two peaks at 390 and 550nm start to appear. These peaks are generally associated with Ru red i.e., $[(NH_3)_5Ru^{III}O–Ru^{IV}(NH_3)_4–O–Ru^{III}(NH_3)_5]^{6+}$ [31]. This speciation and evolution of different Ru complexes at high

SL/pH might have caused rapid change in precursor color as well as lowered the pH. Hence, particularly for high pH and high SL, care should be taken to make sure adsorption is performed right after preparing the pH adjusted impregnating solution. Nevertheless, it can be summarized that the presence of different Ru complexes can add to the complexity of the quantification of ionic strength and its ultimate effect on the adsorption capacity. However, initial drop in adsorption capacity with SL does indicate more pronounced role (than $Pt(NH_3)_4^{2+}$) of ionic strength on adsorption which hints towards an agreement to our hypothesis.

Effect of slurry thickness on metal dispersion/particle size of final catalyst has been performed primarily with $Pt(NH_3)_4^{2+}$adsorbed silica samples primarily due to their unusual nature of SEA uptake. A standard SEA protocol where metal adsorbed samples were dried and directly reduced was applied at first. With increasing SL, this procedure resulted in larger average size of Pt on the final catalysts. In a typical SEA setup with enough excess of the impregnating solution, post-adsorption filtration allows removal of significant portion of the residual ions. This becomes increasingly more difficult as thickness of the slurry (also, SL) increases. Particularly, since Aerosil®300 silica had almost 3x the pore volume of other supports this silica appeared to be thicker than rest of the supports at similar SLs. As a result, despite filtration or even centrifugation, a significant portion of the residual ions remained with the Pt adsorbed support. It was initially hypothesized that the leftover residual ions facilitated the growth of Pt nanoparticles during the reduction process.

Further study confirmed the role of these ions on the final metal particle size. It was also understood that Cl^- has the maximum influence on the growth of supported Pt

nanoparticles. A series of experiments were performed in order to arrive at this conclusion. Firstly, $Pt(NH_3)_4^{2+}$ that was used for the study in Figure 1.6b, came with Cl^- counter-ions. These counter-ions when washed off with a basic solution prior to reduction drastically lowered Pt particle size of the final catalyst compared to the unwashed samples (Figure 1.7). Secondly, when $Pt(NH_3)_4^{2+}$ with Cl- free counter-ion e.g., $Pt(NH_3)_4(OH)_2$ was used, small Pt particles resulted even without washing which further hints towards the influence of Cl^- (Figure 1.7). Finally, three CEDI experiments (no filtration) were performed with different combinations of $Pt(NH_3)_4^{2+}$ precursor and base. From the XRD patterns it is obvious that only when Cl^- was present in the setup, growth of Pt nanoparticles was facilitated (Figure 1.9a).

Growth of metal nanoparticles influenced by the presence of ions will be addressed in further detail in future. Nevertheless, preliminary results, as discussed here, offer interesting possibilities with regards to controlling metal particle size on supported catalysts. This was demonstrated via controlled doping of Cl^- ions in a CEDI setup (Figure 1.9b). From XRD patterns, of these Cl^- doped catalysts, it was shown that such control over metal particle size is possible. With simple Cl^- doping and at moderate reduction temperatures a particle size between 1.2 to 7nm could be achieved. Similar influence on particle size was not noticed with other anions e.g., NO_3^- although its influence at a much higher concentration cannot be discarded. STEM images in Figure 1.10 revealed, however, that the growth of Pt nanoparticles did not occur uniformly in presence of Cl^- (high standard deviation). Average particle sizes measured from the STEM images along with the XRD and chemisorption sizes (Table 1.7) were plotted against the atomic ratio of Cl and Pt in Figure 1.12. STEM particle sizes were represented in terms of surface averaged, D_s

(comparable to chemisorption size) and volume averaged, D_v (comparable to XRDs size) size. From this figure Pt particle size also demonstrated good correlation with respect to ratio of [Cl] to [Pt] rather than [Cl] itself. This was further verified using different Pt wt% (other than 5wt%) catalysts with results also included and labeled in Figure 1.12. Nevertheless, currently available method of controlling metal particle size involves calcination at high temperatures. Many oxide supports are not amenable to calcination treatments (e.g., SBA-15 silica) [22]. Particularly, for those system of catalysts, a softer approach like doping Cl^- , with some improvements, could become a useful technique.

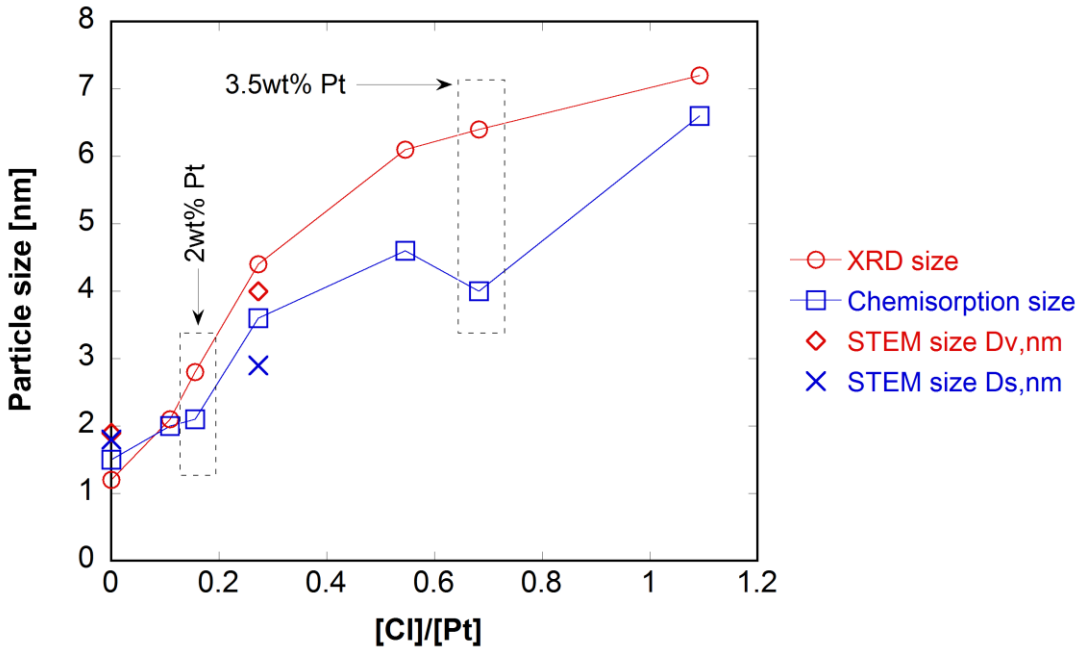

Figure 1.12. Particle size of silica support Pt nanoparticles with respect to the atomic ratio of Cl and Pt. Except those marked otherwise, Pt loading on all samples is 5wt%.

1.7 Conclusions

In summary, we have carried out a systematic study to understand the effect of slurry thickness on the metal adsorption capacity of different PZC supports. Resulting

synthesized catalysts have been characterized and studied for final metal particle size. The results can be summarized as follows:

[1] The uptake of $PtCl_6^{2-}$ on alumina at low pH was affected at high surface loading similarly as predicted by the RPA model. As a result, well-dispersed Pt catalysts yet with lower Pt loading could be prepared via SEA at high SL.

[2] Same was not mirrored at the basic pH range for $Pt(NH_3)_4^{2+}$ adsorption over silica and titania. In these cases, the decrease in maximum adsorption capacity was much lower than that predicted by RPA model at high surface loadings or in presence of high concentrations of counter-ions at low surface loadings.

[3] Complexation of $Ru(NH_3)_6^{3+}$ precursors at high pH and/or high concentrations complicated the study of the effect of ionic strength on adsorption. However, initial drop-off in adsorption with SL suggests more pronounced role of ionic strength on adsorption capacity compared to $Pt(NH_3)_4^{2+}$. This was in line with the proposed hypothesis that retention of more than one layer of hydration by metal complexes can dilute the concentration of ions and their possible influence on adsorption.

[4] Although the adsorption capacity of $Pt(NH_3)_4^{2}$ over silica and titania was largely unaffected by the presence of ions, final particle size of the resulting catalysts was not. By using a pre-reduction washing step or a Cl^- free $Pt(NH_3)_4^{2}$ precursor, such influence on particle size was effectively eliminated.

[5] Role of Cl^- on the growth of metal nanoparticles offered interesting avenues to synthesize supported catalysts with controlled particle sizes. This has been demonstrated via simple salt impregnation during $Pt(NH_3)_4^{2}$/silica catalyst synthesis and could potentially be expanded to many different metals.

1.8 Future work

This project addressed a very interesting topic and the initial outcomes of it offered some very exciting opportunities with plenty of scopes of improvement. For example, genesis of the role of ions on the growth of nanoparticles could be investigated further and applied to other metals (e.g., Au, Ag, Pd). Influence of other ions, in the halogen series, can also be studied. On the other hand, $PtCl_4^{2-}$ and $PdCl_4^{2-}$ are two anionic metal precursors that adsorb with two hydration sheaths. Effect of SL on the SEA adsorption with these precursors can further elucidate if number of hydration sheaths does indeed play a significant role on nullifying the effect ionic strength as has been hypothesized in this study. Finally, some modifications of CEDI approach will be tested in order to ensure uniform size of supported metal nanoparticles by ion doping.

Chapter 2

Determining surface composition of mixed oxides with pH

2.1 Introduction

Composite metal oxides are extensively used in industrially significant catalytic and electrocatalytic processes [32-35] and have demonstrated tremendous potential to replace single metal oxides in metal ion adsorption, separation and photosensitive operations [36-41]. Many of these processes benefit from the unique properties that mixtures of two or more oxide components can develop [36-41].

For a mixed oxide system it is often important to study the electro- and physico-chemical properties based on the fractional surface coverage of each of the oxide components [37, 41-46]. Common surface analysis techniques are often expensive and necessitate considerable expertise and maintenance [34]. Moreover, if one or both of the oxides is porous, as in industrial catalysts, the quantification of composition can be problematic [47].

PZC of a metal oxide is a surface sensitive property that accounts for the proton transfer to and from the surface hydroxyl groups which causes dramatic pH shifts in an aqueous solution [20]. Park and Regalbuto used a technique that they referred to as Equilibrium pH at high oxide loading (EPHL), to determine PZC of single oxides via

simple pH measurements [20]. They also used a single site model to predict the dramatic pH shift. However, for mixed oxides, PZC could be considered to reflect the cumulative charge contribution from each component, which would be a function of the surface composition. While EPHL and the associated single site model was originally developed for single oxides [20], the current study demonstrates how it can be extended into a "2-surface model" to provide estimates of surface composition for mixed oxides. Following objectives were set for this study:

1. Development of a 2-surface model by extending the single site-single surface pH shift model that would be a non-Nernstian description of mixed oxide surface.
2. Determination of oxide charging parameters, namely the protonation and deprotonation constants and the hydroxyl surface densities, from measurements of the pure oxides. These parameters will be used in the 2-surface model, to predict the PZC of mixed oxides.
3. Determination of the "apparent surface coverage" (ASC) of mixed oxides by comparing the PZC of the material to the 2-surface model results, using parameters of the individual oxides.
4. Test accuracy of 2-surface model using various characterization tools. Application of this model on data extracted various literature.

Overall scheme of 2-surface model has been illustrated in Figure 2.1. Nevertheless, for objective 1, extension of the single site EPHL model to "2-surface model" was coded using Matlab. A simple and non-interacting mixture of two components was assumed. For objective 2, oxide charging parameters for various silica and alumina powders were estimated from independent pH shift measurements [28]. These parameters were used in

the 2-surface model to predict the PZC of physical mixtures where these silica and alumina powders were used as components. For objective 3, another utility of the 2-surface model was tested as PZCs of mixed oxides were used to estimate surface composition, in the form of, "apparent surface coverage" (ASC). For objective 4, XPS and BET were used to verify 2-surface model predictions. This model was also subsequently used to predict some prior works in literature [48, 49].

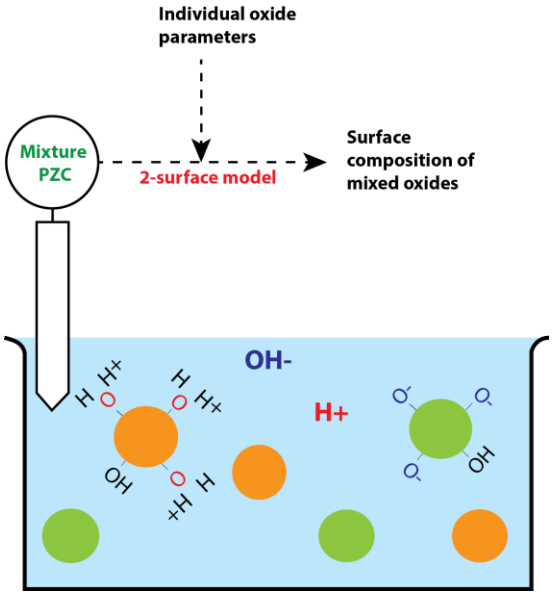

Figure 2.1. Determination of surface composition of mixed oxide using 2-surface model.

The main contributions of this research are:

(1) Development of 2-surface model that can be used to predict surface composition of mixed and composite metal oxides with simple and inexpensive pH measurements.

   a. Journal publication:
   Samad, J. E., Hashim, S., Ma, S., & Regalbuto, J. R. (2014). Determining surface composition of mixed oxides with pH. *Journal of colloid and interface science*, *436*, 204-210.

2.2 Characterization of mixed oxide surfaces

Various sophisticated characterization tools are often consulted to evaluate surface properties of mixed oxides. Common surface analysis techniques such as x-ray photoelectron spectroscopy (XPS) and auger electron spectroscopy (AES) may not be adequately surface sensitive as both detect the top ten layers of the surface of light elements. In secondary-ion mass spectroscopy (SIMS), 95% of the detected emitted radiation is from the top 2 layers [44]. Ion scattering spectrometry (ISS) is the most surface sensitive technique available, and derives information almost exclusively from the top monolayer [44].

Studies conducted over the last few years underscore the importance of developing a simpler technique that can be applied to predict surface properties of mixed oxides easily and accurately [32, 37, 41, 43, 45, 46, 50]. In many of these studies the surface under investigation can be characterized in terms of its point of zero charge (PZC). Parks utilized the Gouy-Chapman version of electrical double layer theory to show that PZCs of mixed oxides change linearly with the weight fraction of individual components assuming that the components do not interact with one another [51]. Schwarz et al. used mixtures of silica and alumina and claimed to have found direct agreement with the results obtained by Parks [50]. Some observed non-linear dependence of PZC of a SiO_2 and Al_2O_3 physical mixture on surface composition which they attributed to the higher sensitivity of alumina to the change of pH [52, 53]. Elsewhere, one of the composite oxide models proposed by Schwarz group was based on the premise that PZC of a mixed oxide is the sum of its pure component PZC weighted by surface area [54]. In cases where 2^{nd} oxide is present at a reasonably high concentration they proposed another model where they utilized (1) mixed oxide PZC

values measured by “mass titration” method and (2) physical mixture calibration curve [48]. Zhang et al (2008) used proton equilibrium relations to introduce non-linearity in Parks’ model which he showed to fit the experimental values of TiO_2 and Al_2O_3 mixtures reasonably better [41]. Some have implicated that the surface area effect is the cause of non-linearity, which means Parks’ linear model is only valid when components of a mixture share the same surface area [32, 55]. Others tried to relate mixture PZC to the surface coverage through a number of equations that are mostly empirical and component specific [48].

2.3 EPHL method and oxide charging parameters

EPHL method and its associated equations have been included in section 1.3.1. From these equations, three material specific oxide surface parameters could be identified that need to be determined independently to predict pH shifts in presence of metal oxides in solution. These are: (a) ionization constant (ΔpK), (b) Density of hydroxyl groups (N_s) and (c) PZC.

Determination of these charging parameters has been studied extensively in literature [28, 56-59]. Firstly, ΔpK stems from protonation and deprotonation constants, K_1 and K_2 which quantify the propensity of terminal hydroxyl groups to undergo protonation and deprotonation at pH other than the PZC. In a typical double layer system, K_1 and K_2 would be on the opposite sides of and equidistant from the PZC [20, 28, 60]. Now, PZC carries great physical significance and can be measured rather easily. As a result, it is often convenient to use the terms ΔpK (pK_1-pK_2) and PZC as a pair rather than using K_1, K_2 separately. Secondly, various experimental techniques exist to determine density of hydroxyl groups, N_s (OH groups/nm^2). These include potentiometric titration, infrared and

deuterium exchange [56, 60, 61]. As oxide surface becomes fully protonated or deprotonated, this N_s value determines the extent of charge on the surface. Finally, a wide array of methods is in place to determine PZC of oxides. As for example, it can be determined by potentiometric titration, zeta potentiometry, mass titration and EPHL method [20, 60, 62]. All these methods have their advantages and limitations [20]. Nevertheless, in this study, EPHL method will be used exclusively for PZC determination.

Schreier et al introduced a rather simple way to determine these charging parameters [28]. Their method involved optimizing these critical parameters using Equation 1.1-1.4 to fit the pH shift data obtained experimentally for each metal oxide in solution. This can be conducted in two ways: (a) single parameter fitting and (b) three parameter fitting. For (a), PZC, obtained experimentally via EPHL and N_s from literature, are used to fit pH shift data by optimizing ΔpK in the model equations (Equation 1.1-1.4). On the other hand, for (b), all three parameters are optimized simultaneously to fit the pH shift data. pH shift experiments should be conducted at several SLs for better fitting of parameters. Thus with the help of simple pH shift experiments, acceptable set of values for these parameters could be determined that can be subsequently used to model metal adsorption uptake over oxides with higher degree of predictability. Matlab codes associated with this parameter fitting have been presented in Appendix A.2.

2.4 Theory behind 2-surface model

For 2-component mixed oxides, two different OH groups will populate the surface and thereby create 2 different surfaces for aqueous medium to interact (Figure 2.2). Furthermore if it is a physical mixture it can safely be assumed that one type of hydroxyl group will not affect the functionality of the other and vice versa. For such a system the

net charge at a given pH can be predicted as the sum of negatively charged (more acidic) and positively charged (more basic) sites weighted by mole fraction (Equation 2.1).

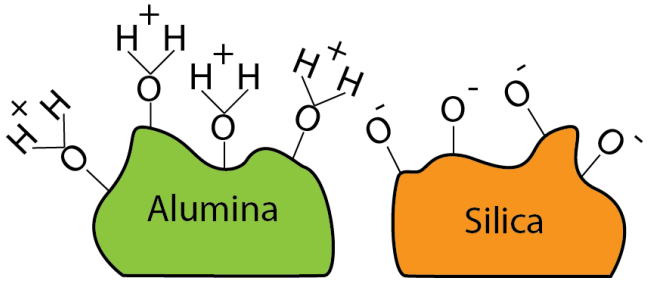

Figure 2.2. Simplistic depiction of a physical mixture of alumina and silica immersed in an aqueous solution where $PZC_{silica}<pH<PZC_{alumina}$

$\sigma_{net}=f_1\sigma_1+f_2\sigma_2$ **Equation 2.1**

Where, $f_k=\frac{\text{moles of OH groups on k surface}}{\text{total moles of OH groups}}$

When pH is near the PZC of the oxide surface the Nernstian approximation accurately estimates surface charge in terms of pH of solution and PZC of individual oxides (Equation 2.2). However, this approximation is no longer valid when pH values are considerably different from the PZC of individual component. Hence a new term (y_k) has to be introduced to the equation to account for the deviation (Equation 2.3).

$\sigma_k=K(pH - PZC_k)$ **Equation 2.2**

Where, $K=\frac{\varepsilon k}{4\pi}$

$\sigma_k=y_k K(pH - PZC_k)$ **Equation 2.3**

At the PZC the net charge of a mixed oxide will be zero i.e., negatively charged sites will effectively cancel out positively charged sites. Thus Equation 2.1 transforms to:

$0 = K[y_1 f_1(PZC_{mix} - PZC_1) + y_2 f_2(PZC_{mix} - PZC_2)]$ **Equation 2.4**

Mole fractions of oxide can be represented in terms of terminal hydroxyl groups (Equation 2.5), whereas ASC can be defined as the fraction of surface area occupied by one component (Equation 2.6).

$$f_k = \frac{A_k N_k}{\sum A_k N_k} \qquad \textbf{Equation 2.5}$$

$$ASC_k = \frac{A_k}{\sum A_k} \qquad \textbf{Equation 2.6}$$

A_k is the area contributed by component k and N_k is the density of hydroxyl (OH) groups on the surface of component k.

Combination of Equation 2.4 to 2.6 yields the final equation for 2-surface model,

$$ASC = \left[Z\left(\frac{PZC_{mix} - PZC_2}{PZC_1 - PZC_{mix}}\right) + 1\right]^{-1} \qquad \textbf{Equation 2.7}$$

Where $Z = \left(\frac{y_2}{y_1}\right)\left(\frac{N_2}{N_1}\right)$ **Equation 2.8**

Z values can be obtained by solving, for each component, the oxide charging equation (Equation 1.2) and Gouy-Chapman model equation (Equation 1.3) at the pH of the mixed or composite oxide.

This yields the value for y_1 and y_2 from Equation 2.3. Z is then calculated from Equation 8 using known N_1 and N_2 values. ASC values for each set of physical mixtures are then calculated using Equation 2.7. Matlab codes used for 2-surface model have been included in Appendix A.3.

2.5 Materials and methods

2.5.1 Sample preparation

All the oxides were used as received in this study and have been listed in Table 2.1. Surface area (SA) values included in the table were obtained from BET analysis.

Table 2.1. Properties of oxide materials used in this study.

Material	**BET SA (m^2g^{-1})**	**Product name & manufacturer**
γ-alumina (HA)	157	Catalox SBa-200, Sasol
Silica (HS)	182	Aerosil® TT600, Evonik
α-alumina (LA)	33	Ceralox APA 0.2, Sasol
Silica (LS)	54	Aerosil® OX50, Evonik

Two silica samples (HS & LS) were physically mixed with two alumina samples (HA & LA) in different combinations to produce three mixed oxide sets (HH, HL and LH) as shown in Table 2.2.

Table 2.2. Components of physical mixtures used in this study.

Acronym	**Component 1**	**Component 2**
HH	High SA of alumina (HA)	High SA of silica (HS)
HL	High SA of alumina (HA)	Low SA of silica (LS)
LH	Low SA of alumina (LA)	High SA of silica (HS)

Physical mixture samples were prepared by weighing and then thoroughly mixing masses of individual component to obtain a set of samples with known nominal surface compositions (Equation 2.9). Thus each surface fraction value corresponds to a mass fraction value related by Equation 2.9[3]. For HH samples where component surface areas are reasonably similar, surface area fractions closely resemble those of mass fraction. However, for the remaining two sets, alumina mass fractions were in fact different i.e., lower (HL) or higher (LH) than their corresponding surface fractions. Overall surface loading (SL) was set at 12,500m^2/l for silica-alumina physical mixtures.

[3] A physical mixture of 50% alumina (by surface) corresponds to
For HH: $\frac{gm\ of\ alumina}{gm\ of\ silica} = \frac{f_{Al}}{SA_{Al}} \times \frac{SA_{Si}}{f_{Si}} = \frac{0.50}{157} \times \frac{182}{0.50} = 1.16 \equiv 53.7\%$ alumina by mass.
For HL: $\frac{0.50}{157} \times \frac{54}{0.50} \equiv 25.3\%$ alumina by mass ; For LH : $\frac{0.50}{33} \times \frac{182}{0.50} \equiv$ 84.8% alumina by mass.

$$\text{mass of k component} = \frac{\text{surface fraction of k} \times \text{SL} \left[\frac{m^2}{g}\right] \times \text{volume[ml]}}{1000 \times \text{SA of k} \left[\frac{m^2}{g}\right]} \quad \textbf{Equation 2.9}$$

Dry physical mixture of each composition was contacted with aqueous solutions of fixed volume (30ml) placed in 60ml polypropylene bottles. The solutions were prepared between 1-12 pH ($pH_{initial}$) by adding HCl or NaOH. After adding measured amount of support to the solution the resultant slurry was allowed to settle for 1 hour in the shaker. This was followed by measuring the pH (pH_{final}) again. A standard pH electrode (Orion® 3-star benchtop) was used with 3-point calibration to record solution pH (detail specification in Chapter 1). Calibration of the pH meter was performed using standard pH solutions (pH=4,7 and 10). Thus obtained pH_{final} vs. $pH_{initial}$ data were plotted for each set of samples at each component mass fraction (pH shift plot). Each pH shift plot offered a plateau at a certain pHfinal value which is then noted as the point of zero charge (PZC) of that set at that composition [20]. Experiment was performed at least 3 times for reproducibility and standard deviation values are included as error bars in individual plots.

2.5.2 Characterization

2.5.2.1 BET

BET was performed with an ASAP 2020 Micrometrics apparatus.

2.5.2.2 X-ray Photoelectron Spectroscopy (XPS)

XPS was conducted using a Kratos AXIS Ultra DLD system equipped with a monochromatic Al Kα source operated at 15keV and 150W. The pass energy was fixed at 160eV for the survey scans. A charge neutralizer (CN) was used to compensate for the surface charge.

2.6 Results and Discussion

2.6.1 PZCs and ASCs of Physical Mixtures

The data fitting method that was followed to obtain oxide charging parameters (N_k, ΔpK and PZC) for individual oxides has been detailed elsewhere [28]. Experimental pH shift data have been presented in Figure 2.3, for a number of aluminas and silicas at two different surface loadings. Best fits to this data can be obtained with either a one parameter fit of the data (for ΔpK, taking PZC at the experimental plateau and using N_k from the literature), or by allowing all three parameters to vary. These are connoted as "1P" and "3P" respectively. Yet a third way to fit the data is to use parameters typically employed in the literature (connoted as "typ"). The fits with these three sets of parameters are also shown in Figure 2.3, and the derived parameters and the corresponding percentage error in fitting are given in Table 2.3.

Table 2.3. Critical parameter (PZC, ΔpK, N_s) values used in this study.

Sample	PZC	ΔpK	N_s	Error [%]
HA 1P	8.3	3.76	8.0	2.3
HA 3P	8.2	3.94	8.1	2.2
HA typ	8.3	5.0	8.0	2.9
HS 1P	3.6	6.75	5.0	1.2
HS 3P	3.5	6.84	5.04	1.6
HS typ	3.6	7.0	5.0	1.3
LS 1P	3.5	5.99	5.0	2.3
LS 3P	2.9	6.8	3.53	1.2
LS typ	3.5	7.0	5.0	2.3
LA 1P	8.2	3.04	8.0	5.5
LA 3P	8.4	4.65	8.02	5.2
LA typ	8.2	5.0	8.0	6.2

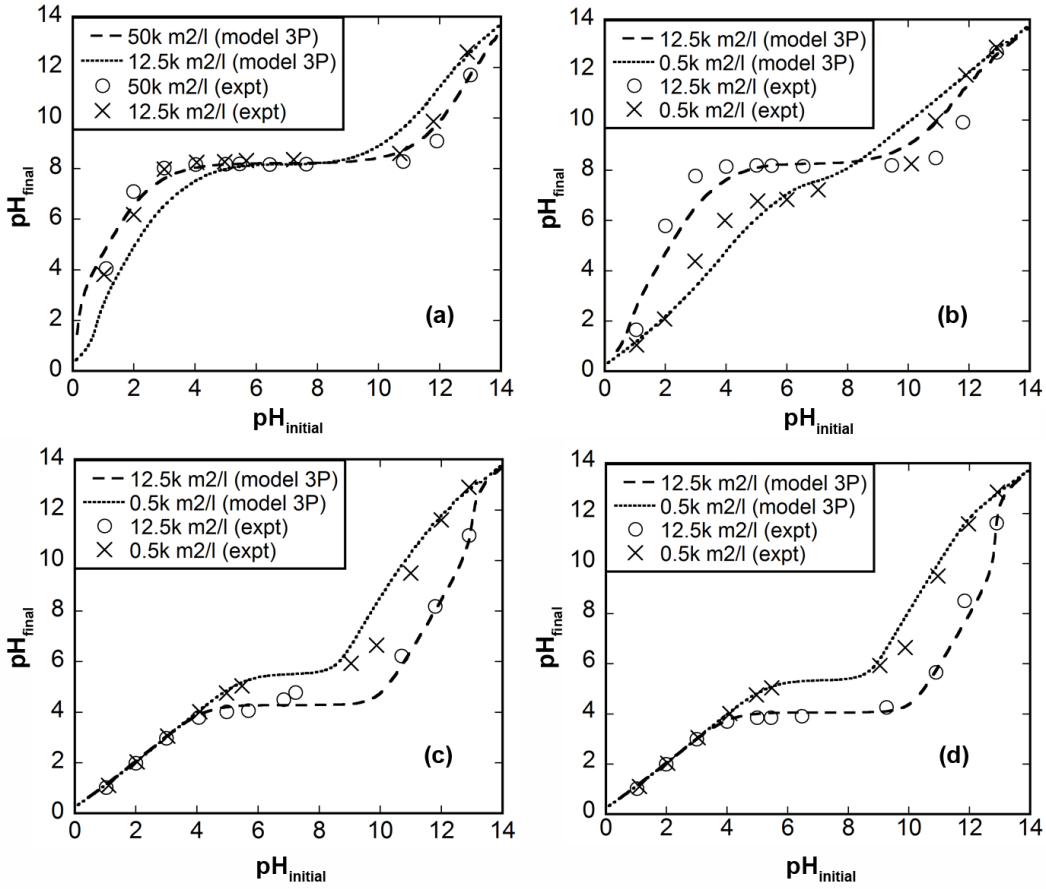

Figure 2.3. pH shift data over pure silica and pure alumina samples at different surface loadings (500 and 12,500m^2/l) : (a) HA, (b) LA, (c) HS and (d) LS. Experimental data were best fitted with model 3P to obtain values of three surface parameters (ΔpK, N_k and PZC).

Using the pure oxide parameters in the 2-surface model, pH shifts were then predicted for various physical mixtures of silica and alumina. These were compared to experimentally measured PZC values of the three different sets (HH, HL and LH) in Figure 2.4a-c. Model predictions with the three sets of parameters (1P, 3P, and typ) are shown for each set of physical mixture. The 2-surface model offers reasonable agreement with the experimental data in all sets (HH, HL and LH) regardless of component SA. However, some level of interaction, which is quite common between these two oxide components could be the potential source of deviation. Nevertheless, such deviation, if any, was small.

Fits of the 3P parameters are slightly better than the other sets (also seen in Table 2.3). All three data sets are S-shaped, most pronounced in the mixture of low SA alumina with high SA silica (LH in Figure 2.4c) which was similar to the findings of Schwarz et al. [49].

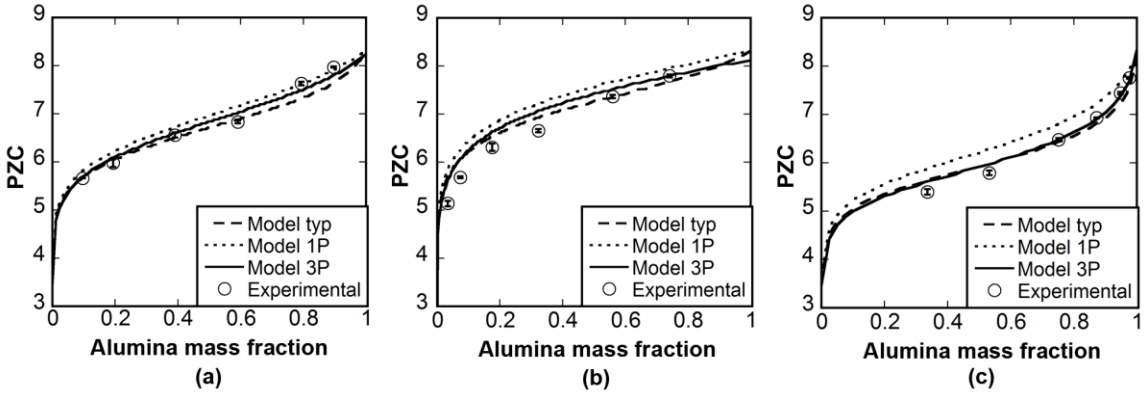

Figure 2.4. PZC vs. nominal Al_2O_3 mass fraction plots comparing simulation results with experimental data for (a) HH, (b) HL and (c) LH physical mixture sets.

Figure 2.5 (a-c) shows ASC vs. mass fraction correlations for the three alumina-silica physical mixtures (HH, HL and LH). Z values were calculated from Equation 2.8 using the respective 3P parameter values in Equation 1.2 and 1.3. ASC values were then calculated using the experimental PZC data from Figure 2.4 in Equation 2.7 and plotted as open circles in Figure 2.5. Z values are plotted on the right hand y-axis. The surface coverage of the control samples, labeled "From BET" in Figure 2.5 were derived from BET surface areas of pure component. The ASC data predicted from the pure oxide parameters fits the control samples reasonably well even for large differences in component surface area (HL and LH). When the surface area of the two components is about equal, the ASC-mass fraction relationship is approximately linear. When the surface areas are appreciably different, the ASC-mass fraction curves are bowed up or down.

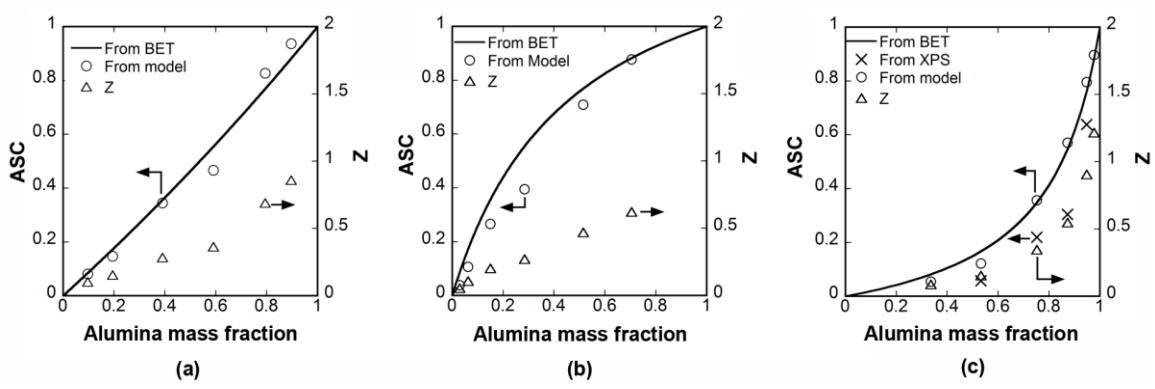

Figure 2.5. Actual and simulated ASC values of alumina for (a) HH, (b) HL and (c) LH physical mixtures of alumina and silica. Charging parameter (ΔpK, N_k and PZC) values were obtained from 3-parameter (3P) optimization for corresponding mixture components as listed in Table 2.3 and already used to obtain Model_3P plots in Figure 2.3. Z values obtained from Equation 2.8 for corresponding ASC are also plotted. XPS was used for LH sample only and the data is presented in (c).

For further confirmation, surface fraction values were determined using X-ray Photoelectron Spectroscopy (XPS) for the LH data set in Figure 2.5c. This set of data agrees reasonably well with the control data set and the predicted ASC values obtained from the 2-surface model. The XPS data yields ASC data a little on the low side, perhaps due to the photoelectron escape depth being deeper for the less dense (high SA) silica phase.

2.6.2 2-surface model on experimental data from literature

The 2-surface model was utilized to simulate experimental data of physical mixtures obtained from literature. In one study, performed by Schwarz group, PZCs of physical mixtures of silica and alumina with differing compositions were measured by mass titration [49]. In the same study they have also estimated the values of critical parameters which were used in 2-surface model to simulate their data (Figure 2.6a). From the results, 2-surface model exhibited reasonable agreement with their data.

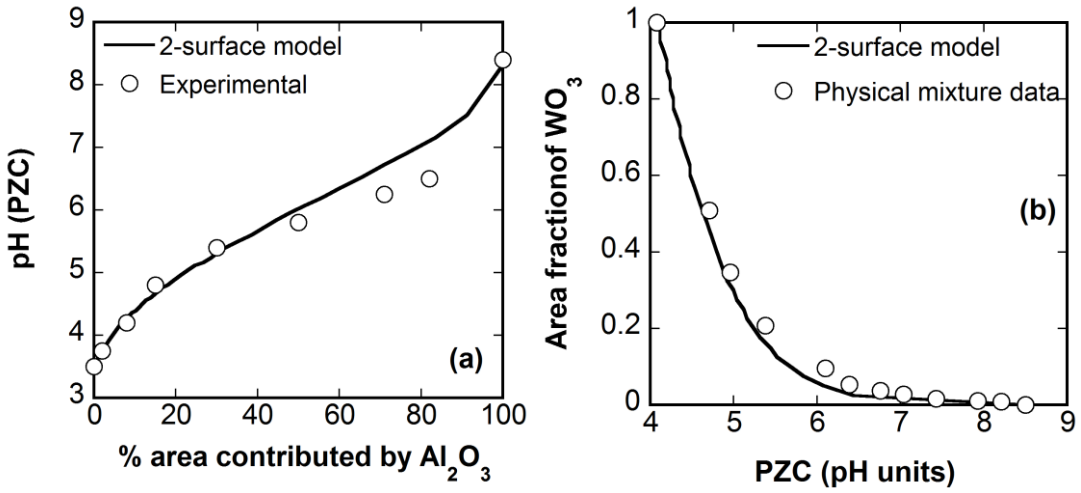

Figure 2.6. (a) Physical mixture data obtained by Schwarz group [49] simulated using 2-surface model with N_s=2.7 , ΔpK=5.18 (for alumina) and N_k=1, ΔpK=0.68 (for silica). (b) Physical mixture of alumina and tungsten oxide data of Schwarz group [48] simulated using 2-site model with N_k=2.7, ΔpK=5.18 (for alumina) and N_k=10, ΔpK=1 (for tungsten oxide). Values of the critical parameters were extracted from the respective studies.

Finally, in another study the same group performed similar analysis on mixtures of alumina and tungsten oxide (WO_3) [48]. Additionally, they proposed a polynomial equation consisting of terms obtained from non-linear regression as a model to simulate the experimental data. For comparison we have simulated the same set of data using our 2-surface model. For the critical parameter values of alumina we used the same values as we had in Figure 2.6a (N_k=2.7 and ΔpK=5.18). However, since the values for tungsten oxide were not reported in any of the studies performed by their group we have used independent pH shift analysis similar to that shown in Figure 2.3 and found that the values of N_s and ΔpK that fit the pH shift data of WO_3 most accurately were 10 and 1 respectively and hence they were used during 2-surface model simulation. Figure 2.6b shows the result which again exhibited reasonable agreement with the data.

2.6.3 2-surface model on composites with interacting components

In another independent study, 2-surface model has been successfully implemented on some bound oxide extrudates containing sulfated zirconia with alumina binders [63]. ASC values estimated by the 2-surface model for those extrudates revealed higher coverage of alumina on the surface than their bulk compositions dictated. This was speculated to be due to dissolution of Al on the surface in presence of acids during the synthesis of these extrudates. Additionally, these ASC results were shown to correlate well with catalyst reactivity in a C_5, C_6 isomerization reaction which verified our justification of neglecting interactions between components [63].

However, there are often cases where interaction between components in a mixed oxide would be too high to neglect. This can potentially complicate the characterization of surface of such a mixed oxide using 2-surface model. Such interactions, as have been widely reported in literature, include heterocoagulation, co-precipitation and dissolution from one solid and adsorption onto another [64]. Various models have been proposed to account for such interactions [65, 66]. Acid sites generated at the interface between two oxides (e.g., silica and alumina) could be used here as an example. In this study, a set of aluminosilicate mixed oxides, either synthesized in-house (AlSi-50, AlSi-380) or procured commercially (SIRAL), have been used as representative of acidic composites. Detail about these composites and their characterization results will be discussed in Chapter 3. Nevertheless, surface coverage of each of these composites was determined using two different techniques: XPS and 2-surface model. The resulting values have been listed in Table 2.4. From the listed values in Table 2.4 several advantages as well as limitations of using XPS or 2-surface model can be ascertained.

Table 2.4. Estimation of alumina surface coverage [area%] of composites.

Al-Si composite	Bulk alumina [area%]	Surface coverage (Al_2O_3, area%)	
		Via XPS	Via 2-surface model
AlSi-50	1.0[1]	5	45
AlSi-380	2.8[1]	10	16
SIRAL 80	20.2[2]	28	3
SIRAL 70	30.8[2]	25	3
SIRAL 40	60.7[2]	57	10
SIRAL 20	79.6[2]	83	35

[1]From ICP-OES, [2]From manufacturer provided information

As has been already discussed previously, XPS is not strictly surface sensitive (sampling depth = 2-10 nm). Hence, for the synthesized composites (e.g., AlSi-50 and AlSi-380) where very thin and highly dispersed alumina domains formed over silica (results presented in Chapter 3) it is likely that XPS detected more of the bulk silica and recorded as such. On the other hand, 2-surface model being strictly surface sensitive it was able to record composition more exclusively from the surface. Deposition of Al over Aerosil®OX50 silica (resulted in AlSi-50 mixed oxide) shifted the PZC from 4.0 (silica) to 7.0 (composites), which translates to about 45% alumina coverage according to the PZC method.

Discrepancy between XPS and model's prediction still existed as we go down the list of values in Table 2.4. For the commercial aluminosilicate composites (SIRAL) with higher density of acid sites, 2-surface model revealed a much higher surface coverage of silica than XPS. Here it should be noted that interactions such as presence of (stronger) Brønsted acid sites at the interface between the silica and alumina and their subsequent effect on PZC are not accounted for in 2-surface model. Presence of strong(er) Brønsted acid sites is expected to create a permanent (or at least extending over a broad pH range) negative surface charge. Therefore, measured PZCs of silica-alumina composites with

reasonable acid site densities may translate to a significantly higher coverage of the low PZC component (e.g., silica in this case). Interestingly, surface coverage values estimated by XPS were close to bulk fractions (listed in Table 2.4), as expected from the high penetration depth of XPS in light materials. In order to characterize these composites with acid sites better an alternative method will be discussed in Chapter 3.

2.7 Conclusion

Several mixed oxide systems were characterized using the proposed 2-surface model. However, it should be noted that this technique is limited to high oxide loadings. In studies that necessitate low oxide content e.g., electrophoretic mobility dramatic shift in pH is not observed. Also there were some cases where the interaction between two phases might cause deviations. Next step would be to accommodate for such interactions in our 2-surface model and apply on systems where such interactions prevalently occur. The conclusions for this study are as follows:

[1] For composite materials with different PZCs it is possible to measure surface composition with pH measurements. This simple and accurate method can be applied to a wide variety of mixed oxides.

[2] Developed 2-surface model was successfully used to reproduce various data obtained from literature.

[3] Limitation of 2-surface model has been shown in cases where pH measurements are affected by other factors e.g., presence of acid sites.

2.8 Future work

Using this model other system of mixed oxides could be evaluated. Also, modification in the model in order to account for the interaction between components could improve the applicability of this model in many systems of mixed oxides

Chapter 3

The controlled synthesis of metal-acid bifunctional catalysts: Selective Pt deposition and nanoparticle synthesis on amorphous aluminosilicates

3.1 Introduction

Mixed oxides constitute an important class of materials in heterogeneous catalysis due to their vast applications in organic synthesis, petroleum industry and green chemistry [67]. Many of these processes benefit from the new functionalities that these mixed oxides incorporate into the catalytic system. Aluminosilicates, for example, contribute via their acid sites and hence play a major role in petroleum and oil refining applications [68].

Noble metals (e.g., Pt) deposited over aluminosilicates are widely studied as metal-acid bifunctional catalysts where aluminosilicates supply the acid function and noble metal nanoparticles provide a dehydrogenating/hydrogenating function [69-73]. In this domain the focus has recently been mostly directed towards testing new materials with different structures, acid strength and composition [74-81]. However, the synergy by menas of balance and proximity between these two types of active sites is often ignored partly due to the lack of control during catalyst synthesis [82-85].

In this study, we have explored the potential to control the location and mechanism of Pt adsorption over mixed oxides through the choice of metal precursor and simple pH adjustment. The underlying principle and hypothesis have been depicted in Figure 3.1 and will be elaborated in the subsequent sections. Following objectives were determined for this study.

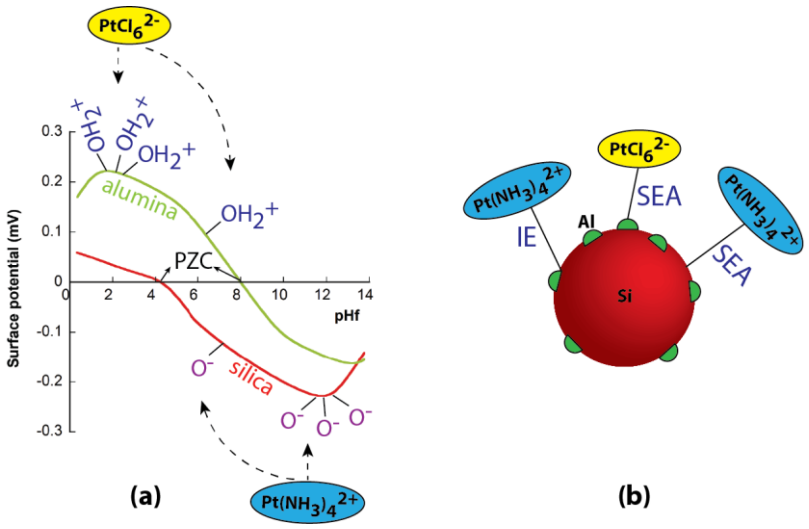

Figure 3.1. (a) Theoretical surface potential versus adsorption pH (pH_f) plot for silica (PZC = 4.25) and alumina (PZC = 8.0). Theory (pH shift model) has been elaborated in Chapter 1. (b) Simplistic depiction of selective metal ion adsorption over silica-alumina mixed oxide (Green patches are alumina domains deposited over red silica particles).

1. Study of pH directed metal precursor adsorption onto physically mixed oxides.
2. Characterization of metal deposited physically mixed oxides.
3. Synthesis and procurement of amorphous aluminosilicates.
4. Study of pH directed metal precursor adsorption over aluminosilicates.
5. Characterization of metal deposited aluminosilicates.

The experimental schemes designed to fulfill these objectives have been summarized in Table 3.1. For objective 1, cationic and anionic Pt precursor adsorption surveys over physical mixtures of silica and alumina with very dissimilar sizes were conducted. For objective 2, these Pt deposited physical mixtures were reduced and characterized for selective Pt adsorption. Physical mixtures of a nonporous silica and a nonporous alumina with dissimilar sizes were ideal samples to image under the microscope. For objective 3, synthesized composites of silica and alumina and commercial amorphous aluminosilicates were characterized to analyze their surface morphology and

acid sites. Particularly, the mixed oxide composites synthesized on a nonporous silica with 40nm average particle size added to the ease of characterization via imaging. For objective 4, similar series of experiments as in objective 1, were performed on these mixed oxides to study metal adsorption over them. For objective 5, sizes of the Pt nanoparticles following reduction of the precursors have been quantified using several techniques.

Table 3.1. Experimental schemes of this study.

Objective(s)	**Experiment(s)**	**Expected outcome(s)**
1	Cationic and anionic Pt precursor uptake versus pH surveys over physical mixtures of silica and alumina	Electrostatic and predictable Pt uptake over physically mixed oxides
2	STEM imaging on selected Pt/silica-alumina physical mixtures	Demonstration of selective Pt deposition
3	Synthesis and characterization using (a) NH_3-TPD, (b) ^{27}Al NMR and (c) XEDS mapping of aluminosilicates	Aluminosilicates with small patches of alumina domains
4	Same as Objective 1, but over aluminosilicates	Understanding the nature of Pt adsorption over aluminosilicates
5	(a) XRD, (b) STEM and (c) Chemisorption of Pt deposited over aluminosilicates prepared at different conditions	Effect of preparation method on the size of Pt nanoparticles

The main contributions of this research are:

(1) Selective metal deposition onto mixed metal oxides.

(2) Simple method to quantify alumina surface coverage of aluminosilicates.

3.2 Synthesis of mixed oxides for heterogeneous catalysis

Mixed oxides frequently feature in the study of heterogeneous catalysis as supports or promoters to enhance catalytic performance [86]. Depending on the methods by which they are synthesized, mixed metal oxides can impart different functionalities. Hence, it is often beneficial to find the most effective route to synthesize mixed metal oxides for certain catalytic application. Most common methods to synthesize mixed metal oxides include, co-precipitation, sol-gel and grafting of metal alkoxides on surface OH groups [87].

Based on the synthesis method and condition, the level of intimacy between components of mixed oxides can be controlled. For example, in commercial zeolites, molecular level of interaction between Si and Al is established. This renders strong and abundant acid sites in zeolites suited for certain applications. On the contrary, many amorphous aluminosilicates, prepared differently, could offer composite surface consisting of well-defined alumina and silica domains and their interfacial sites, the combination of which could aid in many other applications [88, 89].

3.3 Metal deposition strategies over mixed oxides

Impregnation is one of the most common methods of metal deposition over mixed oxides. However, with a typical impregnation technique, little or no control over the location of metal deposition can be established. More specifically, over mixed oxides with strong acidity e.g., zeolite, ion exchange is one of the most widely used techniques of metal deposition [90]. This special group of mixed oxides carrying electric charge in their crystalline lattice requires charge compensating oppositely charged ions for the stability of the overall system. As for example, in zeolites when an Si^{4+} from its crystalline framework is replaced by Al^{3+} it creates an electric charge at their interface which is stabilized by the

incorporation of a charge compensating ion e.g., Na^+, NH_4^+. In ion exchange method of catalyst synthesis, these compensating oppositely charged ions are further exchanged with metal precursor ions from a solution [91].Hence ion exchange method could be limited by the type of metal precursor ions and the availability of ion exchange sites [1, 92].

Utility of ion exchange mechanism on zeolites had been extensively studied. Due to the resulting strong metal precursor-support interaction this method can eventually lead to well-dispersed metal nanoparticles at the nearest proximity of the acid sites of zeolites [93]. However, role of ion exchange mechanism in catalyst prepared over moderately acidic mixed oxides e.g., amorphous silica-alumina has often been overlooked. This might be due to the inexplicability of the nature of acid sites on these amorphous mixed oxides [89]. Over amorphous silica-alumina supports dry impregnation (DI) or incipient wetness impregnation (IWI) or wet impregnation (WI) method without any pH adjustment and using cationic metal precursor ions e.g., $Pt(NH_3)_4^{2+}$ had been reported numerous times to yield well dispersed metal particles [79, 94]. Quite possibly, the acid sites retained by amorphous silica-alumina used in these studies promoted ion exchange with the cationic metal precursor ions. This might have played a significant role in the improvement of metal dispersion, which was not often confirmed due to lack of systematic study and reliable characterization techniques.

Since ion exchange mechanism triggers adsorption at the acid sites (preferentially at the protonic sites), it is anticipated that acidity of the resulting catalysts will be affected. Also, it has been reported that the nature, strength and number of acid sites in silica-alumina mixed oxides can be affected by factors e.g., solution pH and metal loading [79, 95]. These observations further complicate the evaluation of the effect of ion exchange mechanism.

3.4 Potential of SEA over mixed oxides

In Chapter 1 (Section 1.3.1), the concept of SEA applied over single oxides has been discussed at length. It has been shown there that in order to develop enough surface charge for electrostatic adsorption, prior pH adjustment is necessary. As a result, a low PZC material e.g., silica can adsorb cationic metal precursor ions at high pH whereas a high PZC material e.g., alumina would hold considerable surface charge to adsorb anionic metal precursor ions at low pH.

However, as silica and alumina are brought together in the form of mixed oxide, individual phase domains, depending on its PZC and density of hydroxyl groups would provide surface for electrostatic adsorption. This will be more applicable to amorphous aluminosilicate materials where well-defined silica and alumina domains are present [89]. In addition to that, any acid site generated at the interface between silica and alumina would supply potential for ion exchange of cationic metal precursor. Difference in the nature and selectivity of metal ion adsorption with respect to the pH and type of precursor ions have been hypothesized and depicted in Figure 3.1. Thus with cationic metal uptake over acidic silica-alumina mixed oxides contributions from ion exchange mechanism could be envisaged in addition to SEA. Iamoto and his coworkers first reported that at high pH copper (II) 'excessively' exchanged on zeolite which was over the amount dictated by the ion exchange [96]. Later, Schreier et al. observed similar findings using cationic $Pt(NH_3)_4^{2+}$ and $Cu(NH_3)_4^{2+}$ precursors over three different zeolites [97]. In their study, they attributed these 'overexchanged' cationic metal uptakes to the cumulative contributions from electrostatic and ion exchange mechanism.

SEA can have vast implications on the rational design of catalysts over mixed oxides. Due to different nature of the individual oxides there would be a range of pH where metal precursor ions with certain charge types would preferentially adsorb onto one oxide than another (Figure 3.1). Feltes et al. synthesized Mn-Co/TiO_2 bimetallic catalysts using this principle. In this case, Mn was selectively adsorbed on to Co_3O_4 particles and not onto the TiO_2 support [98]. Zečević et al showed that selective Pt adsorption can be established on microporous zeolites with alumina binders which enabled them to study catalytic performance by varying proximity between active sites [93]. Zha et al. used cationic Pt precursor and different charging behavior of niobia and alumina to selectively adsorb Pt onto niobia domains of a niobia-alumina mixed oxide [99]. These results offer strong foundation for pH directed selective adsorption study over silica-alumina mixed oxides.

3.5 Materials and Methods

3.5.1 Materials

All the materials used in this study have been listed in Table 3.2.

Table 3.2. Different materials, their specifications and purpose.

Commercial name	**Purpose**	**Supplier**	**Assay**
Aerosil®380 silica	Phys. mix. Component and parent silica for Al deposition	Evonik-Degussa	PS=7nm,SA=380m^2/g
Nanodur® γ-alumina	Phys. mix. Component	Nanodur	PS=40nm, SA=37m^2/g
Aerosil®OX-50 silica	Parent silica for Al deposition	Evonik-Degussa	PS=50nm, SA=54m^2/g
Puralox SBa200 γ-alumina (Al-1)	Reference alumina support	Sasol, Germany GmbH	SA=190m^2/g
Aluminum chloride	Formation of charged Al polytcations	Sigma-Aldrich	≥99%

hexahydrate ($AlCl_6.6H_2O$)			
SIRAL 20-80	Commercial silica-alumina	Sasol, Germany, GmbH	(Table 3.3)
Platinum tetraammine chloride, $Pt(NH_3)_4Cl_2$	Cationic Pt precursor	Aldrich Chem Co.	98%
Chloroplatinic acid, H_2PtCl_6	Anionic Pt precursor	Aldrich Chem Co.	99.9%

PS=Particle size

3.5.1.1 Components of physical mixture

A model, nonporous silica (Aerosil® 380) and a model, nonporous γ-alumina (Nanodur®) with contrasting particle sizes (Table 3.2) were used in the study of physical mixtures.

3.5.1.2 Synthesis of silica-alumina

The silica-alumina mixed oxides (commonly referred to as "Al-Si") were either synthesized in-house or obtained commercially. The in-house synthesis was based on a method prescribed elsewhere [100, 101] and has been elaborated with a schematic diagram in Figure 3.2. Briefly, a clear solution containing Al polycations ($[Al_{13}O_4(OH)_{24}(H_2O)_{20}]^{7+}$, denoted Al_{13}^{7+}) was prepared. Within 30 min of preparation, silica (~0.1m^2 silica/μmole of Al in solution) was contacted to this solution and shaken on an orbital shaker for 1h. During this time part of the Al_{13}^{7+} polycations in solution electrostatically adsorbed onto silica [102]. Following filtration and drying, the Al_{13}^{7+} deposited silica supports were calcined at 550°C for 3h. One high surface area (Aerosil® 380) and one low surface area (Aerosil® OX50) silica were used. Both were pre-calcined at 550°C for 5h prior to Al_{13}^{7+} deposition which resulted in the reduction of surface area of Aerosil® 380 silica to 240m^2/g. These

Al_{13}^{7+} deposited (and calcined) Aerosil® 380 and Aerosil® OX50 silicas will be referred to as AlSi-380 and AlSi-50 respectively.

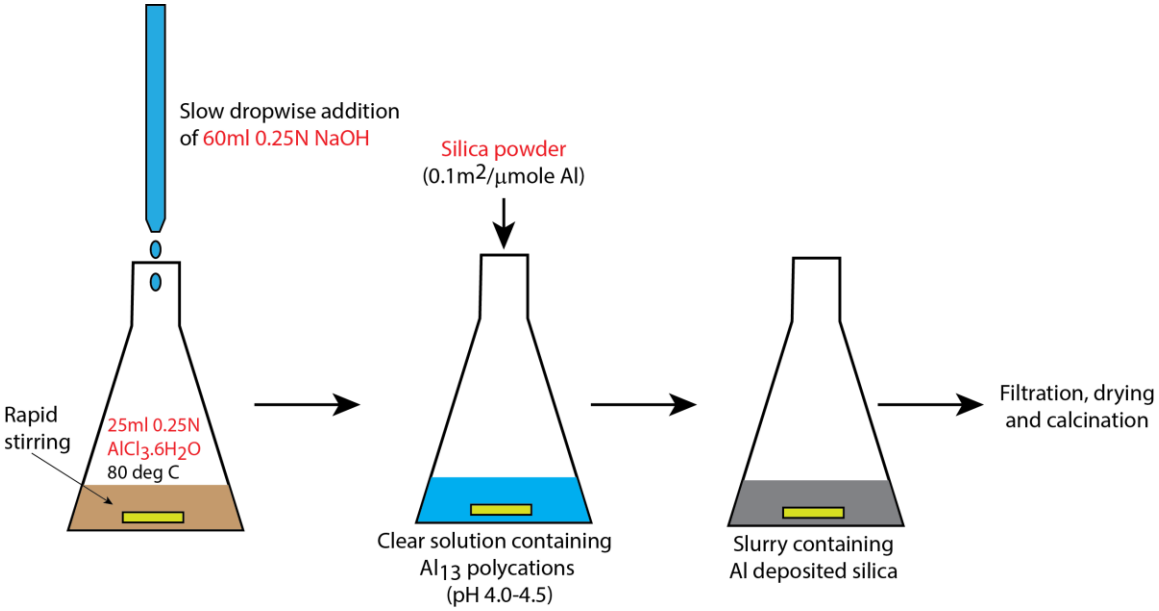

Figure 3.2. Schematic diagram showing recipe to synthesize Al-Si.

Four commercial Al-Si (SIRAL 20, SIRAL 40, SIRAL 70 and SIRAL 80) provided by Sasol, Germany GmbH were also studied. Each SIRAL sample ID number represents the bulk concentration [wt%] of silica. These SIRAL samples were originally synthesized using a patented procedure [103] involving hydrolysis of aluminium hexanolate in hexanol (6wt% Al) solution with deionized water at 90°C followed by mixing the filtered alumina suspension with orthosilicic acid (3wt% SiO_2) solution. The resulting mixed gels (pseudo-boehmite) were subsequently spray-dried. By varying the amount of orthosilicic acid used, samples containing different silica content were prepared. Before Pt deposition, both sets (commercial and synthesized) of Al-Si samples were washed 3 times with 0.2M NH_4NO_3 solution (150 ml/2.5 g sample) to ion exchange Na, if present, from the acid sites. This was

followed by calcination in air at 550°C for 3h at 2°C/min ramp rate to obtain the acid form of the catalyst.

Additionally one γ-alumina sample (Al-1) was used to study acidity and metal dispersion on pure alumina supports. This alumina is commercially synthesized via activation of boehmite phase.

3.5.1.3 Adsorption experiments

Platinum tetraammine chloride, $Pt(NH_3)_4Cl_2$ (98%) and chloroplatinic acid, $H_2PtCl_6.6H_2O$ (99.9%) were used as cationic and anionic precursors of Pt, respectively. Both were obtained from Sigma-Aldrich in powder form.

Unless otherwise noted equilibrium adsorption experiments were conducted at 500m^2/l surface loadings (SL = total surface area of material in solution). At first, a series of pH (initial pH, pH_i) adjusted aqueous solutions (fixed volume) with known amount of dissolved Pt precursors were prepared and subsequently contacted with the support to reach the desired SL. The resulting slurries were then left on an orbital shaker for 1h after which their final pHs (pH_f) were recorded. Finally, each slurry solution was filtered using 0.2 □m syringe filters to collect ~5ml of the filtrate solution, which was analyzed using Inductively Coupled Plasma (ICP-OES) apparatus. Pt adsorption uptake was calculated from the difference in Pt concentration in solution before and after addition of support.[4]

Langmuir isotherms were developed for anionic $PtCl_6^{2-}$ adsorption over different single and composite oxides. In this experiment, for each support up to four $PtCl_6^{2-}$ solutions with different platinum concentrations (50-500 ppm i.e. mg/liter and equivalent

[4] Calculation of Pt uptake in μmoles/m^2 :
Initial (pre-adsorption) Pt conc. C_i ppm, final (collected filtrate after adsorption) Pt conc. = C_f ppm
Pt uptake [μmoles/m^2] = $\frac{(C_i - C_f)[\frac{mg}{liter}] \times 1000}{MW_{Pt}[\frac{gm}{mole}] \times SL\ [\frac{m^2}{liter}]}$

to 0.00025-0.0025mol/liter) were prepared. The concentrations were chosen such that the equilibrium (post-adsorption) Pt concentration was ≤ 250ppm. Also in order to maintain constant ionic strength, all the experiments were conducted in presence of a background electrolyte (e.g., $NaNO_3$). The concentration of 0.0075N was found to be enough to keep the ionic strength constant without being too high to significantly affect the adsorption capacity. The initial pH values were adjusted such that the final pH was that for maximum adsorption of $PtCl_6^{2-}$ on that particular support. Adsorption constants were determined from best fits of the Langmuir isotherm.

3.5.2 Catalyst pre*p*aration

Following adsorption surveys Pt loaded catalysts were prepared at specific adsorption pHs (pH_f). After metal adsorption, the filtered solid was dried at room temperature overnight under vacuum and then reduced at 350°C for 1h in a 10% mixture of H_2/Ar (total flow rate 200ml/min). Catalysts were also prepared via dry impregnation (DI). In this method, the amount of $Pt(NH_3)_4Cl_2$ required for specific Pt loading was dissolved in the amount of de-ionized water (no prior pH adjustment) necessary to fill the pore volume of the support. After synthesis the catalysts were dried and reduced at the condition described above. Reduced samples were subsequently characterized with different techniques e.g., XRD, Chemisorption, STEM, the specifics of which are described below.

3.5.3 Catalyst characterization

3.5.3.1 XRD

Powder XRD was performed using a Rigaku MiniFlexII bench-top system fitted with a Rigaku D/tex Ultra silicon strip detector [104]. The radiation source was Cu Kα

radiation (λ = 1.5406 Å) at operating condition of 30kV and 15mA. All spectra were taken at a scan rate of 1°/min and sampling width of 0.02°. Pt particle size was calculated using Scherrer formula with negligible instrument line broadening (shape factor = 0.94).

3.5.3.2 H_2 Pulse Chemisorption

Chemisorption was performed using hydrogen pulse titration of oxygen precovered Pt (Micromeritics Autochem II 2920 automated analyzer). First, approximately 0.1g of catalyst sample was fully reduced in flowing 10% H_2/Ar gas mixture at 350°C for 1h. This was followed by pure Ar flow at 350°C for 0.5h (to remove chemisorbed H). Following cooling of the catalyst to 40°C in Ar flow, it was exposed to 10% O_2/He for 0.5h to ensure saturation with adsorbed atomic oxygen and then purged with pure Ar for 0.5h to remove residual O_2. Pulses of H_2/Ar were initiated at this point to replace adsorbed oxygen with atomic hydrogen and form H_2O. Hydrogen consumption was quantified via a calibrated, high sensitivity thermal conductivity detector (TCD). H_2 Pulsing was continued until no further H_2 uptake. The overall stoichiometry of Pt to H_2 was assumed to be 0.667:1 [27]. Particle sizes were estimated assuming hemispherical geometry.

3.5.3.3 STEM imaging

High angle annular dark field (HAADF) images were obtained using an aberration-corrected JEOL JEM-ARM200CF (200kV electron) scanning transmission electron microscope (STEM). The instrument has an imaging resolution as low as 0.078nm and energy resolution 0.35eV. ImageJ software was used to redraw and admeasure ~1000 Pt particles on the resulting HAADF images which yielded a representative statistical distribution of particle size. Both surface ($d_{s,EM} = \Sigma n_i d_i^3/\Sigma n_i d_i^2$) and volume ($d_{v,EM} = \Sigma n_i d_i^4/\Sigma n_i d_i^3$) average particle sizes were calculated which were subsequently compared

with chemisorption ($d_{s,chemi}$) and XRD ($d_{v,XRD}$) particle sizes respectively. Additionally, elemental maps of Pt, Al and Si were generated using X-ray energy dispersive spectroscopy (XEDS) acquired through an Oxford Instruments X-Max100TLE SDD detector fitted to the JEM-ARM200CF at the University of Illinois at Chicago.

3.5.3.4 NH_3-TPD

NH_3-temperature-programmed desorption (TPD) was conducted on different supports in a Micromeritics Autochem II 2920 automated analyzer equipped with a thermal conductivity detector (TCD). 0.2g of sample was first pretreated in 50ml/min He flow for 1h at 500°C. NH_3 adsorption was initiated at 150°C by flowing 2%NH_3/He at 50ml/min for 0.5h which was followed by purging with He flow at the same temperature and flow rate for 0.5h to remove physisorbed NH_3. After that temperature ramping was initiated under He flow at 10°C/min ramp rate for up to 500°C.

For the NH_3-TPD experiments on the Pt loaded catalysts an additional *in situ* reduction step (350°C, 1h in 50ml/min flow of 10% H_2/He) was included at the beginning. This was followed by increasing the temperature up to 500°C in flow of He and maintaining the sample at this temperature for 1h. This additional treatment did not affect the metal dispersion of the catalysts, as was verified separately using H_2 pulse chemisorption.

3.5.3.5 ^{27}Al NMR

^{27}Al NMR spectra were obtained on an Avance 500 spectrometer (Bruker). Samples were fully rehydrated prior to measurement. The conditions for the ^{27}Al NMR spectra were: rotor external diameter 4mm, single pulse detection, Larmor frequency 130.33 MHz, pulse length 5.3μs, recycle delay 1 s and spinning rate 12kHz. A 0.1M solution of aluminum nitrate was used as the 0 ppm reference.

3.5.3.6 XPS

XPS was conducted on the composites to determine component surface fraction using a Kratos AXIS Ultra DLD system equipped with a monochromatic Al Ka source operated at 15keV and 150W. The pass energy was fixed at 160eV for the survey scans. A charge neutralizer (CN) was used to compensate for the surface charge.

3.6 Results

3.6.1 Selective Pt adsorption over single oxides and their physical mixtures

Anionic $PtCl_6^{2-}$ and cationic $Pt(NH_3)_4^{2+}$ uptake surveys over pure components and physical mixtures of silica and alumina in presence of an excess of the platinum precursor are presented in Figure 3.3. Adsorption studies over silica (denoted as Q_s) and alumina (denoted as Q_a) were conducted at SL = 500m^2/l (open circles and open squares in Figures 3.3a and b). These can be interpreted in light of the surface potential plot presented in Figure 3.1. In the acidic pH range, anionic $PtCl_6^{2-}$ adsorption over silica was almost negligible whereas over alumina high uptake was observed (Figure 3.3a). This was due to the development of high positive surface potential over alumina in the acidic pH range as shown in Figure 3.1. Over silica, surface potential was too insignificant to carry on electrostatic adsorption. On the contrary, at higher pH, according to Figure 3.3b, away from their respective PZCs, negative surface potentials over silica and alumina enable them to adsorb cationic $Pt(NH_3)_4^{2+}$. However, due to significantly higher potential in the basic pH range (see Figure 3.1), $Pt(NH_3)_4^{2+}$ adsorption capacity over silica was nearly 3 times as high as over alumina.

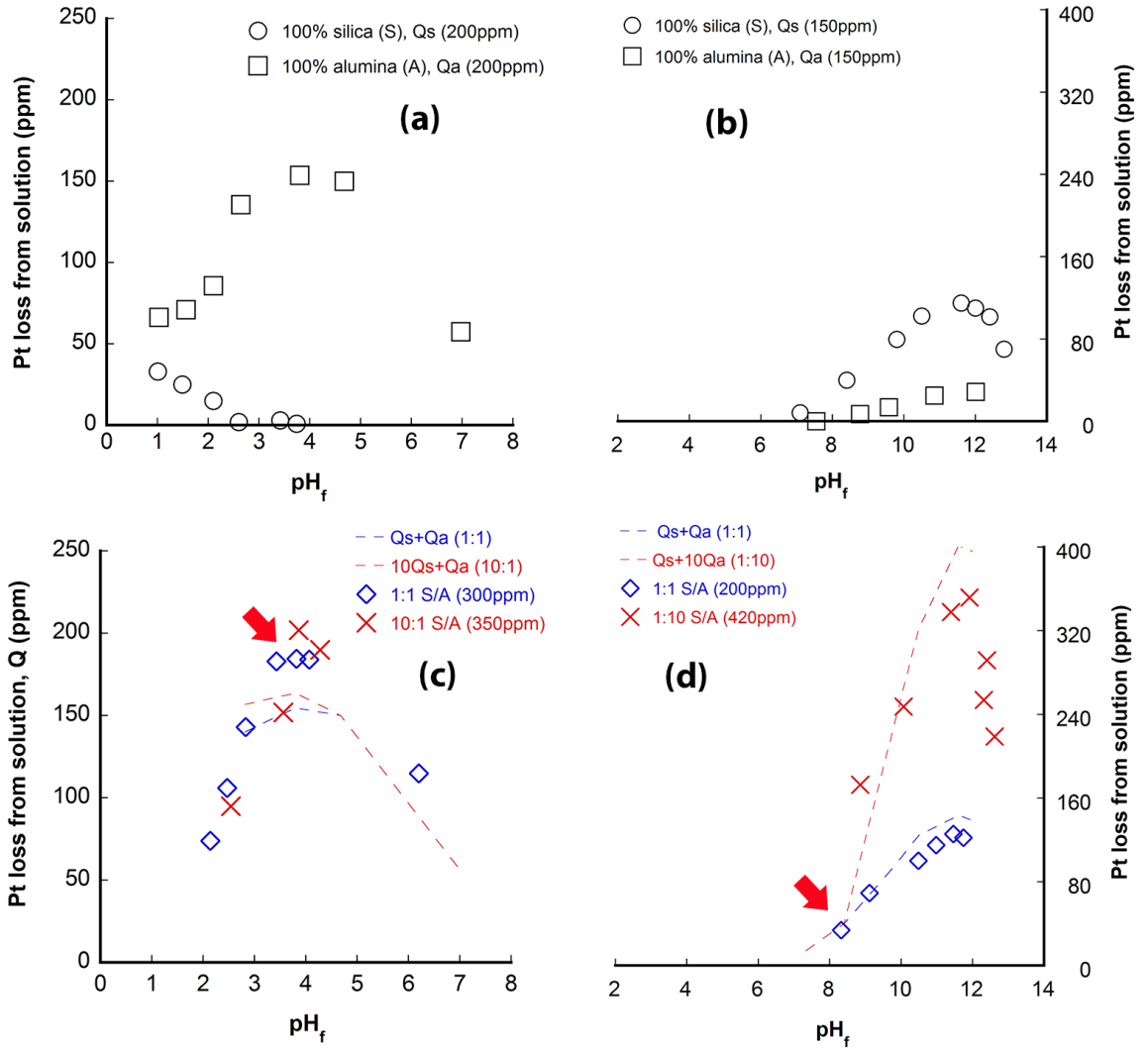

Figure 3.3. Pt complex adsorption surveys over pure and physical mixtures of silica (S) and alumina (A): (a) Anionic $PtCl_6^{2-}$ over single oxides, (b) cationic $Pt(NH_3)_4^{2+}$ over single oxides, (c) Anionic $PtCl_6^{2-}$ over physical mixtures and (d) Cationic $Pt(NH_3)_4^{2+}$ over physical mixtures. Initial ppm (mg/L) concentration of Pt present in the solution for each experiment is included in the legend. Dashed lines in (c,d) represent data extrapolated from single oxide uptakes. Two red arrows indicate selected samples (open diamonds) that were analyzed with STEM.

Next, $Pt(NH_3)_4^{2+}$ and $PtCl_6^{2-}$ adsorption studies were conducted over physical mixtures of silica and alumina with surface area ratios of 1:1, 1:10 and 10:1. In order to maintain these ratios SLs of $1000m^2/l$ (500+500), $5500m^2/l$ (500+5000) and $5500m^2/l$ (5000+500) were used. Measured uptake data over physical mixtures were also presented

in Figures 3.3c and d. In parallel to this, the component oxide uptakes based on the uptake of the pure components (Figure 3.3a,b) were extrapolated to the area ratio of the studied physical mixture. These were presented as dashed lines in Figures 3.3c and d. A reasonably close agreement was observed between the measured uptake over physical mixtures and the extrapolated uptake.

Following uptake survey experiments, two samples from 1:1 physical mixture series were dried, reduced and imaged with high resolution STEM (Figure 3.4). These two samples (indicated with arrows in Figures 3.3c and d) were selected for the demonstration of selective Pt adsorption. Contrasting particle sizes of component oxides (inset of Figure 3.4a) offered easy visual identification of different phases of the physical mixture from the STEM images. In the adsorbed $PtCl_6^{2-}$ series in Figure 3.3c, the sample synthesized at pH_f=3.9 (uptake corresponding to 3.7wt% Pt) over 1:1 physical mixture was chosen for STEM imaging. For this sample, according to Figure 3.4a, Pt° particles are mostly present on the alumina domains (large spherical particles) indicating that $PtCl_6^{2-}$ adsorbed selectively onto alumina. On the other hand, from adsorbed $Pt(NH_3)_4^{2+}$ series illustrated in Figure 3.3d, the sample obtained at pH_f=8.3 over the 1:1 physical mixture (open diamond) was imaged. Pt uptake corresponded to 0.7wt% for this sample. It is evident from the Figure 3.3d that, at this $pH_{f,,}$ $Pt(NH_3)_4^{2+}$ adsorption, albeit low, occurred almost exclusively over silica. This was confirmed from the STEM image in Figure 3.4b.

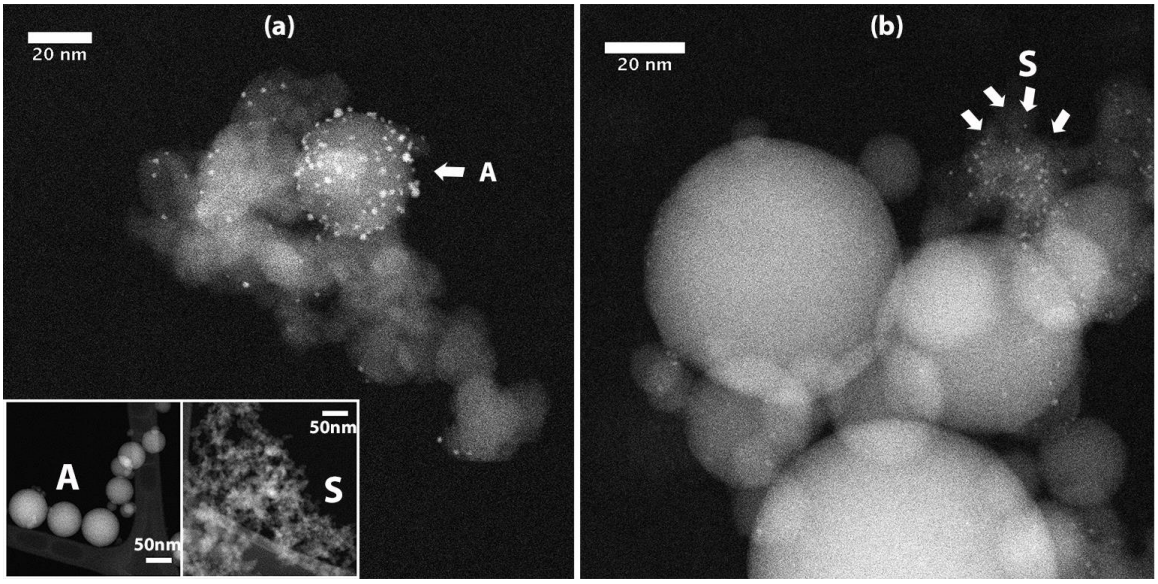

Figure 3.4. STEM images of (a) $PtCl_6^{2-}$ (3.7wt% Pt, pH_f=3.9) and (b) $Pt(NH_3)_4^{2+}$ (0.7wt% Pt, pH_f=8.3) over 1:1 physical mixtures. Inset of Figure (a) shows images of contrasting sizes of model and nonporous alumina (A) and silica (S) particles.

3.6.2 Characteristics of Al-Si supports

All six Al-Si supports were calcined at 550°C/3h before characterization and subsequent use. The characterization results of the calcined samples are in Table 3.3.

Table 3.3. Physico-chemical characteristics of Al-Si supports.

Support	**SA [m^2/g]**	**Bulk Al_2O_3 [%]**	**Al_2O_3 domain size [nm]**	**PZC**	**Total acidity[3] [μmoles/g]**
AlSi-50	54	1.0[1]	≤1.5	7.0	22
AlSi-380	240	2.8[1]	≤1.5	5.6	142
Al-1	190	100	4.0	8.1	220
SIRAL 80	320	20.2[2]	≤1.5	4.5	290
SIRAL 70	239	30.8[2]	≤1.5	4.4	198
SIRAL 40	379	60.7[2]	2.4	5.0	283
SIRAL 20	278	79.6[2]	3.0	6.4	333

[1]calculated from measured Al concentration before and after deposition using ICP-OES, [2]Analytical data provided by the manufacturer, [3]Error in acid site count by NH_3-TPD ±10%

XRD profiles of calcined Al-Si supports are shown in Figure 4a. Patterns of pure silica and pure γ-alumina supports were also included for comparison. Only the Al-rich samples (SIRAL 40 and SIRAL 20) displayed γ-alumina peaks in their respective XRD

patterns. Here it must be noted that SIRAL Al-Sis originally come as uncalcined samples and, in agreement to this, the XRD patterns of these Al-rich Al-Si supports showed clear evidence of the boehmite phase prior to calcination at 550°C (XRD patterns in Figure D.1 in the Appendix). Upon calcination, boehmite transformed completely to γ-alumina on these supports as shown in Figure 3.5a. On the other hand, most of the Si-rich Al-Si supports, including SIRAL 80, AlSi-50, AlSi-380 did not show any evidence of alumina or boehmite phase before or after calcination in their respective XRD patterns. From their respective XRD profiles the γ-alumina peaks at (400) and (440) were used to determine the size of alumina domains. These values are listed in Table 3.3.

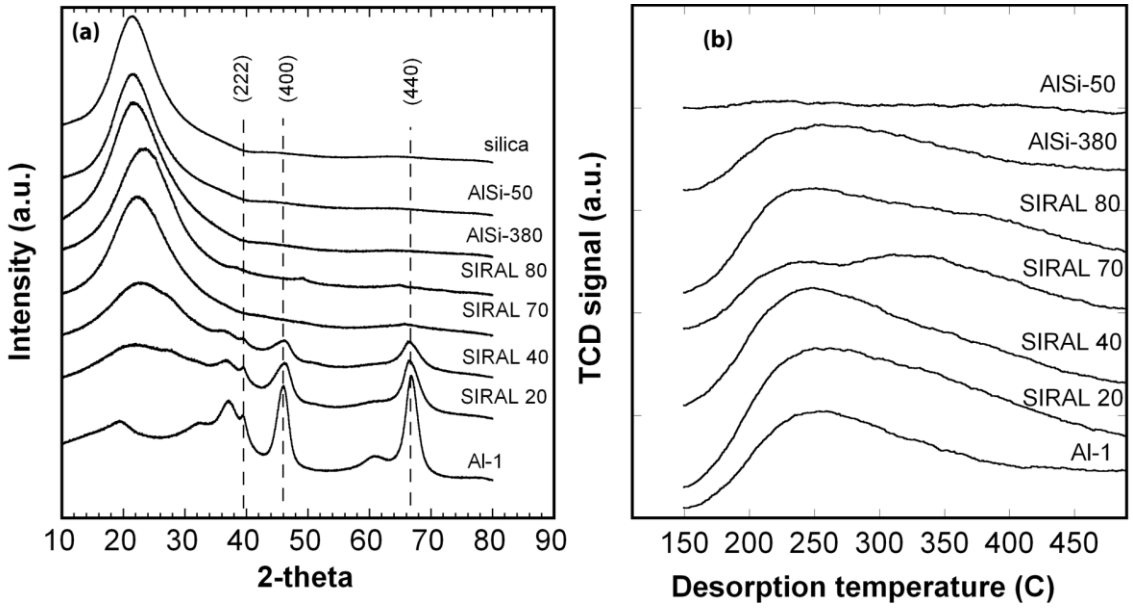

Figure 3.5. (a) XRD and (b) NH_3-TPD desorption profiles of pure oxides and Al-Si samples. Patterns are ordered with respect to increasing alumina content from top to bottom.

NH_3 desorption profiles of the Al-Si samples (0.2g) compiled in Figure 3.5b were used to quantify the total number of acid sites (Table 3.3). The desorption signal of AlSi-50 was very weak compared to the others due to its low surface area (Table 3.3). All other

Al-Si samples exhibited NH_3 desorption peaks at ~250°C which might be largely due to presence of alumina-like domains. Indeed, no NH_3 desorption peaks for pure silica (not shown) and a single peak at similar temperature for pure γ-alumina (Al-1) corroborate this possibility (Figure 3.5b). An additional desorption peak at higher temperature (300-400°C) is more noticeable on silica rich supports e.g., SIRAL 80 and SIRAL 70.

As it was not possible to confirm the presence of alumina-like domains on the Si-rich Al-Si samples (AlSi-50, AlSi-380, SIRAL 70 and SIRAL 80) from their respective XRD patterns, elemental mapping (Al and Si) was performed on one of these samples, namely AlSi-50 (Figure 3.6a). We selected this sample due to the regular structure and nonporous nature of Aerosil® OX 50 (fumed silica spheres of about 40nm) that would greatly facilitate its imaging. It was expected that adsorption of the Al_{13}^{7+} Keggin precursor on silica would form alumina-like domains of ~1 nm (average size of Al_{13}^{7+} Keggin precursor). However, from elemental mapping, alumina domains were found to be in a much more dispersed state over silica. The very small size of these domains explains why they were not be detected by XRD. Furthermore, ^{27}Al NMR study of the AlSi-380 sample (an Al-Si sample similar to AlSi-50 but prepared using Aerosil® 380 fumed silica with higher surface area and therefore a higher Al content, which makes this sample more convenient for characterization by ^{27}Al MAS NMR) revealed the presence of four (~54ppm) and five (30-35ppm) coordinated aluminum which confirmed interaction between Si and Al [68]. It also revealed the presence of Al atoms in an octahedral environment (~0ppm), which indicates the presence of alumina-like domains. For comparison, the ^{27}Al MAS NMR spectrum of SIRAL 80 is also shown in Figure 3.6d. It is also composed of 3 NMR signals whose positions are similar to those observed on the

spectrum of AlSi-380 but with different relative intensities. Although ^{27}Al NMR cannot be used for a quantitative assessment of the Al distribution, one can safely conclude that the difference in the proportions of 4, 5 and 6 coordinated Al in these two samples reflects the difference in the size of the alumina domains for these two samples, the larger domains of SIRAL 80 resulting in a higher proportion of 6-coordinated Al.

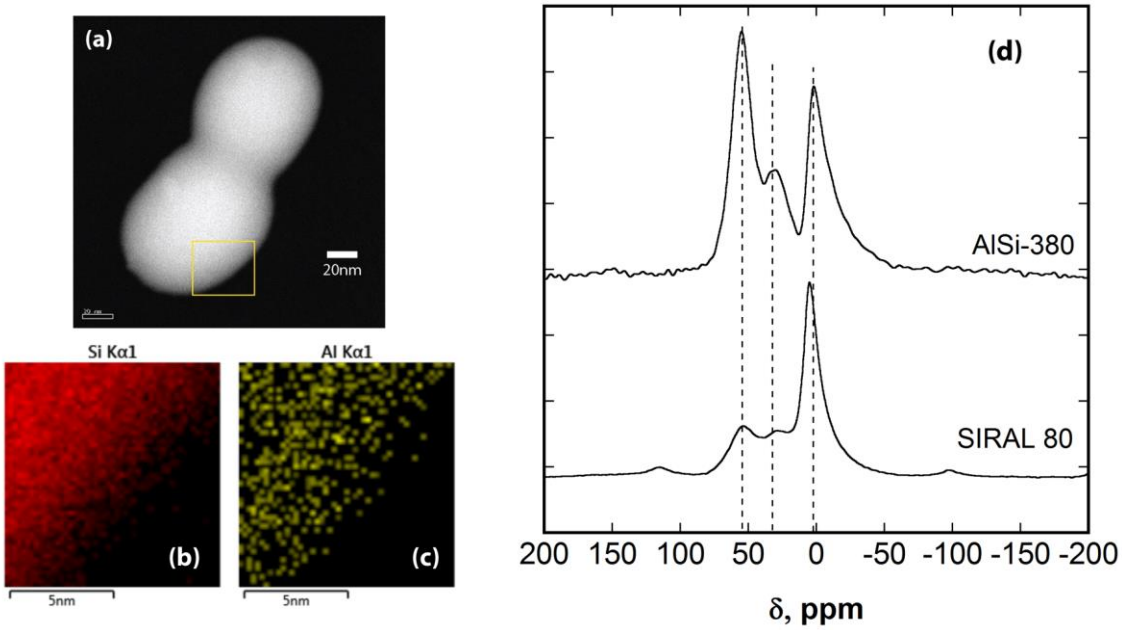

Figure 3.6. (a) STEM micrograph of AlSi-50. (b-c) Elemental maps of Si (b) and Al (c) of the bounded area shown in (a). (d) ^{27}Al NMR profiles of synthesized (AlSi-380) and commercial (SIRAL 80) Al-Si.

3.6.3 Pt adsorption surveys over Al-Si

Anionic and cationic Pt uptake surveys were performed on the Al-Si supports. Pt uptake surveys over Al-Si's synthesized in lab are compiled in Figure 3.7I and 3.7II whereas Figure 3.7III contains uptake surveys over all commercial SIRAL calcined supports. The corresponding parent silica (either Aerosil® OX 50 or Aerosil® 380) over which Al_{13} polycations were deposited was used as the representative silica supports. Al-1 was used as representative alumina support.

For anionic $PtCl_6^{2-}$ adsorption over mixed oxides (Figure 3.7A), Pt uptake was in between the $PtCl_6^{2-}$ uptake over alumina and over silica. In this case, since $PtCl_6^{2-}$ adsorbed preferentially onto alumina domains, maximum Pt uptake very much depended on the alumina content on the surface of mixed oxide. This can be further noticed from Figure 3.7AIII. As alumina content is increased from SIRAL 80 to SIRAL 20, $PtCl_6^{2-}$ uptake approached that over pure alumina surface. In contrast, when comparing cationic $Pt(NH_3)_4^{2+}$ uptake over mixed and pure oxides (Figure 3.7B), a significant difference can be observed. Maximum $Pt(NH_3)_4^{2+}$ uptake over mixed oxides with fractional silica and alumina coverage was higher than over single oxides. This is more obvious in SIRAL supports (Figure 3.7BIII) that possess significantly higher number of acid sites than the synthesized Al-Si materials. These observations hint towards multiple adsorption mechanisms (e.g., ion exchange and strong electrostatic adsorption) over the Al-Si supports which will be discussed later.

Adsorption isotherms were studied for $PtCl_6^{2-}$ adsorption onto the different Al-Si supports. Uptake of $PtCl_6^{2-}$ (τ, $\mu moles/m^2$) is plotted against equilibrium concentration of Pt in the solution (C_{eq}, ppm) in Figure 3.8a. For each isotherm, the metal precursor uptake reached a plateau indicating that maximum adsorption on that support has been reached. The plateau also indicates that ionic strength of the solution was reasonably constant and not high enough to cause any retardation in metal uptake.

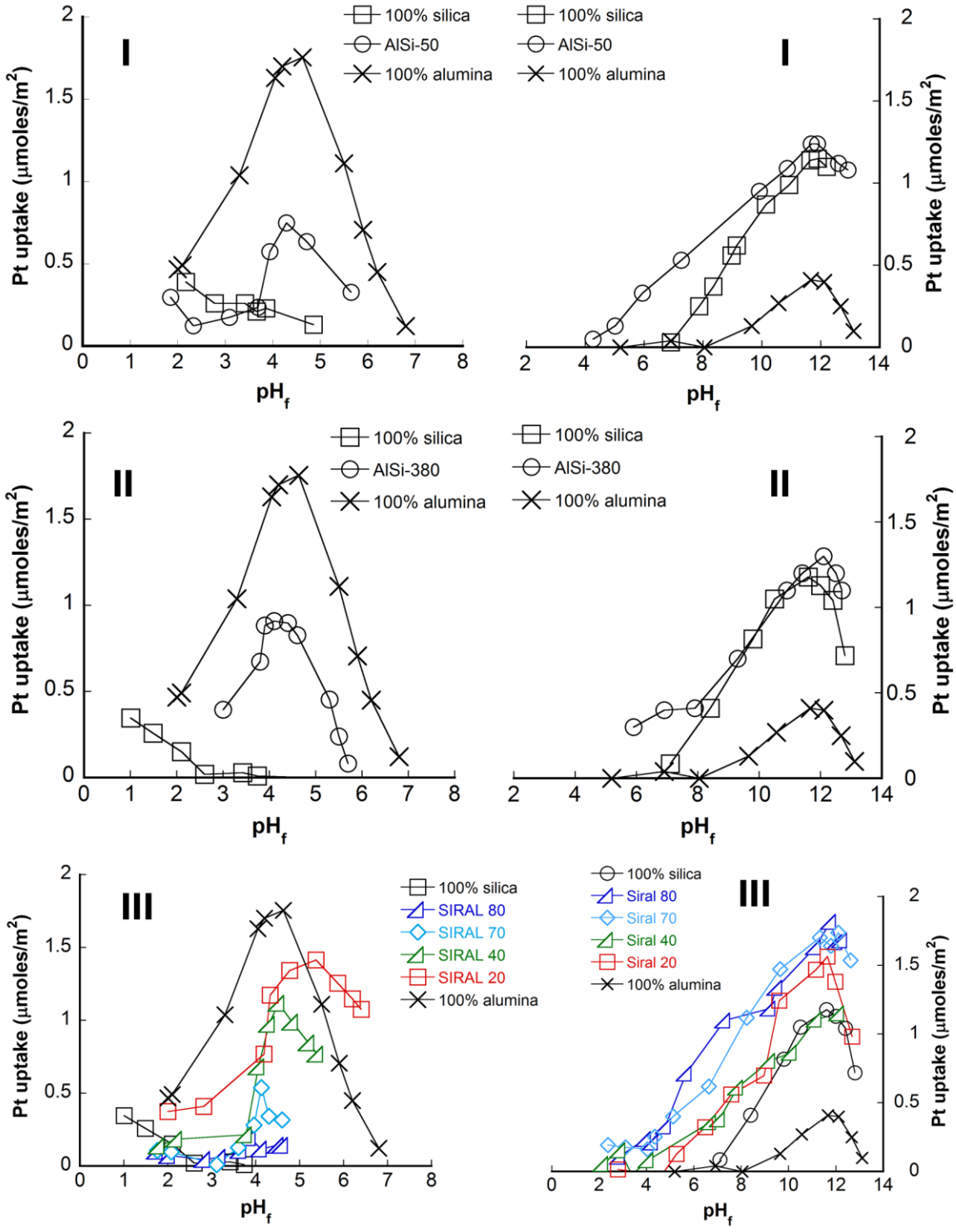

Figure 3.7. Anionic $PtCl_6^{2-}$ (A) and cationic $Pt(NH_3)_4^{2+}$ (B) adsorption onto (I) AlSi-50, (II) AlSi-380 and (III) Commercial (SIRAL) supports. Initial Pt concentration = 200ppm (mg/L). SL=1000m^2/liter. For comparison, the platinum complex uptakes on 100% silica (Aerosil 380 used for part BIII) and on 100% alumina (Al-1) have also been represented

In Figure 3.8b, the ratios of adsorbed (C_{ads}) to equilibrium (C_{eq}) Pt concentration versus C_{eq} show, for all samples, linear correlation in agreement to the Langmuir model. The Langmuir parameters extracted from these plots are listed in Table 3.4.

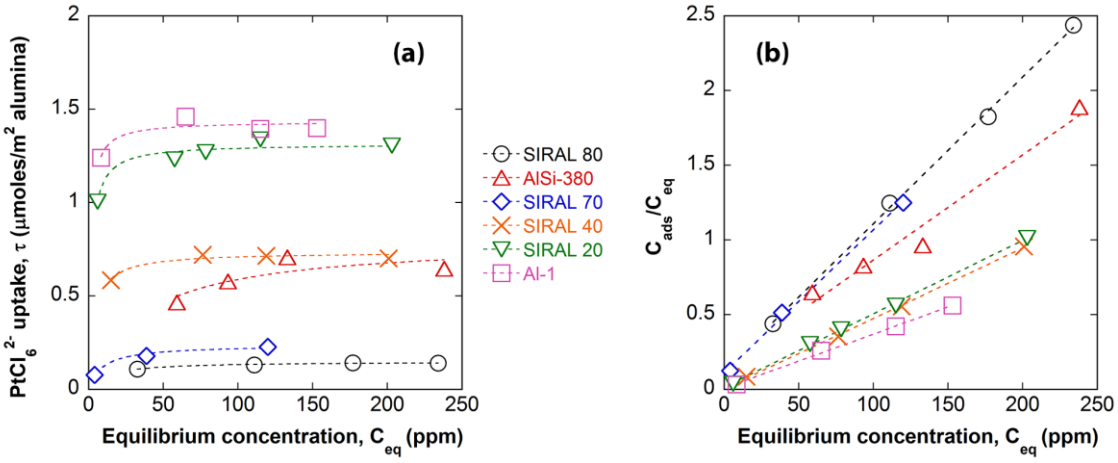

Figure 3.8. (a) Raw data and (b) linear fitting plots of Langmuir isotherms for $PtCl_6^{2-}$ adsorption over pure alumina (Al-1) and over Al-Si supports.

Table 3.4. Parameters obtained from Langmuir isotherm in Figure 3.8.

Support	pH_f	Maximum adsorption, [μmoles/m^2]	Adsorption constant, k [liter/mg]	Goodness of fit (R^2)
SIRAL 80	4.0	0.15	0.08	0.97
AlSi-380	4.4-4.5	0.8	0.03	0.70
SIRAL 70	4.0	0.24	0.11	0.98
SIRAL 40	4.0	0.73	0.27	0.94
SIRAL 20	4.4	1.3	0.54	0.94
Al-1	4.4-4.5	1.43	0.8	0.85

3.6.4 Characterization of reduced Pt/Al-Si

In order to control Pt location as well as adsorption mechanism, various Pt catalysts were synthesized over the Al-Si supports using different precursors ($Pt(NH_3)_4^{2+}$ or $PtCl_6^{2-}$) and pH of adsorption (pH_f). These catalysts were divided into four series:

(a) $Pt(NH_3)_4^{2+}$ adsorption at intermediate pH_f (6-8),

(b) $Pt(NH_3)_4^{2+}$ adsorption at high pH_f (11-12),

(c) $Pt(NH_3)_4Cl_2$ deposition via dry impregnation (due to strong buffering ability of the support, pH_f in this case will approach the PZC),

(d) $PtCl_6^{2-}$ adsorption at low pH (4.0-4.5).

A nominal 0.7wt% Pt loading was prepared in each series with each Al-Si support.

For series (a) samples, as it was difficult to adjust the final pH (pH_f) to a precise value (e.g., 7.0), a narrow range of intermediate pH_f (6-8) was deemed acceptable. Electrostatic adsorption of $Pt(NH_3)_4^{2+}$ over pure silica and alumina was almost negligible ($\leq 0.2 \mu moles/m^2$) in this pH range (Figure 3.7B) as expected from their respective PZCs. This, coupled with significant $Pt(NH_3)_4^{2+}$ uptake over the Al-Si supports in this pH range indicates that a non-electrostatic (presumably, ion exchange (IE)) adsorption would be the dominant adsorption mechanism here. On the contrary, series (b) and (d) represent electrostatically adsorbed samples using cationic $Pt(NH_3)_4^{2+}$ and anionic $PtCl_6^{2-}$ precursors respectively. To ensure a dominant role of electrostatic adsorption, pH_f was adjusted to a significantly higher (series b) or lower (series d) value than the PZCs of each component. An overlap with the non-electrostatic mechanism cannot be completely ruled out for the predominantly electrostatically adsorbed series (b) samples.

Following reduction, all the catalysts were characterized using XRD, chemisorption and STEM for the determination of the average Pt particle size (Table 3.5). Although originally intended for 0.7wt%, the actual metal loadings converted from Pt uptake varied moderately and have been listed in Table 3.5. Here it should be noted that XRD and chemisorption reveal volume ($d_{v,XRD}$) and surface ($d_{s,chemi}$) averaged particle sizes respectively [105]. These values were compared with the respective volume and surface averaged particle size obtained from STEM images. XRD profiles of representative

catalyst samples are presented in Figure 3.9. Profiles of Al-rich samples (SIRAL 20, SIRAL 40) were only included in the appendix (Figure D.3) due to overlapping Pt and γ-alumina peaks which made Pt particle sizing from XRD problematic. From Figures 3.9a and b and Table 3.5 it can be summarized that small, well-dispersed Pt over Al-Si catalysts could be prepared via IE (Series a) and SEA (Series b) of $Pt(NH_3)_4^{2+}$even for Al-rich Al-Si materials (SIRAL 40 and SIRAL 20) with no considerable difference in particle size between them. A representative STEM image of series (b) catalyst, shown in Figure 3.10a, confirms high dispersion of Pt particles for this series.

Table 3.5. Characteristics of 0.7wt% Pt/Al-Si catalysts.

Series	**%Pt**	**Precursor**	**Mechanism**	**pH_f**	**Particle size (nm)**			
					$d_{s,chemi}$ (D%[1])	$d_{s,EM}$	$d_{v,EM}$	$d_{v,XRD}$
AlSi-50								
a	0.75	$Pt(NH_3)_4^{2+}$	SEA	11.9	2.1 (54)	1.7	1.8	<1.5
b	0.70	$Pt(NH_3)_4^{2+}$	IE	8.0	2.2 (43)	2.1	2.1	<1.5
c	0.73	$PtCl_6^{2-}$	SEA	4.4	>10 (4)	Irr	Irr	3.0
d	0.70	$Pt(NH_3)_4Cl_2$	DI	-	>10 (11)	-	-	10.5
AlSi-380								
a	0.76	$Pt(NH_3)_4^{2+}$	SEA	11.7	1.7 (45)	-	-	<1.5
b	0.75	$Pt(NH_3)_4^{2+}$	IE	7.7	1.7 (65)	-	-	<1.5
c	0.72	$PtCl_6^{2-}$	SEA	4.4	>10 (6)	-	-	3.6
d	0.70	$Pt(NH_3)_4Cl_2$	DI	-	1.8 (59)	-	-	1.7
SIRAL 80								
a	0.66	$Pt(NH_3)_4^{2+}$	SEA	11.6	1.8 (62)	-	-	<1.5
b	0.66	$Pt(NH_3)_4^{2+}$	IE	6.3	1.7 (65)	-	-	<1.5
c	0.72	$PtCl_6^{2-}$	SEA	4.2	>10 (1)	Irr	Irr	2.9
d	0.70	$Pt(NH_3)_4Cl_2$	DI	-	2.7 (33)	-	-	2.9
SIRAL 70								
c	0.60	$PtCl_6^{2-}$	SEA	4.2	>10 (3)	-	-	4.7
SIRAL 40								
a	0.65	$Pt(NH_3)_4^{2+}$	SEA	11.5	2.5 (42)	-	-	ND
c	0.65	$Pt(NH_3)_4^{2+}$	SEA	4.2	2.9 (39)	-	-	ND
SIRAL 20								
a	0.71	$Pt(NH_3)_4^{2+}$	SEA	11.3	3.0 (37)	-	-	ND
c	0.72	$PtCl_6^{2-}$	SEA	4.4	2.8 (40)	2.9	4.1	ND
Al-1								

c	0.72	$PtCl_6^{2-}$	SEA	4.1	2.4	-	-	ND

Irr=Large particles, ND=Not determined (Presence of γ-alumina peaks on XRD prevents accurate determination of particle size).

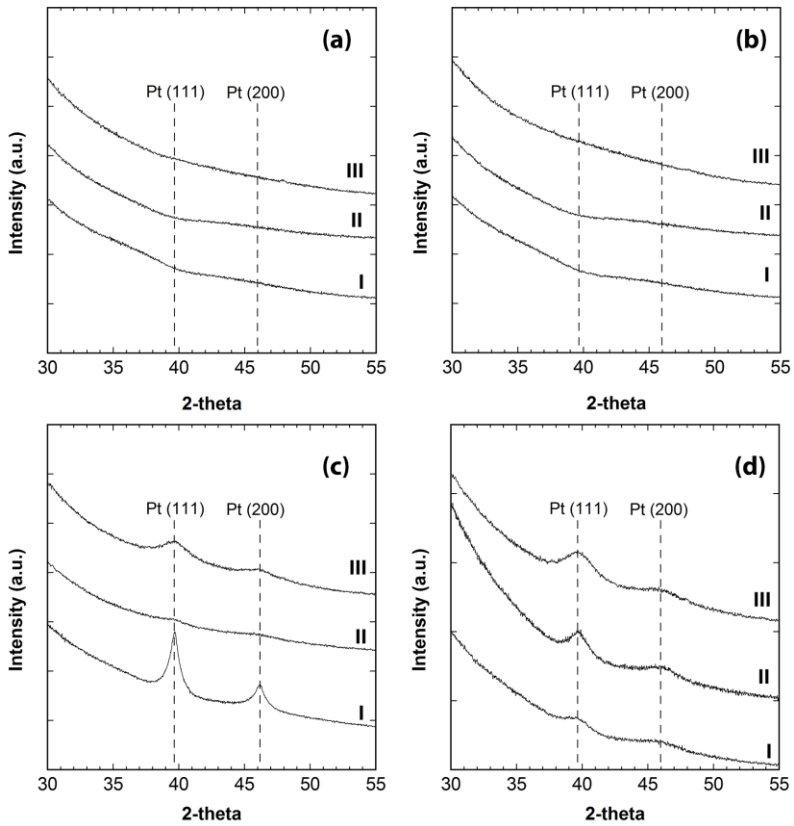

Figure 3.9. XRD patterns of 0.7% Pt/Al-Si catalysts over (I) AlSi-50, (II) AlSi-380 and (III) SIRAL 80 supports from a) PTA deposition at neutral pH (series a), b) PTA SEA at high pH (series b), c) $Pt(NH_3)_4Cl_2$ deposition via DI (series c), and d) $PtCl_6^{2-}$ SEA at low pH (series d).

Pt particle size of catalysts in series (c) prepared via DI method varied with support (Table 3.5 and Figure 3.9). A catalyst prepared over weakly acidic AlSi-50 support had the largest overall Pt particle size (>10nm) as verified from XRD and chemisorption (Table 3.5). However, over more acidic supports e.g., AlSi-380 and SIRAL 80, Pt particles were more dispersed. This hints at the possible role of ion exchange on Pt dispersion in this catalyst series. XRD and chemisorption on series (a), (b) and (c) catalysts showed excellent agreement in terms of Pt particle size (Table 3.5).

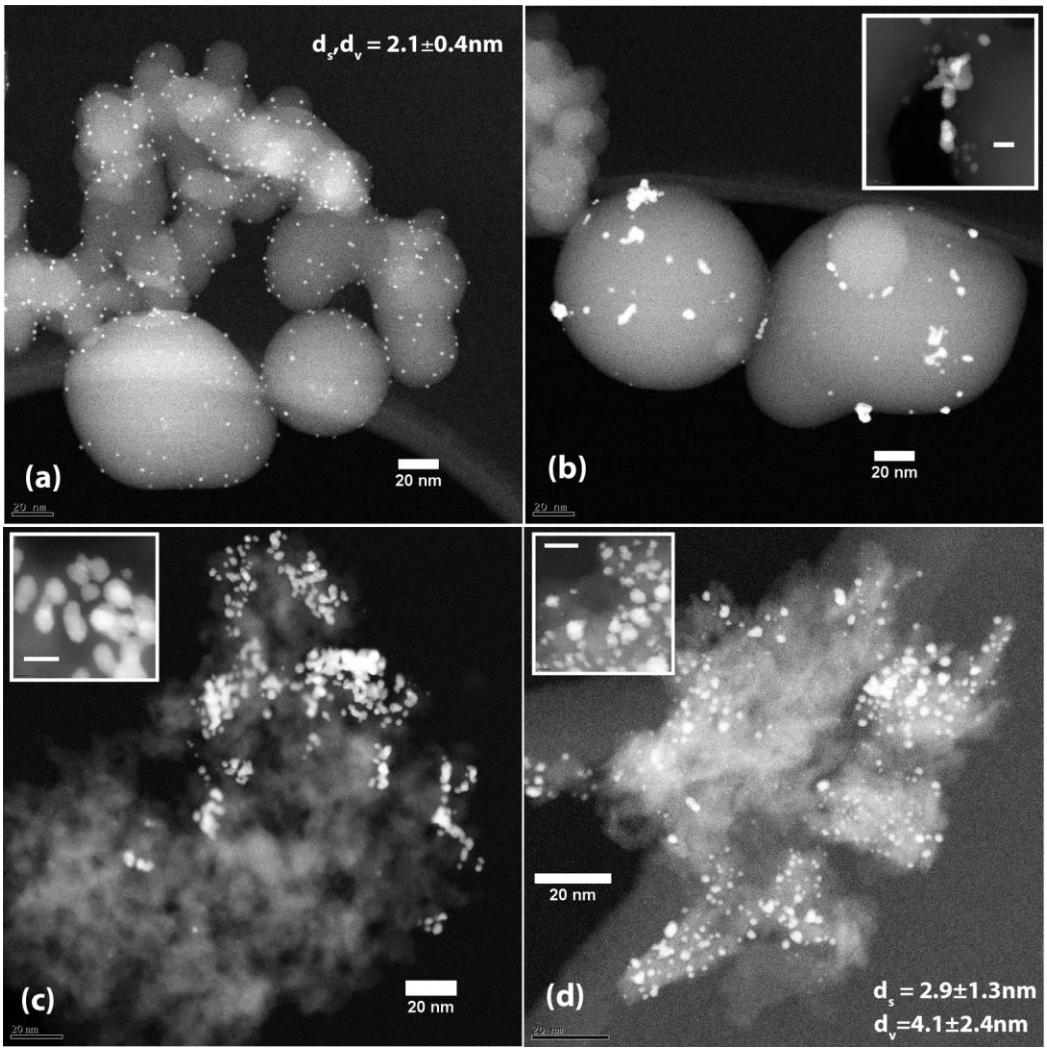

Figure 3.10. STEM images of 0.7% Pt over (a) AlSi-50 using $Pt(NH_3)_4^{2+}$ at pH_f=11.9 (series b), (b) AlSi-50 using $PtCl_6^{2-}$ at pH_f=4.4 (series d), (c) SIRAL 80 using $PtCl_6^{2-}$ at pH_f=4.2 (series d) and (d) SIRAL 20 using $PtCl_6^{2-}$ precursor pH_f=4.2 (series d). Inset of figure (b), (c) and (d) shows high magnification images (scale bar=5 nm).

Pt particle size of series (d) catalysts (SEA of $PtCl_6^{2-}$ at pH~4) showed a large discrepancy between XRD (3-4nm) and chemisorption (>10nm) sizes particularly for the Si-rich Al-Si supports (Table 3.5). STEM images of some of these catalysts confirmed very poor dispersion of Pt particles (Figures 3.10b and c). Moreover, higher magnification images (inset of Figures 3.10b and c) revealed that the irregularly shaped particles are comprised of aggregates of small Pt nanoparticles (of ~3 nm. This explains the discrepancy

between chemisorption and XRD particle size with the latter reflecting the size of the primary particles. However, in case of Al-rich Al-Si materials (SIRAL 20, SIRAL 40) Pt dispersion and particle size improved noticeably (Table 3.5 and Figure 3.10d). $PtCl_6^{2-}$ over pure γ-alumina (Al-1) yielded slightly lower Pt particle size in comparison with the Al-rich Al-Si samples (Table 3.5).

3.7 Discussion

3.7.1 Quantification of SEA versus IE over mixed oxides

In Figure 3.3, both cationic and anionic platinum complex adsorption surveys over physical mixtures showed reasonable agreement with the dashed lines extrapolated from the component oxides. This indicates that platinum uptake occurred almost exclusively by electrostatic adsorption. This was further verified from the STEM images in Figure 3.4. Thus, employing the right pH and metal precursor combination, one can achieve selective adsorption of platinum. Selective uptake prevailed even in presence of a large excess of the non-attractive component.

Schreier et al. observed that cationic Pt and Cu adsorption surveys over zeolites cannot be explained with a single adsorption mechanism [97]. They suggested that in addition to ion exchange at the Al exchange sites of zeolites, cationic Pt could also electrostatically adsorb onto silanol groups. Such a dual adsorption mechanism can be used to explain high overall $Pt(NH_3)_4^{2+}$ uptake over the SIRAL series (see Figure 3.7III (B)) for which a significant amount of acid sites can be expected based on NH_3-TPD results.

In order to isolate and quantify the role of each of these two mechanisms (SEA and IE) it is essential to know the component (alumina or silica) surface coverage on these Al-

Si supports. Surface coverage of each Al-Si was determined using three different techniques: XPS, PZC and $PtCl_6^{2-}$ uptake. Each of these techniques has its own limitations:

- XPS is not strictly surface sensitive (sampling depth = 2-10 nm) [106]. Hence, for the synthesized Al-Si materials where Al is deposited over silica in very small, thin domains it is possible that XPS records a higher silica surface fraction than actual.

- The PZC method translates strictly surface sensitive PZC values of Al-Si supports to surface coverage using the 2-surface model [63]. For example, deposition of Al_{13}^{7+} Keggin precursor over OX 50 silica shifted the PZC from 4.0 (silica) to 7.0 (Al-Si), which translates to about 45% alumina coverage according to the PZC method. However, this method does not account for the presence of (stronger) Brønsted acid sites at the interface between the silica and alumina and their effect on PZC. The presence of strong(er) Brønsted acid sites is expected to create a permanent (or at least extending over a broad pH range) negative surface charge. Therefore, measured PZCs of Al-Si supports with reasonably high acid site densities may translate to a significant overestimation of the coverage by the low PZC component (e.g., silica in this case).

- A third way to estimate component surface coverage is to use the anionic $PtCl_6^{2-}$ uptake data. It is reasonable to assume that anionic metal uptake over Al-Si materials at low pH would be exclusively electrostatic and exclusively onto alumina. Hence alumina surface coverage can be estimated by extrapolating anionic metal uptake over single oxides to fit with the anionic uptake over Al-Si supports (Figure 3.7I, II, III, A).

The results of these three surface coverage estimates are given in Table 3.6.

Table 3.6. Estimation of alumina surface coverage of Al-Si by different techniques.

Support	**Alumina surface coverage [area%]**		
	Via XPS	**Via PZC**	**Via $PtCl_6^{2-}$ uptake**

Al-1	-	-	100
AlSi-50	5	45	42
AlSi-380	10	16	50
SIRAL 80	28	3	11
SIRAL 70	25	3	30
SIRAL 40	57	10	62
SIRAL 20	83	35	78

As expected from the above mentioned limitations, discrepancies exist between the alumina surface coverage obtained by these three techniques. Interestingly, surface coverage values estimated by XPS were close to bulk fractions (listed in Table 3.3), as expected from the high penetration depth of XPS in light materials. The alumina surface fraction estimated based on PZC measurements are comparatively very low for the SIRAL series likely due to the presence of Brønsted sites as mentioned above. In principle, the most accurate value should be that based on $PtCl_6^{2-}$ uptake data. Although this method may not be as direct as the other techniques it is preferred for its applicability to all supports, without any serious compromise on accuracy. Selective metal adsorption is thus a novel yet simple technique to analyze surface composition of metal oxide Al-Si samples [93].

Using the surface coverage values, several important parameters can be estimated. Firstly, the contribution of non-electrostatic adsorption as a function of pH can be estimated. Using the surface area normalized $Pt(NH_3)_4^{2+}$ uptake over single oxides and alumina surface coverage (calculated based on $PtCl_6^{2-}$ uptake), electrostatic uptake over Al-Si supports could be calculated. This contribution was deducted from the total $Pt(NH_3)_4^{2+}$ uptake measured over Al-Si supports (Figure 3.7B) to quantify non-electrostatic (assumed IE) uptake. Plotted in Figure 3.11, this non-electrostatic $Pt(NH_3)_4^{2+}$ uptake showed significant pH sensitivity although it has been previously postulated that ion exchange would be pH insensitive [97]. However, that postulation was based on the study

over zeolites, i.e. materials containing strong Brønsted acid sites. In comparison, the acid sites of the Al-Si supports (amorphous silica-aluminas) are considerably weaker and hence may act differently.

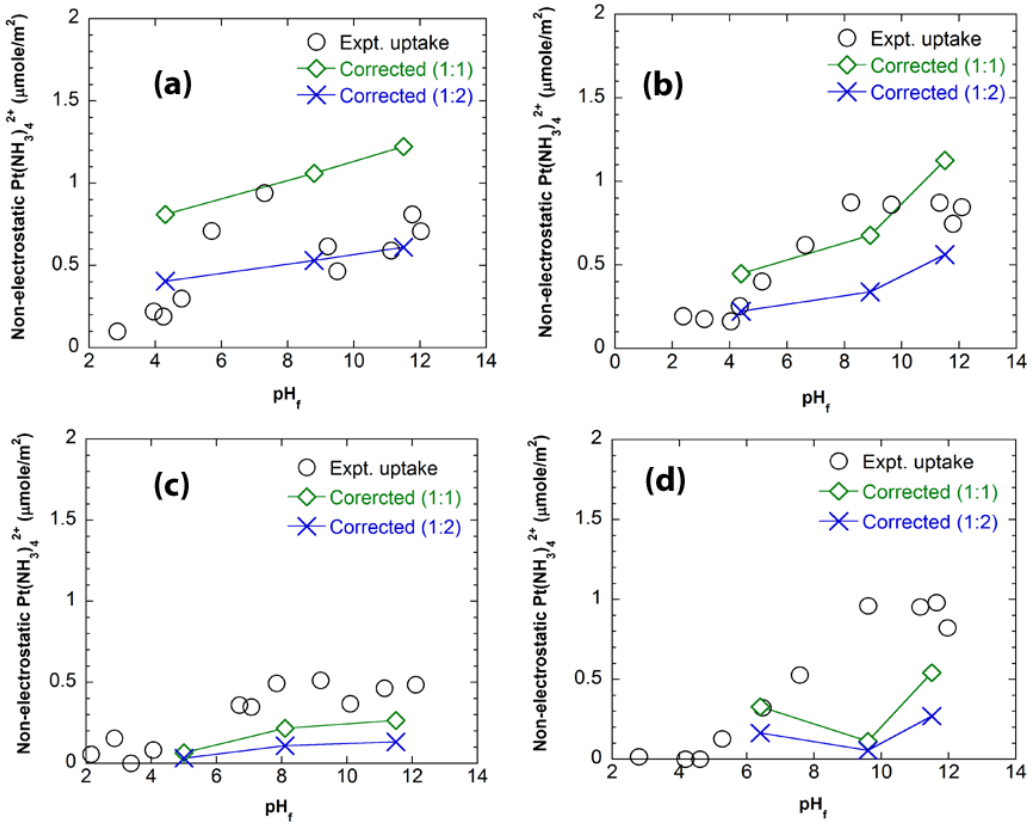

Figure 3.11. Non-electrostatic (presumably, IE) cationic $Pt(NH_3)_4^{2+}$ uptakes (open circles) over (a) SIRAL 80, (b) SIRAL 70, (c) SIRAL 40 and (d) SIRAL 20 supports. Other data points represent acid sites by NH_3-TPD measured at different pH for each Al-Si support (metal free).

Secondly, the non-electrostatic uptake can be correlated with the number of non-alumina acid sites. NH_3-TPD profiles of SIRAL samples treated at different pH showed significant changes in the number and strength of the acid sites with pH (Figure D.2 in the appendix). Such a pronounced role of the pH of Pt adsorption on the modification of aluminosilicate acidity is in agreement to a previous report [95]. The total number of acid sites measured from these NH_3-TPD experiments (open diamonds in Figure 3.11) includes

the contribution of the alumina-like domains, the value of which can be quantified knowing the surface coverage of alumina and surface area normalized acid site density of a representative alumina sample (detail procedure included in the supplementary information). This amount is then subtracted from the total number of acid sites in order to obtain a corrected number of acid sites (that would correspond to the adlineation acid sites) for each Al-Si support (metal-free) treated at different pHs. The results have been plotted in Figure 3.11 to compare with non-electrostatic uptake. In this figure the numbers of ad-lineation acid sites have been presented in equivalent $Pt(NH_3)_4^{2+}$ uptakes by considering 1 $Pt(NH_3)_4^{2+}$ per acid site (labeled as "Corrected (1:1)") and 1 $Pt(NH_3)_4^{2+}$ per 2 acid sites (labeled as "Corrected (1:2)"). Despite the simple assumptions in Figure 3.11, reasonable agreement between non-electrostatic uptake and acid sites at the ad-lineation is observed for the Si-rich Al-Si samples (SIRAL 80 and SIRAL 70). On the other hand, there is no clear correlation for the Al-rich and particularly the SIRAL 20 sample. However, as this sample contains a high fraction of alumina (80 wt% alumina surface coverage by alumina of 78%, see Table 3.3), one can expect that the evaluation of the number of ad-lineation sites on SIRAL 20 would be very approximate.

3.7.2 Pt dispersion over Al-Si

Over the Al-Si supports, a combination of high pH-cationic precursor resulted in small platinum nanoparticles (Table 2). On the contrary, for anionic $PtCl_6^{2-}$ adsorption at low pH particularly for the Si-rich Al-Si supports, Pt particles were aggregated, resulting in strong discrepancies between XRD and chemisorption sizes. The electrostatic nature of oxide components dictates that, at low pH, metal ion adsorption should occur exclusively over alumina. In agreement with this, elemental (Pt, Si and Al) mappings of the reduced

samples prepared by $PtCl_6^{2-}$ adsorption on Si-rich Al-Si supports (Figure 3.12), revealed overlapping Pt and Al domains. This strongly hints at initially selective Pt adsorption over alumina domains via electrostatic adsorption. The electrostatic nature of $PtCl_6^{2-}$ uptake surveys over the Al-Si samples displayed in Figure 3.7 also supports this assertion. Moreover, the coarser nature of alumina domains at the Pt overlapped locations, compared to the metal free AlSi-50 support in Figure 3.6c, suggests possible migration of alumina domains during reduction treatment in presence of Pt.

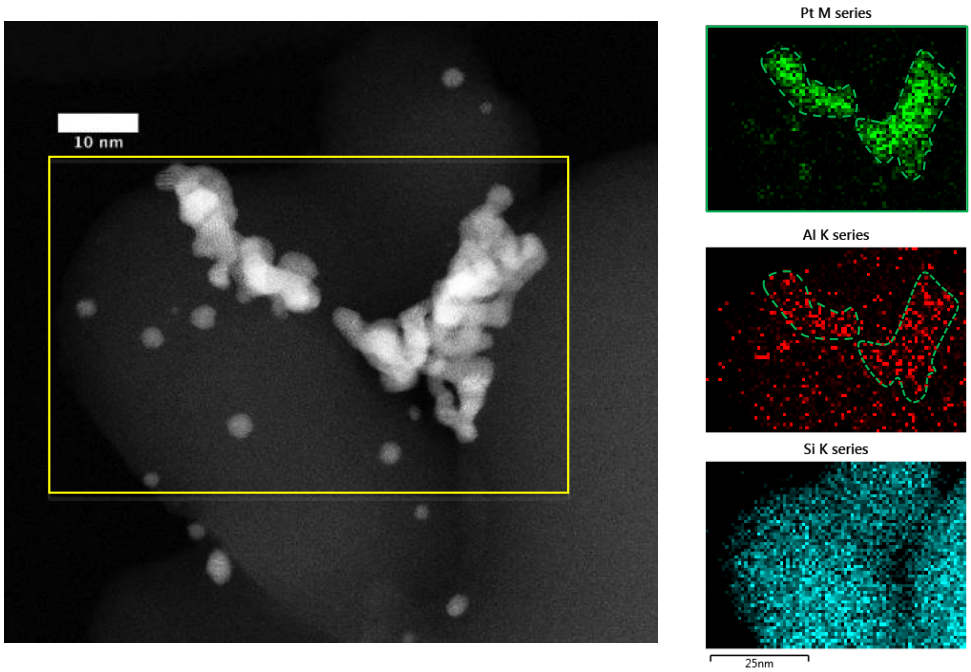

Figure 3.12. Al, Pt and Si elemental mapping of 0.7% Pt ($PtCl_6^{2-}$) over AlSi-50. As a guide to the eye, the contour of the platinum particle has been drawn from the Pt elemental mapping card and reported on the Al elemental mapping card (dashed green line).

Weak adsorption can potentially prevent $PtCl_6^{2-}$ from remaining anchored on small alumina domains during reduction. To test this, Langmuir isotherms were developed for the adsorption of $PtCl_6^{2-}$ on all Al-Si supports (Figure 3.8). The adsorption constant, K_{ads} values generated from the isotherms (Table 3.4) have been plotted in Figure 3.13 with

respect to the alumina domain sizes listed in Table 3.3. Pt dispersions measured by chemisorption are also plotted versus alumina domain size. Since most of the Al-Sis contained boehmite prior to calcination (that were converted to γ-alumina upon calcination), adsorption isotherms were also developed for representative γ-alumina support, Al-1, which was commercially synthesized from boehmite.

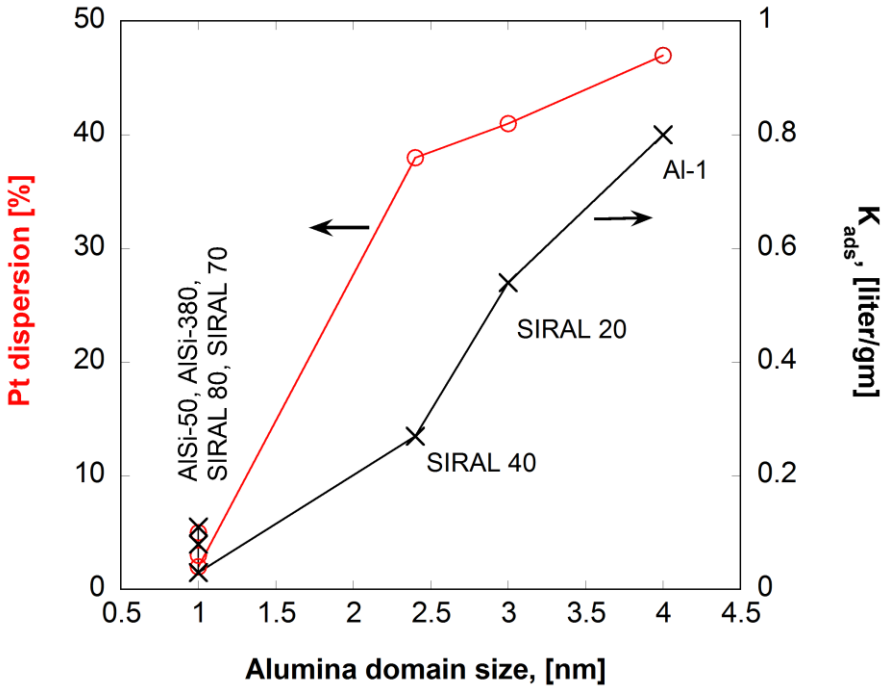

Figure 3.13. Dispersion (chemisorption) of 0.7% Pt (prepared using $PtCl_6^{2-}$) over γ-alumina (Al-1) and Al-Si supports with respect to the size of alumina domains obtained from XRD. For the Si-rich Al-Si supports, the size of the alumina domains has been arbitrarily set to 1 nm as it could not be evaluated using XRD). Adsorption constants (K_{ads}) have been added on the secondary Y-axis.

All the Si-rich Al-Si samples on which size and/or bulk content of alumina were too small to be identified from their respective XRD patterns (Figure 3.5a) showed low $PtCl_6^{2-}$ adsorption constants as well as low Pt dispersion. On the other hand, Al-Si samples with alumina domains discernible from their respective XRD patterns (e.g., SIRAL 20, SIRAL 40) showed reasonably high adsorption constants and Pt dispersion. Average sizes

of alumina domains on these two Al-rich Al-Si supports were calculated using Scherrer equation on 2 distinct γ-alumina peaks indexed as (400) and (440) and were found to be 2.4nm and 3.0nm for SIRAL 40 and SIRAL 20 respectively. For the pure alumina support (Al-1), size of alumina domains were found to be moderately larger (4.0 nm). Overall, these results suggest that a critical size of alumina domain is necessary for strong $PtCl_6^{2-}$ adsorption and therefore better dispersion after high temperature reduction.

Catalyst synthesized via dry impregnation (DI) of $Pt(NH_3)_4Cl_2$ over AlSi-380 and SIRAL 80 also carry strong evidence of the IE. Due to high buffering by oxide supports, the DI method normally results in a pH close to the PZC where there usually exists little or no metal-support interaction [20]. The resulting metal particle size from DI method is usually relatively large. However, the fact that Pt particle size was actually relatively small over the AlSi-380 and SIRAL 80 supports (Table 3.5 and Figure 3.9c) suggests that IE, which can occur close to the PZC of the mixed oxide, (as already shown for the series (a) samples), contributed to the metal-support interaction and thereby reduced particle size. In contrast to this trend, the DI method yielded larger Pt particle size on AlSi-50 support (Table 3.4 and Figure 3.9c), but it is likely due to a too limited number of ion exchange sites on this weakly acidic support. It is important to mention here that the PZCs of these Al-Si samples are slightly higher than the PZC of silica and significantly lower than that of alumina. This means that at the PZC of the Al-Si samples, the surface fraction of alumina would be positively charged and would not favor electrostatic $Pt(NH_3)_4^{2+}$ adsorption. On the other hand, the silica fraction will be positively charged at the Al-Si PZC. However, at this pH the potential would to be too low (Figure 3.1) to favor electrostatic adsorption.

3.8 Conclusion

In this study the potential to control Pt deposition over silica-alumina mixed oxides was explored by exploiting the difference in charging behavior between two component oxides (silica and alumina) in solution and the acid sites generated at the interface between them. Based on the results, following conclusions could be drawn:

[1] Over physical mixtures, selective Pt adsorption was demonstrated using the appropriate pH-precursor complex combination: low pH (at or near the point of zero charge of silica) and anionic precursor complex enabled Pt deposition preferentially on the alumina phase whereas an intermediate pH (at or near the point of zero charge of alumina) and a cationic precursor resulted in selective Pt deposition on the silica phase.

[2] From the adsorption study over composite Al-Si supports alumina surface coverage (anionic Pt adsorption) and the number of acid sites (cationic Pt adsorption) could be estimated.

[3] Well-dispersed Pt/Al-Si catalysts could be prepared using pH adjusted cationic Pt precursor. Even when the same precursor was deposited on acidic Al-Si via DI method, Pt dispersion was reasonably good particularly for the more acidic Al-Sis. This was suggested to be influenced by ion exchange mechanism.

[4] For anionic Pt ($PtCl_6^{2-}$) adsorbed catalysts, it was observed that small Pt particles aggregated significantly over silica rich Al-Sis with small alumina domain sites. There appears to be a critical alumina domain size of about 2.4nm to anchor anionic precursors on the alumina.

3.9 Future work

Migration of alumina domains on Al-Si under reduction condition in presence of metal could be further investigated. Also, role of pH on the evolution of acid sites on the aluminosilicates could be systematically studied using various characterization tools e.g., Lutidine IR, ^{27}Al NMR. Analysis in a metal-acid bifunctional reaction will reveal how different preparation condition could affect catalytic performance. This will be discussed in the next chapter. Overall, the method outlined here could be applied to many other composite oxides with high academic and industrial research interest.

Chapter 4

Effect of the balance and proximity between active sites in selectively deposited Pt over silica-alumina catalysts

4.1 Introduction

Metal-acid bifunctional catalysts have become part and parcel of many industrially significant chemical processes for energy, environment and consumer based applications. Already established processes include, but are not limited to, selective ring opening (increase of cetane number), hydroisomerization (increase of octane number), hydrocracking of heavy oils, reforming and dewaxing [76, 93, 107-110]. More recently, studies on the utility of bifunctional catalysts on biomass conversion have been on the rise [74, 111-113]. Metal-acid bifunctional catalysts have also opened interesting avenues to one step synthesis of fine chemicals and liquid fuels from syn gas and biomass [74, 114, 115].

According to the classical mechanism of bifunctionality, proposed over 50 years ago, a close proximity between metal and acid sites was prescribed to facilitate the diffusion of reaction intermediates between the two types of sites [116]. According to this mechanism, metal (e.g., Pt) provides active sites for hydrogenation/dehydrogenation whereas isomerization/cracking takes place on the acid sites [116]. The role of each type of active sites in a bifunctional reaction has been extensively studied and the overall scheme of this reaction appears frequently in literature. Nevertheless, the degree of intimacy required between the two types of active sites for bifunctional applications has

rarely been tested due to a lack of control of this parameter during synthesis of these catalysts [83-85, 117, 118]. Most often the closest proximity between active sites has been employed using ion exchange where metal cations exchange a fraction of the acid sites of the support.

In the previous chapter, Pt deposition over silica-alumina mixed oxides (Al-Si) was controlled to achieve selective adsorption of metal precursor ions over silica or alumina domains using cationic $Pt(NH_3)_4^{2+}$ (PTA) and anionic $PtCl_6^{2-}$ (CPA) precursors respectively at appropriate pH. Due to a stronger anchoring of the PTA precursor on silica compared to the CPA precursor on alumina, two different degrees of proximity between Pt and acid sites were obtained. Pt and acid sites were in the closest proximity with highly dispersed Pt nanoparticles for samples prepared by electrostatic adsorption of $Pt(NH_3)_4^{2+}$ at high pH (atomic-scale proximity). These catalysts will be identified as "PTA-11" with 11 representing the adsorption pH. One additional set of catalysts was prepared via dry impregnation (DI) of $Pt(NH_3)_4Cl_2$ over Al-Si supports without pH control. The resulting catalysts showed evidence of ion exchange [119]. These catalysts will be referred to as "PTA-DI" and presumed, based on their small particle size, to have the same level of intimacy as PTA-11. On the other hand deposition of $PtCl_6^{2-}$ onto small alumina domains in Si-rich Al-Si led to agglomerated Pt nanoparticles after reduction. The large Pt agglomerates (~15nm) led to a catalyst series with "nanometer scale" proximity with the acid sites. This series of catalysts will be referred to as "CPA-4" with 4 representing the adsorption pH. In order to stretch the degree of proximity even further, physical mixtures of a component with only metallic function, Pt/silica and a component with only acid function e.g., amorphous aluminosilicate, were studied. For physical mixtures (referred to

as “PM”), the degree of intimacy was broadly defined to be in the micrometer-scale range. In other series of catalysts, the metallic and acidic components were maintained even further apart by adding inert layers composed of quartz wool in between them (millimeter-scale intimacy). These layered catalysts were labeled as “L-#”. Schematics of these catalysts, categorized in terms of degree of intimacy have been illustrated in Figure 4.1.

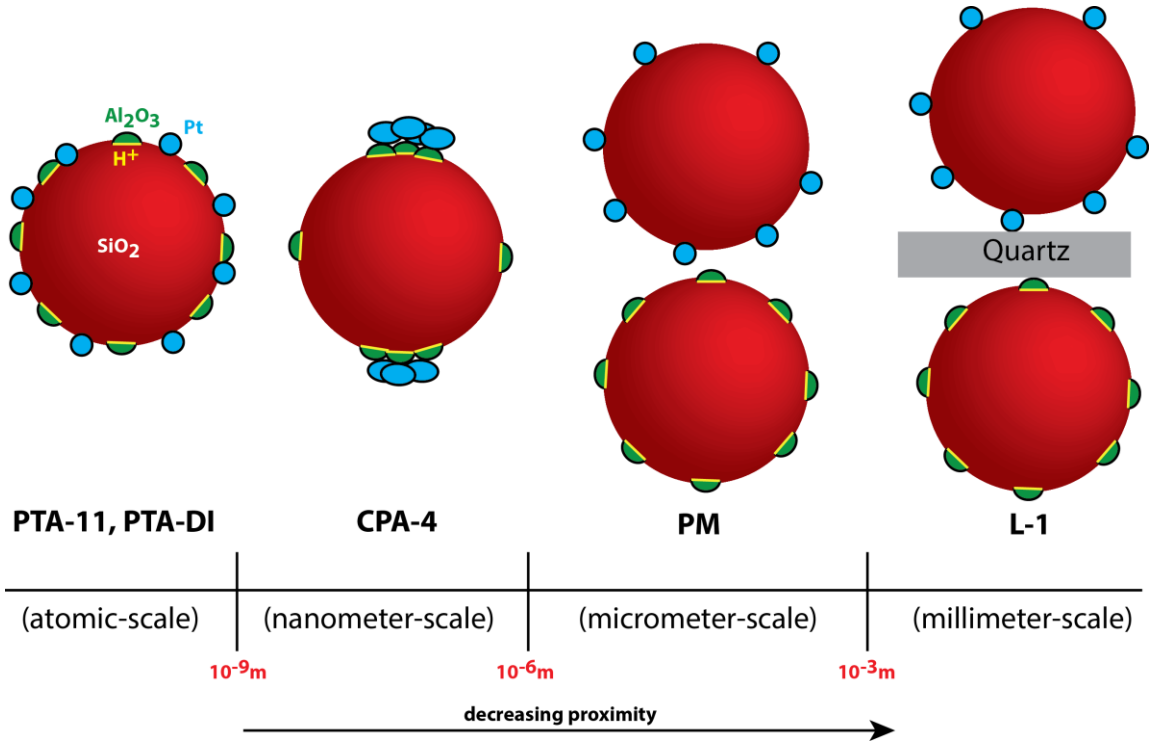

Figure 4.1. Schematics of catalysts used in this study showing different degree of intimacy between active sites. Images are not drawn to scale.

All these samples constitute an array of catalysts with variations in total number of acid sites, active metal surface and proximity between metal and acid sites. These catalysts were tested in an n-heptane isomerization reaction. Following objectives were set for this study:

1. Evaluation of catalytic performance in a metal-acid bifunctional reaction.

2. Study of catalyst activity and selectivity in light of the synergy between metal and acid sites.
3. Study of catalyst stability and deactivation.

For objective 1, catalytic performance of all the catalysts was investigated in an n-heptane isomerization reaction operated at 350°C and atmospheric pressure. Based on the characterization results of these catalysts, the ratio of acid to metal sites, n_a/n_{Pt}. Catalyst performance was correlated with respect to this ratio and proximity between active sites (shown in Figure 4.1) for objective 2. For objective 3, catalyst deactivation was investigated by characterizing the catalysts before and after reaction. Experimental schemes of this study have been presented in Table 4.1.

Table 4.1. Experimental schemes of this study.

Objective(s)	**Experiment(s)**	**Expected outcome(s)**
1	Reaction run with Pt and silica-alumina based catalysts	Evaluation of activity, selectivity and deactivation
2	(a) NH_3-TPD and (b) H_2 Pulse chemisorption on Pt/Al-Si catalysts	Calculation of ratio of acid-to-metal sites, n_a/n_{Pt}
3	STEM imaging on fresh and spent catalysts	Understanding cause of deactivation

The main contributions of this research are:

(1) Study of bifunctionality of Pt/silica-alumina catalysts in light of the ratio and proximity between metal and acid sites.

4.2 Bifunctional reaction mechanism

According to the classical interpretation of bifunctional mechanism, metal (e.g., Pt) promotes hydrogenation/dehydrogenation whereas isomerization/cracking takes place on acidic support [116]. This mechanism has been illustrated in Figure 4.2.

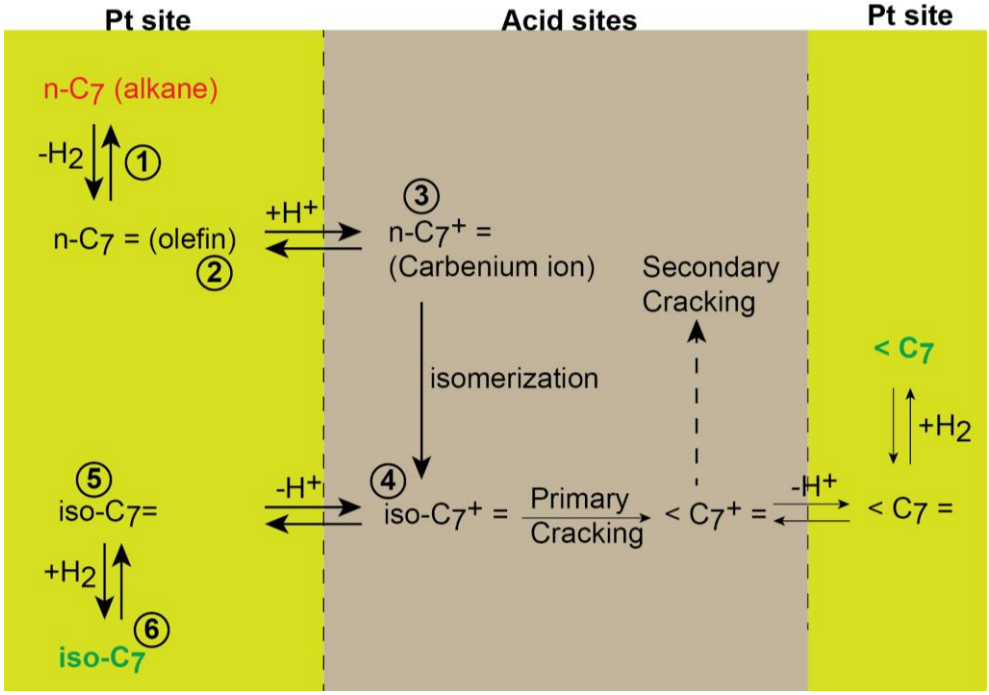

Figure 4.2. Simplified classical mechanism for isomerization of n-alkane on a metal-acid bifunctional catalyst.

Overall, according to this mechanism, n-alkane transformation proceeds through following six steps:

1) Dehydrogenation of n-alkanes at the metal sites to form olefins.

2) Desorption of olefins from the metal sites and diffusion to the Brønsted acid sites.

3) Formation of active intermediates in the form of carbenium ions.

4) Skeletal rearrangement (isomerization) and/or β-scission (cracking).

5) Desorption from the acid sites and diffusion to the metal sites.

6) Hydrogenation at the metal sites.

In order to facilitate gas phase diffusion between metal and acid sites, a close proximity between metal and acid sites has been prescribed in the classical bifunctional mechanism. However, the gas phase diffusion of intermediates between active sites depicted in this mechanism has been under considerable scrutiny lately. For cases where classical interpretation deemed inadequate, new hypotheses have been proposed (e.g., hydrogen spillover) [120-122]. In hydrogen spillover mechanism, hydrogen splits over from metal to acid sites and assist in the generation of carbenium ions and subsequent products form from n-alkanes [123]. This model obviates the formation of alkene intermediates. Additionally, in contrast with the classical mechanism, here the function of metal sites is only to supply hydrogen to the acid sites i.e., no reaction takes place on the metal site. Nevertheless, justification of this mechanism has been reviewed in several reports and is still under considerable debate [124, 125].

4.3 Factors influencing bifunctionality: ideal bifunctional catalyst

Weitkamp in his review paper discussed the features and importance of an "ideal" hydroconversion catalyst [126]. Constructed on a strong hydrogenating/dehydrogenating function, an "ideal" bifunctional catalyst offers flexibility in hydrocarbon conversion. As acid sites promote cracking reaction on a strongly acidic, monofunctional catalyst, distribution of products is mostly obtained in the low carbon number range which reduces the overall quality of the fuel. Introduction of a strong dehydrogenation/hydrogenation function in the form of metallic sites can promote rapid desorption of products from the acid sites and thereby prevent unwanted cracking. As a consequence, for an ideal

bifunctional catalyst, reaction step at the acid sites should be the rate limiting step [85, 126].

Guisnet in his review described "ideal" bifunctional catalyst in light of the balance between active sites [127]. Summarizing experimental findings he concluded that for optimal bifunctional performance the ratio between metal and acid sites should be high enough in order for the acid catalyzed reaction to be rate limiting [118]. It was also suggested that the number of zeolite acid sites between two metal sites should be small enough to limit skeletal transformation of alkene intermediates. Pronounced effect of metal and acid site balance has also been recorded in other studies using different bifunctional reactions [128-130]. In many of these studies, zeolites with strong and abundant acid sites were used. However, if moderately acidic aluminosilicates are used the overall impact of active site balance could be very different. Musselwhite et al. used platinum over bifunctional mesoporous aluminosilicate catalysts in n-hexane isomerization reaction [131]. Based on the results, they concluded that balance between sites have pronounced effect on the bifunctionality of catalyst. They argued that if Pt loading is too high the catalyst could act monofunctionally whereas if it is too low the overall turnover rate would be too low.

Effect of proximity between active sites on catalyst bifunctionality has rarely been studied due to lack of control during the synthesis of bifunctional catalysts. Particularly, controlling the location of Pt within nanoscale precision has not often been possible [93]. Inspired by the intimacy criterion prescribed through classical bifunctional mechanism, ion exchange method has frequently been used to deposit metal at the closest proximity of the acid sites. Zečević et al. conducted a systematic study where controlled proximity between

active sites was achieved [93]. They found that Pt nanoparticles located inside zeolite micropores and thereby maintaining closest intimacy with acid sites did not deliver the most optimized performance with respect to high quality diesel production. This is counterintuitive with respect to the classical interpretation of bifunctionality. It was argued that olefinic intermediates formed on the metal sites experienced slow diffusion through zeolite micropores. This could potentially enhance the possibility for secondary undesired reactions (e.g., cracking) and diminish the quality of the fuel. Similar effect of pore size on the performance of bifunctional catalysts was reported in other studies [126, 132, 133] which prompted researchers to use materials with designed porosity, geometry and composition [77, 134, 135]. Several other studies reported enhanced bifunctionality with physically mixed metallic and acidic components. Some of these results could also be interpreted in light of the effect of pore size [134]. Kim et al. controlled the zeolite crystal thickness and varied the distance between metal and acid sites [136]. They concluded that up to 300nm distance the selectivity of these bifunctional catalysts remain unaffected.

4.4 Materials and methods

The synthesis protocols and characteristics of the catalysts for this study have been reported in Chapter 3. In brief, three different silica-alumina (Al-Si) mixed oxides were used as support. Two were synthesized in-house (AlSi-50, AlSi-380) for which highly dispersed alumina domains were formed on parent nonporous silica particles. A commercial amorphous SIRAL 80 (Sasol, Germany GmbH) was used as the third support. The number in the SIRAL support id represents the weight % of silica in that support (SIRAL 80 contains 80% silica). The total number of acid sites on these supports was from low to high: AlSi-50<AlSi-380<SIRAL 80. These supports could be categorized as Si-rich

Al-Si. Several catalysts were also prepared using more Al-rich SIRAL supports e.g., SIRAL 20, SIRAL 40 and SIRAL 70. One nonporous, non-acidic silica (Aerosil®OX50, Evonik-Degussa, 54m^2/g), named Si-50, which was used to synthesize AlSi-50, as well as a metal-only monofunctional Pt/Si-50 catalyst. Characterization included XRD to identify different phases and determine domain size of alumina, ^{27}Al NMR for confirmation of Al deposition onto parent silica and NH_3-TPD to quantify acid sites [33]. Catalysts with two target weight loadings of 0.4wt% and 0.7wt% Pt were prepared. As seen in Table 4.2, actual weight loadings varied slightly.

Table 4.2. Characteristics of Pt/Al-Si catalysts and results of n-C_7 conversion.

Catalyst	**D[a] [%]**	**Total acid [µmoles/g]**	**n_a/n_{Pt}**	**conv. [mol%][b]**		**Multi/ Mono[c]**
				initial	**final**	
Monofunctional catalyst						
0.69% PTA-11	48	0	0	41.2	24.0	0.47
SIRAL 80 (No Pt)	-	290	∞	0	0	0
Support: AlSi-50						
0.75% PTA-11	54	<30	-	41.2	29.0	0.22
0.46% PTA-11	61	<30	-	29.8	16.3	0.21
0.70% PTA-DI	11	<30	-	4.5	2.2	-
0.73% CPA-4	4	<30	-	18.0	8.7	0.31
Support: AlSi-380						
0.76% PTA-11	45	199	11	35.7	29.8	0.08
0.42% PTA-11	31	231	35	26.1	24.2	0.09
0.70% PTA-DI	59	37.6	2	50.7	31.7	0.12
0.40% PTA-DI	65	122	9	44.0	31.2	0.13
0.72% CPA-4	3	143	124	10.2	14.6	0.15
0.39% CPA-4	3	137	238	7.3	17.9	0.13
Support: SIRAL 80						
0.66% PTA-11	62	290	14	34.4	22.9	0.15
0.32% PTA-11	100	327	20	25.6	15.7	0.13
0.70% PTA-DI	33	344	29	48.1	36.7	0.11
0.40% PTA-DI	41	472	56	26.2	25.8	0.09
0.72% CPA-4	6	360	163	23.4	20.5	0.11
0.39% CPA-4	1	307	1536	42.5	11.1	0.21
Support: SIRAL 70						
0.60% CPA-4	3	344	372	44.9	37.2	0.11

Support: SIRAL 40						
0.65% PTA-11	42	420	30	44.0	34.3	0.03
0.60% CPA-4	39	390	33	74.3	55.4	0.11
Support: SIRAL 20						
0.71% PTA-11	37	430	32	40.2	32.6	0.08
0.72% CPA-4	40	385	26	67.6	42.5	0.21

[a]Dispersion by pulse chemisorption, [b]Conversion at WHSV=1.0h^{-1}, T=350°C, P=1atm, [c]Mu/Mo at 22 ± 3% conversion, TOS=18h

4.4.1 Catalytic reaction

Transformation of n-heptane (n-C_7) was conducted in a U-shaped flow-type, fixed-bed, quartz tube reactor and operated at 350°C and atmospheric pressure. 0.2g of catalyst powder was supported by quartz wool. Prior to reaction, the catalyst was reduced in situ in flow of hydrogen (25ml/min) at 350°C for 6h. The reactants (n-C_7 and H_2) were introduced by flowing H_2 carrier gas through a conventional saturator (maintained at 12°C) containing n-C_7. This resulted in an H_2/n-C_7 mole ratio of 33:1. The weight hourly space velocity (WHSV) was 1.0h^{-1}. "Initial" (time-on-stream, TOS=0.33h) and "final" (TOS=18h) activity and the extent of deactivation were measured at this WHSV. After 18h time-on-stream, the space velocity was adjusted by changing H_2 flow rate in order to reach 22% ± 3% conversion. Product selectivity was measured at this constant conversion. Mass flow rates were regulated using Brooks controllers. Effluent gas compositions were analyzed by online gas chromatography with a flame ionization detector (FID) and a capillary column (CP-Sil PONA CB, 50 x 0.21mm, Varian).

The reaction products were divided into four categories: (a) Aromatic (Toluene), (b) C_7 isomers (i-C_7), (c) cyclic products (Cyclic) and (d) cracking products (<C_7). Toluene was the sole aromatic compound detected. i-C_7 products were composed of monobranched e.g., methylhexane, ethylpentane and multibranched isomers e.g., dimethylpentanes. Cyclic products were composed of substituted C_5 cyclic compounds with seven carbons,

e.g., dimethylcyclopentanes, ethylcyclopentane with a small fraction of methylcyclohexane and methylcyclopentane. Finally, n-C_6 to n-C_2 single chain alkanes and a few other <C_7 isomers e.g., dimethylpentane, isobutane, dimethylpropane were representatives of <C_7 products. Equations used to calculate selectivity and turnover frequency (TOF) are as follows.

$$\text{Selectivity of product i} = \frac{\text{moles of product i}}{\sum \text{moles of product with 4 or more carbon numbers}}$$

TOF of i-C_7=

$$\frac{\text{Fractional n-}C_7\text{ convertion} \times \text{Fractional selectivity of i-}C_7 \times \text{WHSV} \left[\frac{\text{gm n-}C_7}{\text{gm cat. sec}}\right] \times MW_{Pt}}{\frac{\text{gm Pt}}{\text{gm catalyst}} \times MW_{\text{n-}C_7} \times \text{Fractional Pt dispersion}}$$

4.5 Results

4.5.1 Acidity of Pt/Al-Si catalysts

Acidity of each one of the Al-Si supports and the effect of pH on their acidity have been discussed at length in Chapter 3. NH_3-TPD profiles of Pt loaded Al-Si catalysts, characterized using NH_3-TPD have been included in Figure 4.3.

The total number of acid sites of Pt/Al-Si catalysts is listed in Table 4.2 and plotted in Figure 4.4. Catalysts prepared from $Pt(NH_3)_4^{2+}$ with higher Pt loading (0.7wt%), consistently exhibited less acid sites than the lower loading (0.4wt%). This reduction in acid sites was more drastic for the PTA-DI set where, as explained in the companion paper [119], ion-exchange would be the sole deposition mechanism. For CPA-4 samples prepared by anionic $PtCl_6^{2-}$ adsorption, acidity remained virtually unchanged with metal loading as expected in the absence of ion exchange. The low acid site density (< 30μmoles/g) of AlSi-50 support could not be measured reliably and hence is not reported.

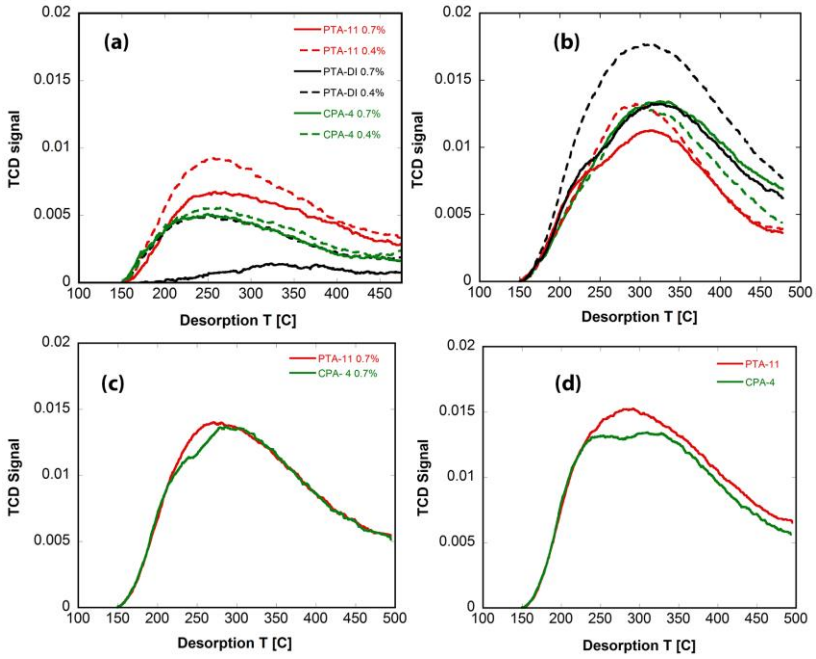

Figure 4.3. NH_3-TPD profiles of all Pt/Al-Si catalysts synthesized on (a) AlSi-380, (b) SIRAL 80, (c) SIRAL 40 and (d) SIRAL 20 support.

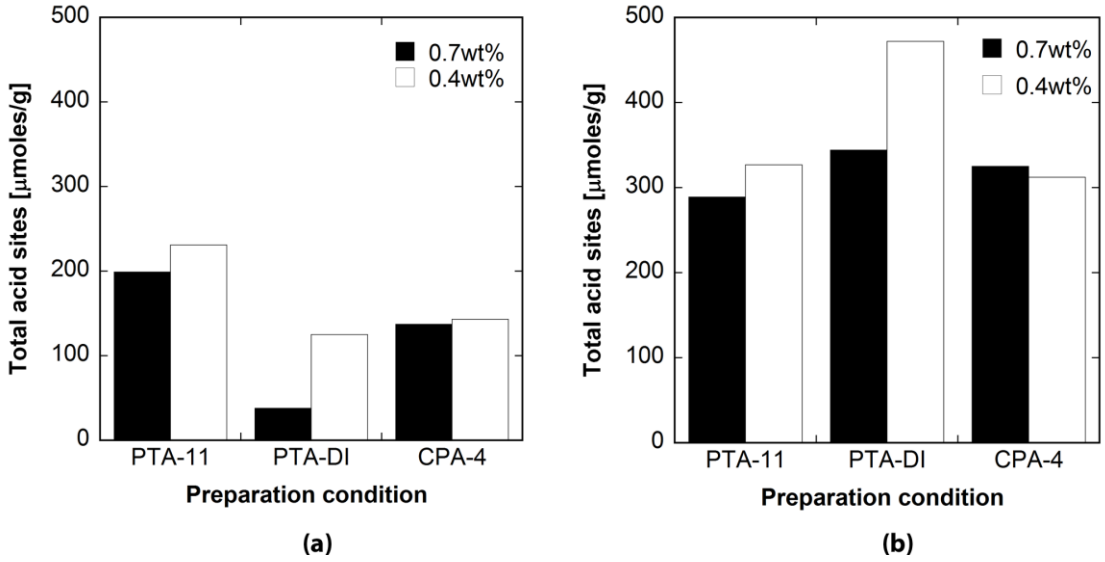

Figure 4.4. Total number of acid sites (NH_3-TPD) of 0.4wt% and 0.7wt% Pt/Al-Si catalysts synthesized at different conditions (precursor, pH): (a) Synthesized from AlSi-380 and (b) from Commercial SIRAL 80.

4.5.2 Performance of Pt/Al-Si catalysts

The physicochemical characteristics of the Pt/Al-Si catalysts prepared using different conditions (precursor, pH) are listed in Table 4.2. The metal dispersion (D,%) and total number of acid sites were used to calculate the ratio of acid to active metal sites, n_a/n_{Pt}. The results of n-C_7 reactivity, specifically, initial and final conversion and the ratio of multi-to-monobranched i-C_7 products (multi/mono) are included. The product distributions at 22%±3% conversion after TOS=18h have been plotted in Figure 4.5. The performance of a monofunctional 0.69wt% Pt/Si-50 catalyst, "PTA-11(Si)", has been included in Table 4.2 and Figure 4.5a for comparison. This monofunctional catalyst showed notable activity and selectivity towards i-C_7. Also, the multi/mono ratio was found to be reasonably high (0.47) and the catalyst deactivated appreciably (Table 4.2).

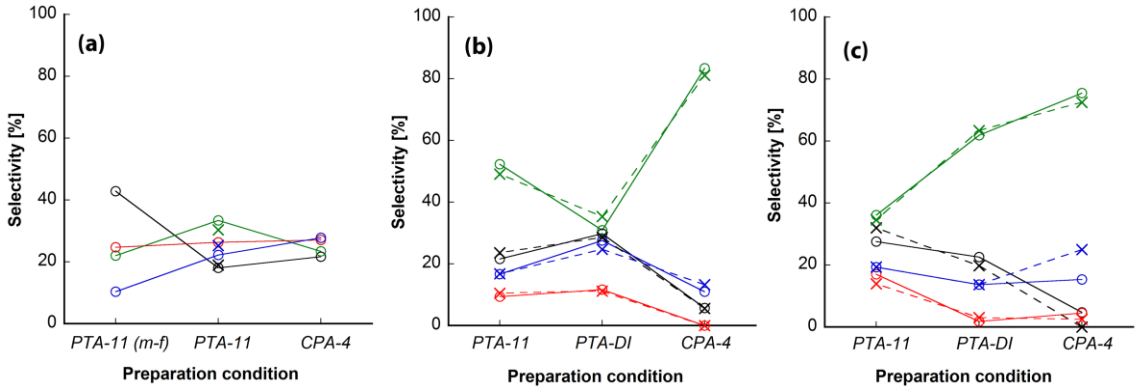

Figure 4.5. Product distribution (at 22 ± 3% conversion) of silica and Si-rich Al-Si catalysts using (a) Si-50, AlSi-50, (b) AlSi-380 and (c) SIRAL 80 as support. Product color coding: i-C_7 (Green), toluene (Black), cyclic (Red) and <C_7 (Blue). "o" with solid lines representing 0.7wt% and "x" with dashed lines representing 0.4wt% catalyst.

In the AlSi-50 support (Figure 4.5a), acid sites were introduced by Al deposition onto Si-50 silica. Bifunctionality becomes apparent in comparing the catalytic performance of PTA-11 on AlSi-50 to PTA-11 on pure silica, as i-C_7 selectivity improved primarily at the expense of toluene selectivity. However, in other aspects (e.g., deactivation,

multi/mono) this weakly acidic catalyst was quite comparable to the monofunctional Pt/Si-50 catalyst (Table 4.2). A relatively low number of acid sites limited ion exchange of cationic Pt in the PTA-DI catalyst synthesized on the AlSi-50 support. As a result, Pt dispersion on the AlSi-50 support in the PTA-DI series was poor (11%) unlike other more acidic Al-Si (e.g., SIRAL 80 or AlSi-380) supported DI catalysts. A similarly prepared (PTA-DI) 0.7wt% catalyst on Si-50 silica (no acidity) support yielded even poorer dispersion (3%) which further confirms the role of ion exchange on metal dispersion of the final catalyst. Due to their low dispersion and acidity, these catalysts (PTA-DI over Si-50 and AlSi-50 supports) were largely inactive and not included on Figure 4.5a.

Performances of Pt catalysts supported over more acidic, Si-rich Al-Si (AlSi-380 and SIRAL 80) have been presented in Figure 4.5b and 4.5c. Of these, catalysts prepared by adsorption of anionic $PtCl_6^{2-}$ (CPA-4, nanometer scale proximity) stand out with significantly higher selectivity towards i-C_7. Similar performance was observed for another 0.6wt% CPA-4 catalyst using SIRAL 70 as support (Table 4.2). The PTA-11 catalysts with well-dispersed Pt (atomic scale proximity) showed less preference for i-C_7 products than the CPA-4 catalysts. On the other hand, considerable differences could be observed between product selectivity of PTA-DI catalysts prepared over AlSi-380 and SIRAL 80 supports (Figure 4.5b and 4.5c). These results will be discussed later. With few exceptions, Pt over these more acidic supports exhibited less deactivation and lower multi/mono ratios than Pt/Si-50 and Pt/AlSi-50 catalysts (Table 4.2).

Catalytic performances of other Al-rich Al-Si supports (SIRAL 20, SIRAL 40) 0.7wt% Pt catalysts synthesized at different conditions (PTA-11 and CPA-4) have also been studied. In contrast with the Si-rich Al-Si supports, anionic $PtCl_6^{2-}$ adsorption (CPA-

4) over these Al-rich supports yielded significantly higher dispersion of Pt (Table 4.2). From the selectivity results plotted in Figure 4.6 the CPA-4 catalysts over these Al-rich Al-Si showed significantly higher selectivity towards cracking (<C_7) than the PTA-11 series.

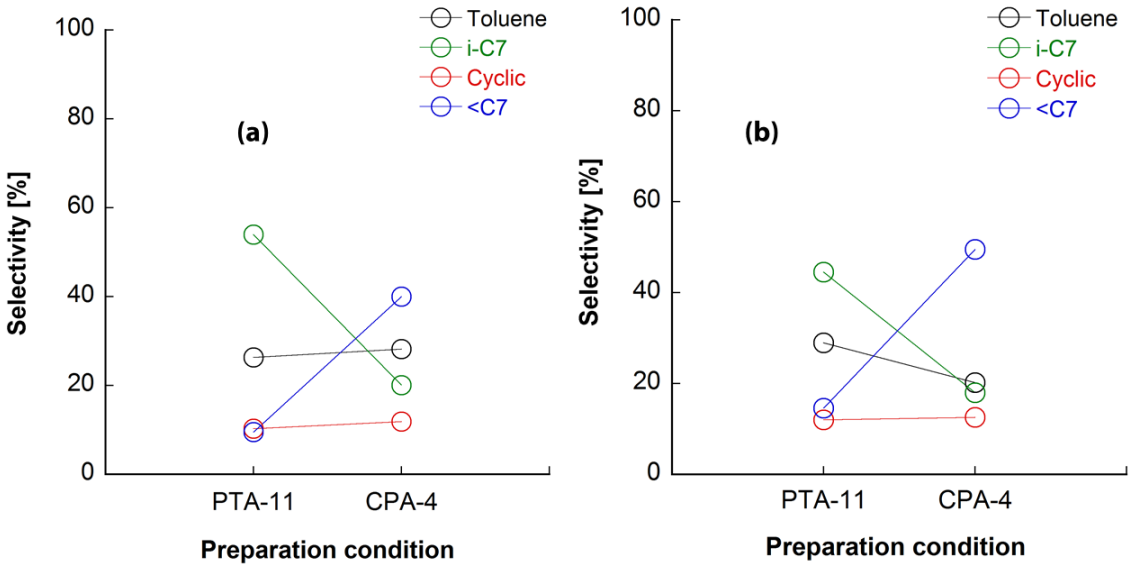

Figure 4.6. Product distribution for n-C_7 conversion (at 22 ± 3% conversion) of Al-rich (a) SIRAL 40 and (b) SIRAL 20 supported 0.7wt% catalysts synthesized at different conditions.

4.5.3 Performance of physical mixtures and layered catalysts

Performance of PM (physical mixture) and layered catalysts (L-1 to L-3) is given in Figure 4.7. Schematics of these catalysts are presented above their respective results. The two monofunctional catalysts, metal-only Pt/Si-50 and acid-only SIRAL 80, were used as references in Figure 4.7.

Two different catalyst forms were used to control the proximity between active sites. In the layered setup, the active sites were the furthest apart (millimeter scale intimacy) whereas in the physical mixtures (PM) the scale of mixing was in the micrometer range. Equal mass (~0.2g) of each component was used (1:1 mass ratio). The exact mass along with the reactivity results have been summarized in Table 4.3 and Figure 4.7. In the layered

setup, the components were ordered in different combinations to form L-1, L-2 and L-3 (Figure 4.7). According to Figure 4.7a, activity of the layered catalysts slightly improved from the monofunctional Pt/Si-50 although the distribution of products remained fairly identical (Figure 4.7b). Comparing among L-1 to L-3, no significant difference in activity or selectivity was observed (Table 4.3 and Figure 4.7) regardless of the order of components. All the layered catalysts displayed a similar degree of deactivation, apparent in Figure 5a, with a high multi/mono (Table 4.3) similar to that of the monofunctional Pt/Si-50 catalyst.

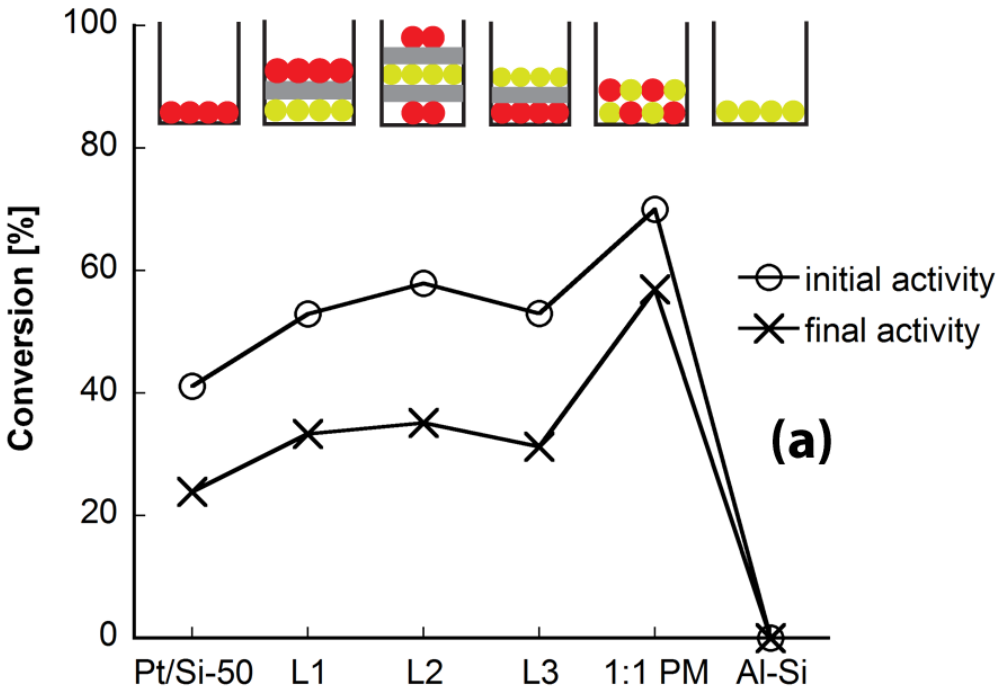

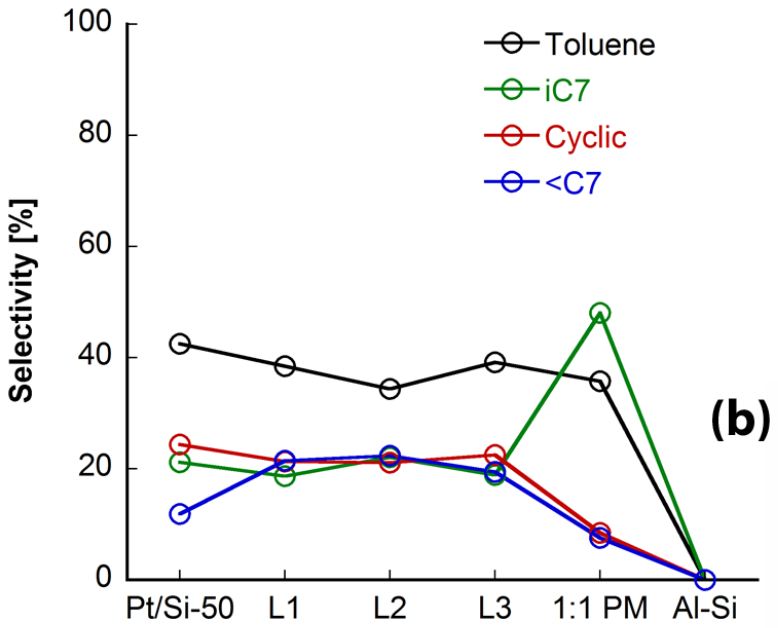

Figure 4.7. Product distributions obtained for different two-component catalysts based on Pt/Si-50 and SIRAL 80 (Al-Si). Schematic diagram on top of each sample data is showing components and their degree of intimacy. Yellow circles in the schematics represent acidic SIRAL 80 (Al-Si) and red circles represent Pt/Si-50. Total catalyst mass for 1:1 PM and layered catalysts were 0.4g with equal mass (~0.2g) of components. For reference catalysts, total mass of catalyst was ~0.2g (Exact masses are listed in Table 2).

Table 4.3. n-C_7 transformation data on PM and L-1 to L-3 catalysts.

Type	**Component Mass [g]**		**n-C_7conv. [mol%]**		**Multi/Mono**
	Pt/Si-50	**SIRAL 80**	**initial**	**final**	
Layered					
L-1	0.223	0.222	52.9	33.3	0.35
L-2	0.200	0.200	58.0	35.2	0.40
L-3	0.212	0.208	53.0	31.3	0.41
PM					
1:2	0.154	0.080	54.5	38.3	0.13
1:1	0.100	0.100	53.9	41.2	0.06
1:1[a]	0.209	0.203	70.0	56.9	0.11
2:1	0.080	0.150	52.9	44.6	0.10
6:1	0.034	0.174	47.9	39.8	0.12
10:1	0.018	0.181	37.1	32.2	0.18
15:1	0.013	0.188	30.7	27.9	0.21

[a]used as 1:1 PM catalyst in Figure 4.7

The catalytic performance of the PM catalyst in Figure 4.7a (1:1 PM) was significantly different than that of the layered catalysts. With more intimately mixed metal and acid sites, an improvement in i-C_7 selectivity at the expense of cracking ($<C_7$) and cyclic products was evident. Initial activity was also significantly higher (70% versus 58% in L-2 shown in Table 4.3 and 41% in Pt/Si-50 shown in Table 4.2) with significantly less deactivation and lower multi/mono ratio. In short, the performance of PM catalyst was more in line with the bifunctional Pt/Al-Si catalysts whereas the layered catalysts resembled the monofunctional Pt/Si-50 catalyst.

The bifunctional nature of the PM catalysts was further assessed using different mass ratios of components. The summary of the results has been reported in Table 4.3 and Figure 4.8. A constant total mass of 0.2g was used and amounts of individual components were varied. There are obvious trends of activity (Figure 4.8a) and product selectivity (Figure 4.8b) with respect to component ratio. From left to right of Figure 4.8a, catalysts with a higher acid fraction experienced less deactivation. In terms of product distribution plotted in Figure 4.8b, i-C_7 selectivity increased until a 10:1 acid-to-metal ratio. Toluene selectivity remained unchanged up to 1:1, then decreased. Selectivity to $<C_7$ decreased initially up to 1:1 ratio then increased. Finally, selectivity to cyclic products decreased with increasing ratio. High multi/mono ratio was evident at high ratios of either metallic (0.13 for 1:2 ratio) or acidic component (0.18 for 10:1, 0.21 for 15:1 ratio) seen in Table 4.3. At intermediate ratios (1:1–6:1), however, multi/mono ratios were significantly lower.

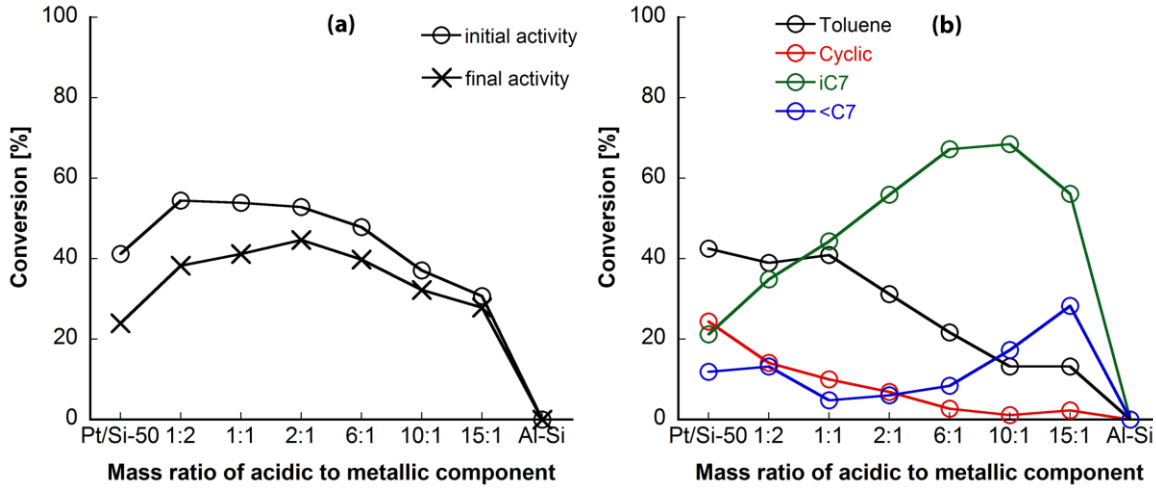

Figure 4.8. (a) Conversion and (b) product selectivity of PM catalysts with different mass ratios of Pt/Si-50 and SIRAL 80 (Al-Si) components. Total mass of catalysts = 0.2g and selectivity data obtained for 22±3% conversion.

4.5.4 Stability of catalysts

From the activity data summarized in Table 4.2, it is evident that some Pt/Al-Si catalysts have undergone deactivation over time. More notably, the least acidic AlSi-50 supported catalysts suffered the greatest loss of activity. One representative catalyst from this set (0.75wt%, PTA-11) has been analyzed using STEM before and after reaction (TOS = 18h at 1.0h^{-1} WHSV). This catalyst lost 30% of its activity as listed in Table 4.2. However, representative STEM images presented in Figure 4.9, did not show any significant change in particle size in the deactivated catalyst (volume averaged particle sizes (D_v) = 2.1 ± 0.4nm before and 2.2 ± 0.6nm after reaction. This indicates that sintering of metal nanoparticles was not the cause for catalyst deactivation.

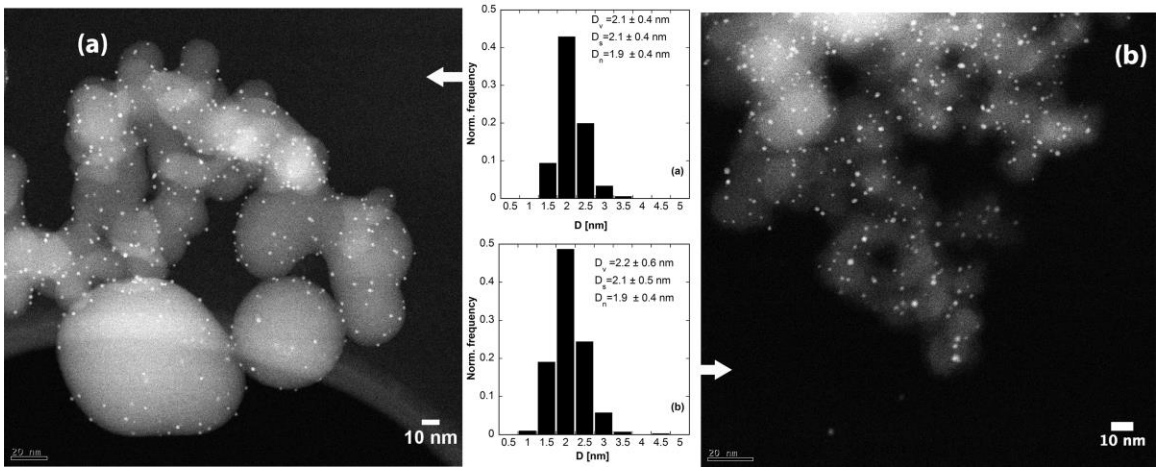

Figure 4.9. Representative high STEM images of 0.75% Pt/AlSi-50 (PTA-11) catalyst: (a) fresh catalyst, (b) after TOS=18h. Volume (D_v), surface (D_s) and number (D_n) averaged particle sizes have been included along with histograms showing distribution of metal particle size.

4.6 Discussion

4.6.1 Effect of metal-acid site ratio

In his review, Guisnet described an "ideal" bifunctional catalyst in light of the balance between metal and acid sites [127]. The performance of catalysts studied here can be similarly interpreted. To quantify the balance between active sites, the ratio of acid to active metal sites, labeled as n_a/n_{Pt}, was calculated. Such a metric has not been used often in literature [79, 84, 118]. The Pt/Al-Si, PM and layered catalysts with varying degree of acidity and metal dispersion constitute a wide variation of acid to metal site ratio. For the Pt/Al-Si catalysts, in particular, the resulting n_a/n_{Pt} ratios are included in Table 4.2. On the other hand, for the PM and layered catalysts, n_a/n_{Pt} values were determined by combining values for individual component at the respective mass ratios. The performance of the monofunctional catalysts can be used as a reference. An acidic support (SIRAL 80) in the absence of metal was completely inactive to n-C_7 conversion (Table 4.2). A much more

acidic zeolite support, metal-free, would promote cracking at these conditions [131]. On the contrary, metallic Pt/Si-50 catalyst in the absence of acid sites (n_a/n_{Pt} ~ 0) showed significant activity and selectivity towards all four types of products. Although isomerization is largely regarded to take place at the acid sites, formation of isomerized products on a monofunctional Pt/silica catalyst has been reported [137-139]. At similar conditions, monofunctional Pt catalysts can favor dehydrocyclization of long chain alkanes. During C_7 transformation, the C_5 and C_6 substituted cyclic intermediates (e.g., 1,2-dimethylcyclopentane and ethylcyclopentane) that form via dehydrocyclization on the metal sites could undergo nonselective hydrogenolysis and produce some specific i-C_7 products (e.g., 3-methylhexane, 2,3-dimethylpentane). In agreement with this, these two i-C_7 products constituted the majority (87%) of the i-C_7 products from the Pt/Si-50 catalyst.

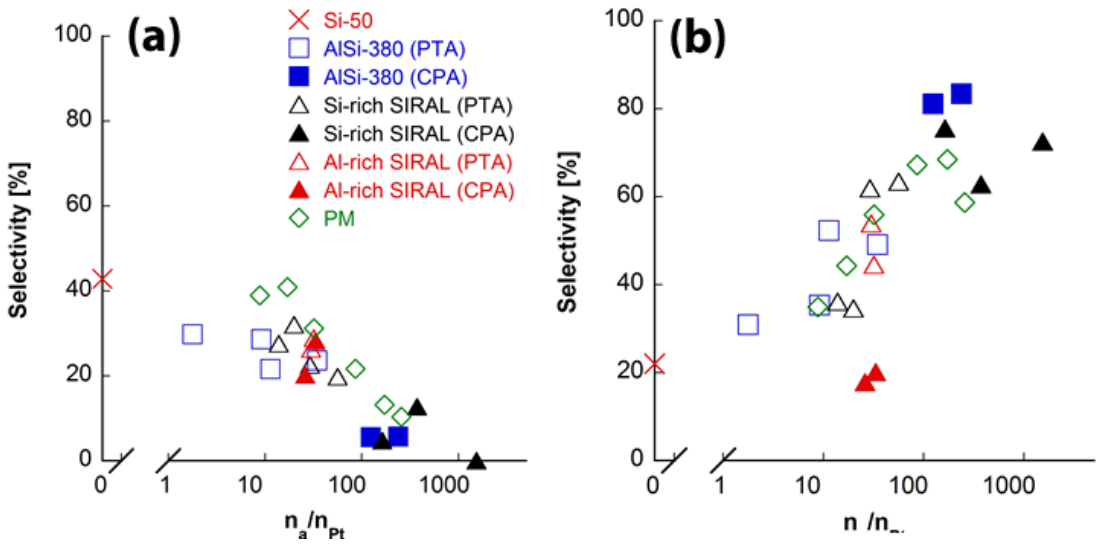

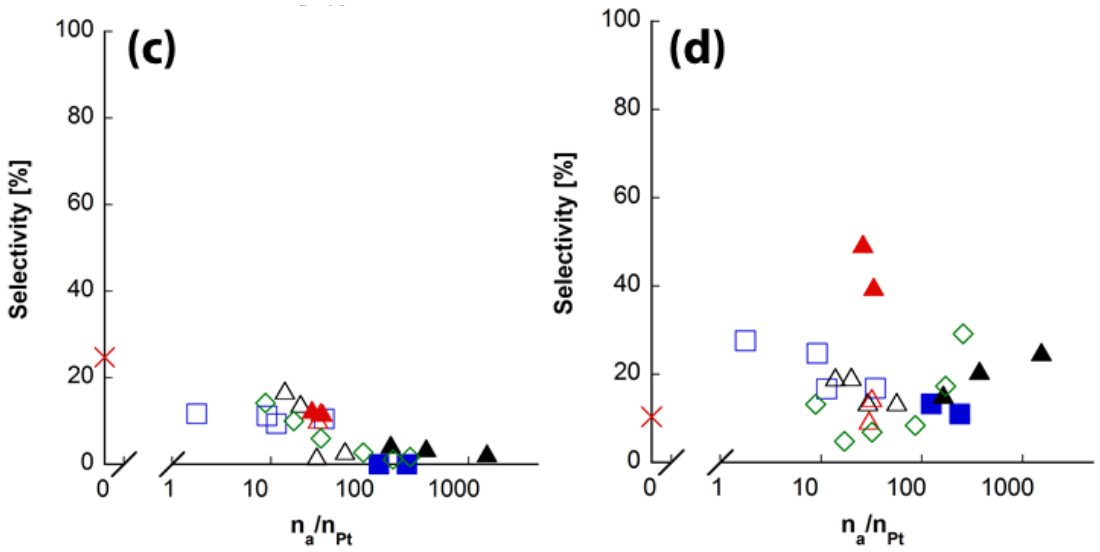

Figure 4.10. Product selectivity of all catalysts as functions of acid to metal ratio toward (a) toluene, (b) i-C_7, (c) cyclic and (d) <C_7. The legend in (a) is common to all.

For the PM catalysts, product selectivity was quite sensitive to the metal-to-acid ratio (Figure 4.8b). This offers the first glimpse on the influence of active site ratio on bifunctional performance. Product selectivity of all the catalysts have been plotted with respect to n_a/n_{Pt} in Figure 4.10 where all but the cracking product (<C_7) selectivity (Figure 4.10d) showed obvious trends regardless of Pt dispersion, nature of acid sites and proximity between metal and acid sites.

Using these n_a/n_{Pt} correlations, reaction performance of the Pt/Al-Si catalysts in Figure 4.5 can be explained. Poorly dispersed CPA-4 catalysts prepared on acidic Si-rich supports e.g., AlSi-380, SIRAL 80 had very high n_a/n_{Pt} ratio that ultimately enhanced their bifunctional nature leading to high selectivity towards i-C_7. In the PTA-11 catalysts, Pt was brought even closer to the acid sites (atomic-scale intimacy) on the same supports by maintaining high Pt dispersion (Table 4.2). Thus, due to high dispersion, the n_a/n_{Pt} ratio became too low to exhibit the same level of bifunctionality as the CPA-4 catalysts. Moreover, comparing between the PTA-DI catalysts, Pt was better dispersed over AlSi-

380 than over SIRAL 80 support with the former containing significantly less acid sites than the other (Table 4.2). This resulted in a much smaller n_a/n_{Pt} ratio in the AlSi-380 catalysts. Hence, PTA-DI catalysts over AlSi-380 acted more like the monofunctional metallic catalyst whereas SIRAL 80 supported DI catalysts were more bifunctional.

Of the four different types of products, i-C_7 is the one that primarily forms via a bifunctional pathway and is deemed the best metric for bifunctionality. TOFs of i-C_7 products per active metal site have been calculated for all the catalysts and are presented in Figure 4.11. These TOFs were based on the number of Pt sites from chemisorption (Table 4.2). At $n_a/n_{Pt} < 10$, TOFs toward i-C_7 products of all the bifunctional catalysts were more or less similar to that of monofunctional Pt/Si-50 catalyst. At $n_a/n_{Pt} > 10$, TOFs of i-C_7 increased thereby showing evidence of bifunctionality. Alvarez et al. used Pt/zeolite catalysts with various platinum loadings and showed that up to a specific metal-to-acid site ratio (0.03), activity of n-decane transformation increased linearly [84]. This means that the metallic sites act as the rate limiting sites up to this ratio which in equivalent n_a/n_{Pt} would be 33. Beyond this ratio, activity reached a plateau meaning the reactions occurring at the acid sites have become rate limiting and ideal bifunctionality conditions have been met. This trend was later confirmed as Batalha et al. expressed the activity in terms of TOF per acid site and correlated it with metal-to-acid site ratio [85]. However, for Pt/amorphous Al-Si, Regali et al [79] found that with increasing metal to acid ratio the rate of bifunctional hydrocracking of n-hexadecane remain almost unchanged and only the monofunctional hydrogenolysis reaction rate increases. However, in contrast to the present work, either a lower temperature [84] or a higher pressure [79] was used in those studies. It is widely reported that the dehydrocyclization mechanism is favored at low pressures and/or high

temperatures. Hence, such dehydrocyclization mechanism probably played no significant role in any one of these studies.

It can be summarized that under the reaction conditions explored here, bifunctional Pt/Al-Si catalysts act monofunctionally below a certain n_a/n_{Pt}. Musselwhite et al. reported similar observations using a high Pt loading on mesoporous aluminosilicates [131]. They hypothesized that there were simply too few acid sites within an "effective radius" between two Pt nanoparticles for the catalyst to be bifunctional. A minimum number of acid sites per metal site would therefore be required to fully suppress the monofunctional pathway. At the other end of the spectrum, samples with very high n_a/n_{Pt} ratios (>200) mostly corresponded to samples where Pt is very poorly dispersed (<10%). Increasing the n_a/n_{Pt} ratio clearly leads to a significant increase in TOF of i-C_7. Also according to Figure 4.11, each metal site appears capable of feeding hundreds of acid sites without affecting the reaction rate. This confirms the high hydrogenating/dehydrogenating activity of Pt particles and is consistent with the work of Batalha et al. who found that each metal site can feed ~250 acid sites without significantly affecting bifunctional activity [85]. The fact that this limit is higher in the present work might be due to an over-estimation of the number of relevant acid sites (some of the acid sites of the Al-Si determined by NH_3-TPD might be too weak to play any significant role).

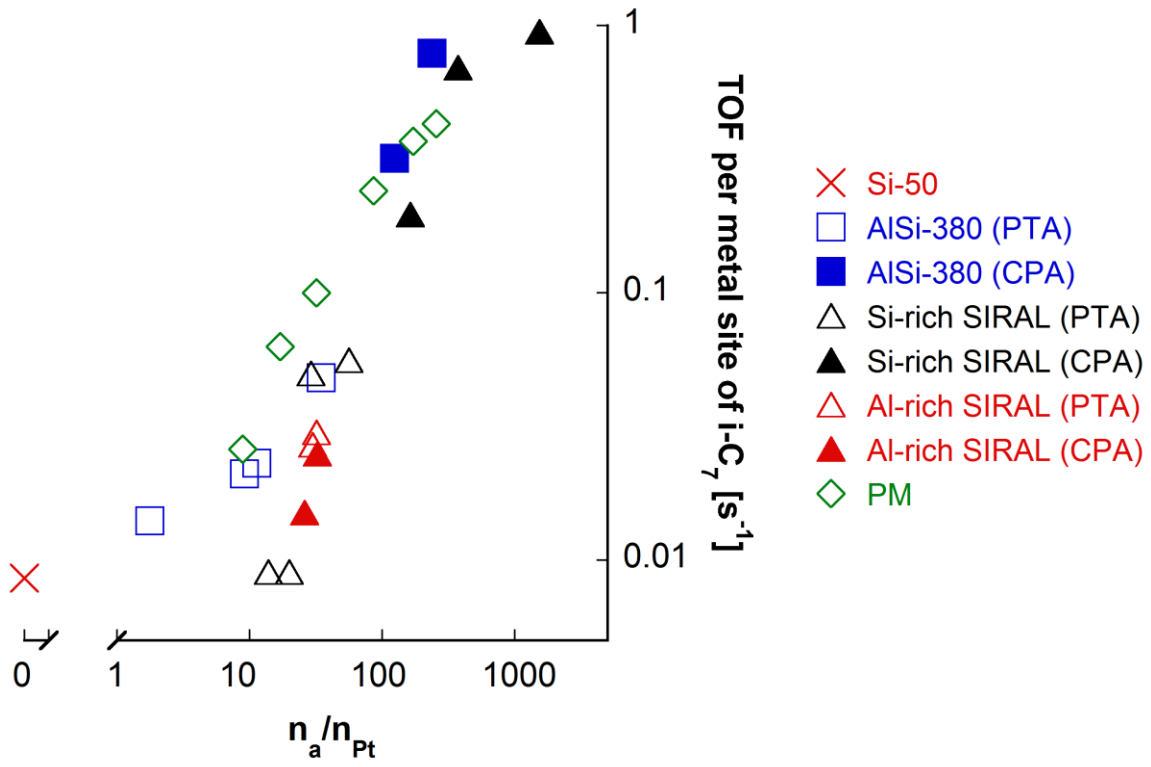

Figure 4.11. TOF (per active metal site) of i-C_7 products with respect to acid-to-metal ratio. TOF determined using conversion and selectivity of i-C_7 at 1.0h^{-1} space velocity, TOS=18h, H_2/n-C_7 = 33. Both axes are logarithmic.

4.6.2 Role of proximity

From Weisz's pioneering work on the intimacy criterion in bifunctional catalysts, it is often taken *a priori* that proximity between active sites in a bifunctional catalyst needs to be as close as possible for greatest bifunctionality [116]. However, recent results suggest that closest proximity between active sites may not always be the most beneficial; as noted above, Zečević et al. even found it to be deleterious [93]. Similarly, in this study, the i-C_7 selectivity trend in Figures 4.10b and 4.11 suggests that the CPA-4 catalyst series with nanometer scale proximity (filled blue rectangles and filled black triangles in Figures 4.10b and 4.11) are more bifunctional than the other series (PTA-11 or DI) with atomic scale proximity. The physically mixed samples at micrometer-scale intimacy (open green

rectangles in Figures 4.10b and 4.11) also exhibit greater bifunctionality than the atomically intimate catalysts (red open and filled and black open triangles, open blue squares).

In Figure 4.12, the selectivities of the i-C_7 and <C_7 products and Pt dispersion obtained for SIRAL catalysts have been plotted against alumina content. The results from both CPA-4 (Figure 4.12a) and PTA-11 (Figure 4.12b) series show that i-C_7 selectivity diminishes and <C_7 selectivity increases with Pt dispersion. This once again indicates that the catalysts with the closest (atomic scale) proximity between metal and acid sites are not the most bifunctional. It could be argued that for the CPA-4 series the retention of residual Cl^- from $[PtCl_6]^{2-}$ precursor in the alumina-rich SIRALs (SIRAL 20 and SIRAL 40), the two higher alumina wt%'s in Figures 4.12a and 4.12b, is responsible for higher cracking as chlorinated alumina has been shown to display strong Brønsted acidity which can contribute to cracking reactions [140, 141]. This would explain the difference in the selectivity of these CPA-4 and the PTA-11 catalysts which had about the same particle size (dispersion about 40%). This also explains the previously noted anomalous performance of CPA-4 catalysts on these Al-rich SIRALs in Figure 4.10 (filled red triangles). However, the residual Cl^- on these samples was too low to be detected by XPS. Moreover, the acidity of PTA-11 (no Cl) on these Al-rich SIRAL supports was found to be higher than that of the CPA-4 catalysts (NH_3-TPD profiles included in Figure 4.3).

Significant loss in bifunctionality was observed only for the layered catalysts with millimeter-scale proximity. At this point, they essentially acted as monofunctional (metallic) catalysts. However, the bifunctional reactivity of the PM catalysts, with micrometer scale metal-acid site proximity, remained intact. According to Figures 4.10 and

4.11, the product distribution and TOFs from even the micrometer intimate PM catalysts were comparable to Pt/Al-Si catalysts with similar n_a/n_{Pt} ratio. Kim et al. used zeolites crystals with different thickness (from bulk crystals to nanosheets) and showed that selectivity of n-C_7 conversion remained nearly unchanged up to 300nm distance between metal and acid sites [136].

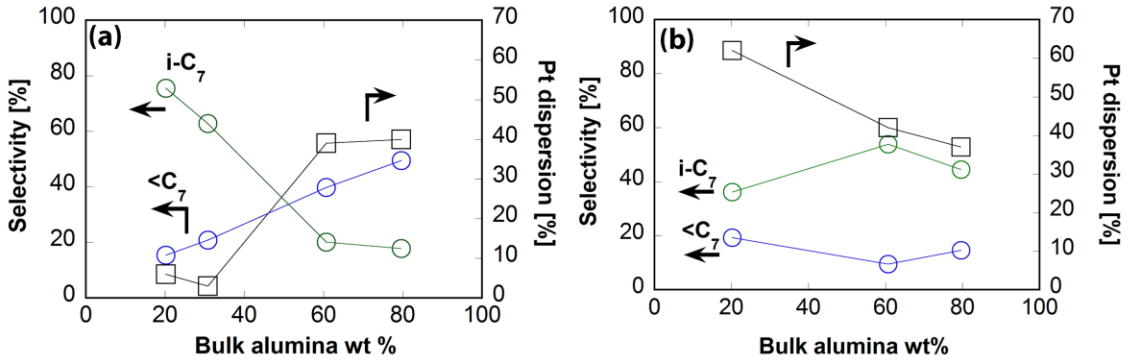

Figure 4.12. Product (i-C_7 and <C_7) selectivity and Pt dispersion of SIRAL Al-Si supported (a) CPA-4 and (b) PTA-11 catalysts with 0.7wt% Pt.

4.7 Conclusions

A series of bifunctional metal (platinum)-acid (silica-alumina) catalysts with a wide range of ratio and proximity between metal and acid sites was studied in n-heptane conversion reaction. Based on the results, following calculations were drawn:

[1] Depending on synthesis conditions, the total number of available metal and acid sites in Pt/silica-alumina was found to vary significantly. This variation can modify the balance between active sites and thereby affect catalytic performance.

[2] In order to preserve bifunctionality, it is essential for Pt/silica-alumina catalysts to maintain an acid-to-metal site ratio above a certain value. Below this value, the catalyst would essentially act as a monofunctional catalyst.

[3] Pt/Al-Si catalysts with nanometer scale proximity acted more bifunctionally (higher i-C_7 selectivity) than those with atomic scale proximity.

4.8 Future work

Knowledge gained from this work could be advanced in future works involving metal-acid bifunctional catalysis. As for example, well-dispersed Pt/Al-Si catalysts with low Pt loading and hence high acid to metal site ratio could be prepared to study activity and selectivity at atomic scale proximity. Nature and strength of acid sites on the Pt loaded catalysts could be characterized using Pyridine or Lutidine IR analysis.

References

[1] J.R. Regalbuto, 13 Strong Electrostatic Adsorption of Metals onto Catalyst Supports, in: Catalyst Preparation: Science and Engineering, 2006, pp. 297.
[2] J.R. Regalbuto, A scientific method to prepare supported metal catalysts, Surface and Nanomolecular Catalysis, (2006) 161-194.
[3] C. Cao, G. Yang, L. Dubau, F. Maillard, S.D. Lambert, J.-P. Pirard, N. Job, Highly dispersed Pt/C catalysts prepared by the Charge Enhanced Dry Impregnation method, Applied Catalysis B: Environmental, 150–151 (2014) 101-106.
[4] X. Zhu, H.-r. Cho, M. Pasupong, J.R. Regalbuto, Charge-Enhanced Dry Impregnation: A Simple Way to Improve the Preparation of Supported Metal Catalysts, ACS Catalysis, 3 (2013) 625-630.
[5] X. Hao, W. Spieker, J. Regalbuto, A further simplification of the revised physical adsorption (RPA) model, Journal of colloid and interface science, 267 (2003) 259-264.
[6] M. Schreier, J.R. Regalbuto, A fundamental study of Pt tetraammine impregnation of silica: 1. The electrostatic nature of platinum adsorption, Journal of Catalysis, 225 (2004) 190-202.
[7] C. Perego, P. Villa, Catalyst preparation methods, Catalysis Today, 34 (1997) 281-305.
[8] F. Pinna, Supported metal catalysts preparation, Catalysis Today, 41 (1998) 129-137.
[9] M. Sterrer, H.-J. Freund, Towards Realistic Surface Science Models of Heterogeneous Catalysts: Influence of Support Hydroxylation and Catalyst Preparation Method, Catal Lett, 143 (2013) 375-385.
[10] M.L. Toebes, J.A. van Dillen, K.P. de Jong, Synthesis of supported palladium catalysts, Journal of Molecular Catalysis A: Chemical, 173 (2001) 75-98.
[11] C. Conţescu, M. Vass, The effect of pH on the adsorption of palladium (II) complexes on alumina, Applied catalysis, 33 (1987) 259-271.
[12] M. Heise, J. Schwarz, Preparation of metal distributions within catalyst supports. I. Effect of ph on catalytic metal profiles, Journal of colloid and interface science, 107 (1985) 237-243.
[13] X. Hao, W.A. Spieker, J.R. Regalbuto, A further simplification of the revised physical adsorption (RPA) model, Journal of colloid and interface science, 267 (2003) 259-264.
[14] W.A. Spieker, J.R. Regalbuto, A fundamental model of platinum impregnation onto alumina, Chemical Engineering Science, 56 (2001) 3491-3504.
[15] J.L. Ewbank, L. Kovarik, C.C. Kenvin, C. Sievers, Effect of preparation methods on the performance of Co/Al2O3 catalysts for dry reforming of methane, Green Chemistry, 16 (2014) 885-896.
[16] L. Jiao, J.R. Regalbuto, The synthesis of highly dispersed noble and base metals on silica via strong electrostatic adsorption: I. Amorphous silica, Journal of Catalysis, 260 (2008) 329-341.
[17] S. Lambert, N. Job, L. D'Souza, M.F.R. Pereira, R. Pirard, B. Heinrichs, J.L. Figueiredo, J.-P. Pirard, J.R. Regalbuto, Synthesis of very highly dispersed platinum

catalysts supported on carbon xerogels by the strong electrostatic adsorption method, Journal of Catalysis, 261 (2009) 23-33.
[18] J. Liu, R. Tao, Z. Guo, J.R. Regalbuto, C.L. Marshall, R.F. Klie, J.T. Miller, R.J. Meyer, Selective Adsorption of Manganese onto Rhodium for Optimized Mn/Rh/SiO2 Alcohol Synthesis Catalysts, ChemCatChem, 5 (2013) 3665-3672.
[19] L. Zhang, G. Wen, H. Liu, N. Wang, D.S. Su, Preparation of Palladium Catalysts Supported on Carbon Nanotubes by an Electrostatic Adsorption Method, ChemCatChem, 6 (2014) 2600-2606.
[20] J. Park, J.R. Regalbuto, A Simple, Accurate Determination of Oxide PZC and the Strong Buffering Effect of Oxide Surfaces at Incipient Wetness, Journal of Colloid and Interface Science, 175 (1995) 239-252.
[21] N. Santhanam, T. Conforti, W. Spieker, J. Regalbuto, Nature of metal catalyst precursors adsorbed onto oxide supports, Catalysis today, 21 (1994) 141-156.
[22] Q. Liu, U.A. Joshi, K. Über, J.R. Regalbuto, The control of Pt and Ru nanoparticle size on high surface area supports, Physical Chemistry Chemical Physics, 16 (2014) 26431-26435.
[23] N. Job, S.D. Lambert, A. Zubiaur, C. Cao, J.-P. Pirard, Design of Pt/carbon xerogel catalysts for PEM fuel cells, Catalysts, 5 (2015) 40-57.
[24] J.E. Samad, J. Keels, J.R. Regalbuto, A Comparison of Pt (II) and Pt (IV) Chloride Precursors for Strong Electrostatic Adsorption Synthesis of Pt/Alumina and Pt/Carbon Catalysts, Catal Lett, 1-6.
[25] R.O. James, T.W. Healy, Adsorption of hydrolyzable metal ions at the oxide—water interface. III. A thermodynamic model of adsorption, Journal of Colloid and Interface Science, 40 (1972) 65-81.
[26] J. Regalbuto, A. Navada, S. Shadid, M. Bricker, Q. Chen, An experimental verification of the physical nature of Pt adsorption onto alumina, Journal of Catalysis, 184 (1999) 335-348.
[27] K. Punyawudho, D.A. Blom, J.W. Van Zee, J.R. Monnier, Comparison of different methods for determination of Pt surface site concentrations for supported Pt electrocatalysts, Electrochimica Acta, 55 (2010) 5349-5356.
[28] M. Schreier, T.E. Feltes, M.T. Schaal, J.R. Regalbuto, The determination of oxide surface charging parameters for a predictive metal adsorption model, Journal of Colloid and Interface Science, 348 (2010) 571-578.
[29] W. Spieker, J. Regalbuto, A fundamental model of platinum impregnation onto alumina, Chemical Engineering Science, 56 (2001) 3491-3504.
[30] P. Castillo-Villalón, J. Ramírez, M.-J. Peltre, C. Louis, P. Massiani, An UV-Visible study of the stability of the ruthenium hexaammine cation in BEA zeolites—comparison with NaY, Physical Chemistry Chemical Physics, 6 (2004) 3739-3746.
[31] J.J. Verdonck, R.A. Schoonheydt, P.A. Jacobs, Chemistry of hexaammineruthenium (3+) in zeolites. 1. Thermal decomposition and interaction with oxygen, water, and nitric oxide, The Journal of Physical Chemistry, 85 (1981) 2393-2398.
[32] L.A. De Faria, S. Trasatti, Physical versus chemical mixtures of oxides: the point of zero charge of Ni+Co mixed oxides, Journal of Electroanalytical Chemistry, 554 (2003) 355-359.
[33] B. Gates, Catalytic Chemistry, John Wiley and Sons, New York, 1992.

[34] I. Wacks, Characterization of catalytic materials, Manning Publications, Greenwich, 1992.
[35] K.D. Zhi, Q.S. Liu, R.G. Zhao, R.X. He, L.F. Zhang, Preparation and characterization of Cu-Ce-La mixed oxide as water-gas shift catalyst for fuel cells application, Journal of Rare Earths, 26 (2008) 538-543.
[36] A.N. Chowdhury, A. Rahim, Y.J. Ferdosi, M.S. Azam, M.M. Hossain, Cobalt-nickel mixed oxide surface: A promising adsorbent for the removal of PR dye from water, Applied Surface Science, 256 (2010) 3718-3724.
[37] M. Mullet, P. Fievet, J.C. Reggiani, J. Pagetti, Surface electrochemical properties of mixed oxide ceramic membranes: Zeta-potential and surface charge density, Journal of Membrane Science, 123 (1997) 255-265.
[38] D. Sathiyamoorthy, S.J. Ghanwat, B.M. Tripathi, C. Danani, Novel mixed-oxide ceramic for neutron multiplication and tritium generation, Journal of Nuclear Materials, 417 (2011) 775-779.
[39] J. Shen, A.D. Ebner, J.A. Ritter, Points of Zero Charge and Intrinsic Equilibrium Constants of Silica‚ÄìMagnetite Composite Oxides, Journal of Colloid and Interface Science, 214 (1999) 333-343.
[40] K. Zakrzewska, Mixed oxides as gas sensors, Thin Solid Films, 391 (2001) 229-238.
[41] Q. Zhang, W. Jing, Y. Fan, N. Xu, An improved Parks equation for prediction of surface charge properties of composite ceramic membranes, Journal of Membrane Science, 318 (2008) 100-106.
[42] L.A. De Faria, M. Prestat, J.F. Koenig, P. Chartier, S. Trasatti, Surface properties of Ni+Co mixed oxides: a study by X-rays, XPS, BET and PZC, Electrochimica Acta, 44 (1998) 1481-1489.
[43] M. Farooq, A. Ramli, D. Subbarao, Physiochemical Properties of gamma-Al2O3-MgO and gamma-Al2O3-CeO2 Composite Oxides, Journal of Chemical and Engineering Data, 57 (2012) 26-32.
[44] J.C. Vickerman, I.S. Gilmore, Surface Analysis : The Principal Techniques, in, John Wiley & Sons Ltd, West Sussex, 2009.
[45] M. Waseem, S. Mustafa, A. Naeem, G.J.M. Koper, D. Salah ud, Physiochemical properties of mixed oxides of iron and silicon, Journal of Non-Crystalline Solids, 356 (2010) 2704-2708.
[46] R. Zhang, J.A. Schwarz, A. Datye, J.P. Baltrus, The effect of 2nd-phase oxides on the catalytic properties of dispersed metals-Platinum supported on 12%WO3/Al2O3, Journal of Catalysis, 138 (1992) 55-69.
[47] C. Satterfield, Heterogeneous catalysis in Industrial Practice, McGraw-Hill, New York, 1991.
[48] R.L. Brady, D. Southmayd, C. Contescu, R. Zhang, J.A. Schwarz, Surface-area determination of supported oxides - WO3/Al2O3, Journal of Catalysis, 129 (1991) 195-201.
[49] J.A. Schwarz, C.T. Ugbor, R. Zhang, The adsorption/impregnation of Pd(II) cations on alumina, silica, and their composite oxides, Journal of Catalysis, 138 (1992) 38-54.
[50] J.A. Schwarz, C.T. Driscoll, A.K. Bhanot, The zero-point of charge of silica-alumina oxide suspensions, Journal of Colloid and Interface Science, 97 (1984) 55-61.
[51] G.A. Parks, Aqueous surface chemistry of oxides and complex oxide minerals, Advances in Chemistry Series, (1967) 121-&.

[52] M.A.F. Pyman, J.W. Bowden, A.M. Posner, Point of zero charge of amorphous coprecipitates of silica with hydrous aluminum or ferric hydroxide, Clay Minerals, 14 (1979) 87-92.
[53] M. Tschapek, L. Tcheichvili, C. Wasowski, Point of zero charge (pzc) of kaolinite and sio2+al2o3 mixtures, Clay Minerals, 10 (1974) 219-229.
[54] S. Subramanian, J.S. Noh, J.A. Schwarz, Determination of the point of zero-charge of composite oxides, Journal of Catalysis, 114 (1988) 433-439.
[55] J.F. Kuo, T.F. Yen, Some aspects in predicting the point of zero charge of a composite oxide system, Journal of Colloid and Interface Science, 121 (1988) 220-225.
[56] L.J. Criscenti, D.A. Sverjensky, A single-site model for divalent transition and heavy metal adsorption over a range of metal concentrations, Journal of colloid and interface science, 253 (2002) 329-352.
[57] T. Hiemstra, W.H. Van Riemsdijk, On the relationship between charge distribution, surface hydration, and the structure of the interface of metal hydroxides, Journal of Colloid and Interface Science, 301 (2006) 1-18.
[58] M.K. Ridley, T. Hiemstra, W.H. Van Riemsdijk, M.L. Machesky, Inner-sphere complexation of cations at the rutile–water interface: a concise surface structural interpretation with the CD and MUSIC model, Geochimica et Cosmochimica Acta, 73 (2009) 1841-1856.
[59] D.A. Sverjensky, Prediction of surface charge on oxides in salt solutions: revisions for 1: 1 (M+ L−) electrolytes, Geochimica et Cosmochimica Acta, 69 (2005) 225-257.
[60] J.S. Noh, J.A. Schwarz, Estimation of surface ionization constants for amphoteric solids, Journal of colloid and interface science, 139 (1990) 139-148.
[61] T. Hiemstra, W.H. Van Riemsdijk, A surface structural approach to ion adsorption: the charge distribution (CD) model, Journal of Colloid and Interface Science, 179 (1996) 488-508.
[62] K. Bourikas, J. Vakros, C. Kordulis, A. Lycourghiotis, Potentiometric mass titrations: experimental and theoretical establishment of a new technique for determining the point of zero charge (PZC) of metal (hydr) oxides, The Journal of Physical Chemistry B, 107 (2003) 9441-9451.
[63] J.E. Samad, S. Hashim, S. Ma, J.R. Regalbuto, Determining surface composition of mixed oxides with pH, Journal of colloid and interface science, 436 (2014) 204-210.
[64] X. Meng, R.D. Letterman, Effect of component oxide interaction on the adsorption properties of mixed oxides, Environmental Science & Technology, 27 (1993) 970-975.
[65] X. Meng, R.D. Letterman, Modeling ion adsorption on aluminum hydroxide-modified silica, Environmental Science & Technology, 27 (1993) 1924-1929.
[66] S. Zalac, N. Kallay, Application of mass titration to the point of zero charge determination, Journal of Colloid and Interface Science, 149 (1992) 233-240.
[67] M.B. Gawande, R.K. Pandey, R.V. Jayaram, Role of mixed metal oxides in catalysis science - versatile applications in organic synthesis, Catalysis Science & Technology, 2 (2012) 1113-1125.
[68] E.J.M. Hensen, D.G. Poduval, P. Magusin, A.E. Coumans, J.A.R. Van Veen, Formation of acid sites in amorphous silica-alumina, Journal of Catalysis, 269 (2010) 201-218.

[69] M.A. Arribas, A. Corma, M.J. Diaz-Cabanas, A. Martinez, Hydrogenation and ring opening of Tetralin over bifunctional catalysts based on the new ITQ-21 zeolite, Applied Catalysis a-General, 273 (2004) 277-286.
[70] D. Kubicka, N. Kumar, P. Maki-Arvela, M. Tiitta, V. Niemi, H. Karhu, T. Sami, D.Y. Murzin, Ring opening of decalin over zeolites - II. Activity and selectivity of platinum-modified zeolites, Journal of Catalysis, 227 (2004) 313-327.
[71] S.A.K. Kumar, M. John, S.M. Pai, Y. Niwate, B.L. Newalkar, Low temperature hydrogenation of aromatics over Pt-Pd/SiO2-Al 2 O 3 catalyst, Fuel Processing Technology, 128 (2014) 303-309.
[72] L.M. Kustov, A.Y. Stakheev, T.V. Vasina, O.V. Masloboishchikova, E.G. Khelkovskaya-Sergeeva, P. Zeuthen, A.G.-R.a.I. Rodriguez-Ramos, Dual-function catalysts for ring opening of cyclic compounds, in: Studies in Surface Science and Catalysis, Elsevier, 2001, pp. 307-314.
[73] S. Nassreddine, S. Casu, J.L. Zotin, C. Geantet, L. Piccolo, Thiotolerant Ir/SiO 2-Al 2 O 3 bifunctional catalysts: effect of support acidity on tetralin hydroconversion, Catalysis Science & Technology, 1 (2011) 408-412.
[74] P. Barbaro, F. Liguori, N. Linares, C.M. Marrodan, Heterogeneous bifunctional metal/acid catalysts for selective chemical processes, European Journal of Inorganic Chemistry, 2012 (2012) 3807-3823.
[75] Y. Izutsu, Y. Oku, Y. Hidaka, K. Yoshida, Y. Sasaki, Y. Sekine, E. Kikuchi, M. Matsukata, Synthesis and Characterization of Chromium-Added Pt/Beta Zeolite and its Catalytic Performance for n-Heptane Isomerization, Catal Lett, 143 (2013) 486-494.
[76] N. Musselwhite, K. Na, S. Alayoglu, G.A. Somorjai, The Pathway to Total Isomer Selectivity: n-Hexane Conversion (Reforming) on Platinum Nanoparticles Supported on Aluminum Modified Mesoporous Silica (MCF-17), Journal of the American Chemical Society, 136 (2014) 16661-16665.
[77] N. Parsafard, M.H. Peyrovi, M. Rashidzadeh, n-Heptane isomerization on a new kind of micro/mesoporous catalyst: Pt supported on HZSM-5/HMS, Microporous and Mesoporous Materials, 200 (2014) 190-198.
[78] M.H. Peyrovi, T. Hamoule, Study of catalytic properties of Pt/Al-HMS catalysts in n-heptane hydroisomerization, Reaction Kinetics, Mechanisms and Catalysis, 106 (2012) 233-243.
[79] F. Regali, L.F. Liotta, A.M. Venezia, M. Boutonnet, S. Järås, Hydroconversion of n-hexadecane on Pt/silica-alumina catalysts: Effect of metal loading and support acidity on bifunctional and hydrogenolytic activity, Applied Catalysis A: General, 469 (2014) 328-339.
[80] F. Regali, L.F. Liotta, A.M. Venezia, V. Montes, M. Boutonnet, S. Jaras, Effect of metal loading on activity, selectivity and deactivation behavior of Pd/silicaâ€“alumina catalysts in the hydroconversion of n-hexadecane, Catalysis Today, 223 (2014) 87-96.
[81] S.A. D'Ippolito, C. Especel, L. Vivier, F. Epron, C.L. Pieck, Influence of the BrÃ¸nsted acidity, SiO2/Al2O3 ratio and Rhâ€“Pd content on the ring opening: Part I. Selective ring opening of decalin, Applied Catalysis A: General, 469 (2014) 532-540.
[82] N. Batalha, L. Pinard, Y. Pouilloux, M. Guisnet, Bifunctional hydrogenating/acid catalysis: quantification of the intimacy criterion, Catal Lett, 143 (2013) 587-591.
[83] T. Yashima, Z.-B. Wang, A. Kamo, T. Yoneda, T. Komatsu, Isomerization of n-hexane over Platinum loaded zeolite catalysts, Catalysis Today, 29 (1996) 279-283.

[84] F. Alvarez, F.R. Ribeiro, G. Perot, C. Thomazeau, M. Guisnet, Hydroisomerization and Hydrocracking of Alkanes: 7. Influence of the Balance between Acid and Hydrogenating Functions on the Transformation ofn-Decane on PtHY Catalysts, Journal of Catalysis, 162 (1996) 179-189.
[85] N. Batalha, L. Pinard, C. Bouchy, E. Guillon, M. Guisnet, n-Hexadecane hydroisomerization over Pt-HBEA catalysts. Quantification and effect of the intimacy between metal and protonic sites, Journal of Catalysis, 307 (2013) 122-131.
[86] M.B. Gawande, R.K. Pandey, R.V. Jayaram, Role of mixed metal oxides in catalysis scienceâ€"versatile applications in organic synthesis, Catalysis Science & Technology, 2 (2012) 1113-1125.
[87] P. Courty, C. Marcilly, A scientific approach to the preparation of bulk mixed oxide catalysts, Studies in Surface Science and Catalysis, 16 (1983) 485-519.
[88] M. Valla, A.J. Rossini, M. Caillot, C. Chizallet, P. Raybaud, M. Digne, A. Chaumonnot, A. Lesage, L. Emsley, J.A. Van Bokhoven, Atomic Description of the Interface between Silica and Alumina in Aluminosilicates through Dynamic Nuclear Polarization Surface-Enhanced NMR Spectroscopy and First-Principles Calculations, Journal of the American Chemical Society, 137 (2015) 10710-10719.
[89] E.J.M. Hensen, D.G. Poduval, V. Degirmenci, D.A.J.M. Ligthart, W. Chen, F.o. Maugé, M.S. Rigutto, J.A.R.v. Veen, Acidity characterization of amorphous silica–alumina, The Journal of Physical Chemistry C, 116 (2012) 21416-21429.
[90] N. Kumar, A. Lazuen, D. Kubicka, T. Heikkilä, V.P. Lehto, H. Karhu, T. Salmi, D.Y. Murzin, Synthesis of Pt-modified MCM-41 mesoporous molecular sieve catalysts: influence of methods of Pt introduction in MCM-41 on physico-chemical and catalytic properties for ring opening of decalin, Studies in surface science and catalysis, 162 (2006) 401-408.
[91] J.A. Schwarz, C. Contescu, A. Contescu, Methods for preparation of catalytic materials, Chemical Reviews, 95 (1995) 477-510.
[92] M. Mihaylov, K. Hadjiivanov, N. Abadjieva, D. Klissurski, L. Mintchev, Characterization of Zirconia-supported Nickel Catalysts Prepared by Multiple Ion-exchange, Studies in Surface Science and Catalysis, 118 (1998) 295-304.
[93] J. Zecevic, G. Vanbutsele, K.P. de Jong, J.A. Martens, Nanoscale intimacy in bifunctional catalysts for selective conversion of hydrocarbons, Nature, 528 (2015) 245-248.
[94] O.Y. Gutierrez, Y. Yu, R. Kolvenbach, G.L. Haller, J.A. Lercher, Hydrogenation of tetralin over Pt catalysts supported on sulfated zirconia and amorphous silica alumina, Catalysis Science & Technology, 3 (2013) 2365-2372.
[95] S. Handjani, S. Dzwigaj, J. Blanchard, E. Marceau, J.-M. Krafft, M. Che, Comparing Al-SBA-15 Support and Pt/Al-SBA-15 Catalyst: Changes in Al Speciation and Acidic Properties Induced by the Introduction of Pt via Aqueous Medium, Topics in Catalysis, 52 (2009) 334-343.
[96] M. Iwamoto, H. Yahiro, Y. Torikai, T. Yoshioka, N. Mizuno, Novel preparation method of highly copper ion-exchanged ZSM-5 zeolites and their catalytic activities for NO decomposition, Chemistry Letters, (1990) 1967-1970.
[97] M. Schreier, S. Teren, L. Belcher, J.R. Regalbuto, J.T. Miller, The nature of'overexchanged'copper and platinum on zeolites, Nanotechnology, 16 (2005) S582.

[98] T.E. Feltes, L. Espinosa-Alonso, E. de Smit, L. D'Souza, R.J. Meyer, B.M. Weckhuysen, J.R. Regalbuto, Selective adsorption of manganese onto cobalt for optimized Mn/Co/TiO 2 Fischer–Tropsch catalysts, Journal of Catalysis, 270 (2010) 95-102.
[99] Y. Zha, The Rational Preparation of Niobia Supported and Promoted Platinum Catalysts, in, University of Illinois at Chicago, 2007.
[100] S.Q. Zeng, J. Blanchard, M. Breysse, Y.H. Shi, X.T. Shu, H. Nie, D.D. Li, Post-synthesis alumination of SBA-15 in aqueous solution: A versatile tool for the preparation of acidic Al-SBA-15 supports, Microporous and Mesoporous Materials, 85 (2005) 297-304.
[101] G. Furrer, C. Ludwig, P.W. Schindler, On the chemistry of the Keggin Al13 polymer: I. Acid-base properties, Journal of colloid and interface science, 149 (1992) 56-67.
[102] X. Wu, X. Ge, D. Wang, H. Tang, Distinct coagulation mechanism and model between alum and high Al 13-PACl, Colloids and Surfaces A: Physicochemical and Engineering Aspects, 305 (2007) 89-96.
[103] A. Meyer, German Patent, in: G. Patent (Ed.), DE, 1990.
[104] K. O'Connell, J. Regalbuto, High Sensitivity Silicon Slit Detectors for 1 nm Powder XRD Size Detection Limit, Catal Lett, 145 (2015) 777-783.
[105] T.E. Whyte Jr, Metal particle size determination of supported metal catalysts, Catalysis Reviews, 8 (1974) 117-134.
[106] Verma, Atomic and nuclear analytical methods: XRF, Mossbauer, XPS, NAA and ion beam spectroscopic techniques, in, Springer, Berlin, 2007, pp. 241.
[107] C.A. Monteiro, D. Costa, J.L. Zotin, D. Cardoso, Effect of metal–acid site balance on hydroconversion of decalin over Pt/Beta zeolite bifunctional catalysts, Fuel, 160 (2015) 71-79.
[108] Y. Wang, Z. Tao, B. Wu, J. Xu, C. Huo, K. Li, H. Chen, Y. Yang, Y. Li, Effect of metal precursors on the performance of Pt/ZSM-22 catalysts for n-hexadecane hydroisomerization, Journal of Catalysis, 322 (2015) 1-13.
[109] F. Anaya, L. Zhang, Q. Tan, D.E. Resasco, Tuning the acid–metal balance in Pd/and Pt/zeolite catalysts for the hydroalkylation of m-cresol, Journal of Catalysis, 328 (2015) 173-185.
[110] G. McVicker, M. Daage, M. Touvelle, C. Hudson, D. Klein, W. Baird, B. Cook, J. Chen, S. Hantzer, D. Vaughan, Selective ring opening of naphthenic molecules, Journal of Catalysis, 210 (2002) 137-148.
[111] H. Du, C. Fairbridge, H. Yang, Z. Ring, The chemistry of selective ring-opening catalysts, Applied Catalysis A: General, 294 (2005) 1-21.
[112] C.R. Lee, J.S. Yoon, Y.-W. Suh, J.-W. Choi, J.-M. Ha, D.J. Suh, Y.-K. Park, Catalytic roles of metals and supports on hydrodeoxygenation of lignin monomer guaiacol, Catalysis Communications, 17 (2012) 54-58.
[113] J.C. Serrano-Ruiz, J.A. Dumesic, Catalytic routes for the conversion of biomass into liquid hydrocarbon transportation fuels, Energy & Environmental Science, 4 (2011) 83-99.
[114] Y. Yoneyama, J. He, Y. Morii, S. Azuma, N. Tsubaki, Direct synthesis of isoparaffin by modified Fischer–Tropsch synthesis using hybrid catalyst of iron catalyst and zeolite, Catalysis today, 104 (2005) 37-40.
[115] S. Sartipi, M. Makkee, F. Kapteijn, J. Gascon, Catalysis engineering of bifunctional solids for the one-step synthesis of liquid fuels from syngas: a review, Catalysis Science & Technology, 4 (2014) 893-907.

[116] P.B. Weisz, Polyfunctional Heterogeneous Catalysis, Academic Press, 1962.
[117] J. Francis, E. Guillon, N. Bats, C. Pichon, A. Corma, L.J. Simon, Design of improved hydrocracking catalysts by increasing the proximity between acid and metallic sites, Applied Catalysis A: General, 409–410 (2011) 140-147.
[118] N. Batalha, L. Pinard, Y. Pouilloux, M. Guisnet, Bifunctional hydrogenating/acid catalysis: quantification of the intimacy criterion, Catal Lett, 143 587-591.
[119] J. Samad, J. Blanchard, C. Sayag, C. Louis, J. Regalbuto, in, 2016.
[120] A. Zhang, I. Nakamura, K. Aimoto, K. Fujimoto, Isomerization of n-pentane and other light hydrocarbons on hybrid catalyst. Effect of hydrogen spillover, Industrial & engineering chemistry research, 34 (1995) 1074-1080.
[121] E. Iglesia, D.G. Barton, S.L. Soled, S. Miseo, J.E. Baumgartner, W.E. Gates, G.A. Fuentes, G.D. Meitzner, Selective isomerization of alkanes on supported tungsten oxide acids, Studies in surface science and catalysis, 101 (1996) 533-542.
[122] M. Höchtl, A. Jentys, H. Vinek, Alkane conversion over Pd/SAPO molecular sieves: influence of acidity, metal concentration and structure, Catalysis today, 65 (2001) 171-177.
[123] F. Roessner, U. Roland, Hydrogen spillover in bifunctional catalysis, Journal of Molecular Catalysis A: Chemical, 112 (1996) 401-412.
[124] R. Prins, Hydrogen Spillover. Facts and Fiction, Chemical Reviews, 112 (2012) 2714-2738.
[125] J. Im, H. Shin, H. Jang, H. Kim, M. Choi, Maximizing the catalytic function of hydrogen spillover in platinum-encapsulated aluminosilicates with controlled nanostructures, Nat Commun, 5 (2014).
[126] J. Weitkamp, Catalytic Hydrocracking—Mechanisms and Versatility of the Process, ChemCatChem, 4 (2012) 292-306.
[127] M. Guisnet, "Ideal" bifunctional catalysis over Pt-acid zeolites, Catalysis Today, 218–219 (2013) 123-134.
[128] F. Anaya, L. Zhang, Q. Tan, D.E. Resasco, Tuning the acid–metal balance in Pd/ and Pt/zeolite catalysts for the hydroalkylation of m-cresol, Journal of Catalysis, 328 (2015) 173-185.
[129] A. de Lucas, P. Sánchez, F. Dorado, M.J. Ramos, J.L. Valverde, Effect of the metal loading in the hydroisomerization of n-octane over beta agglomerated zeolite based catalysts, Applied Catalysis A: General, 294 (2005) 215-225.
[130] S. Nassreddine, L. Massin, M. Aouine, C. Geantet, L. Piccolo, Thiotolerant Ir/SiO2–Al2O3 bifunctional catalysts: Effect of metal–acid site balance on tetralin hydroconversion, Journal of Catalysis, 278 (2011) 253-265.
[131] N. Musselwhite, K. Na, K. Sabyrov, S. Alayoglu, G.A. Somorjai, Mesoporous Aluminosilicate Catalysts for the Selective Isomerization of n-Hexane: The Roles of Surface Acidity and Platinum Metal, Journal of the American Chemical Society, 137 (2015) 10231-10237.
[132] D. Kubička, N. Kumar, P. Mäki-Arvela, M. Tiitta, V. Niemi, H. Karhu, T. Salmi, D.Y. Murzin, Ring opening of decalin over zeolites: II. Activity and selectivity of platinum-modified zeolites, Journal of Catalysis, 227 (2004) 313-327.
[133] A. Soualah, J.L. Lemberton, L. Pinard, M. Chater, P. Magnoux, K. Moljord, Hydroisomerization of long-chain n-alkanes on bifunctional Pt/zeolite catalysts: Effect of the zeolite structure on the product selectivity and on the reaction mechanism, Applied Catalysis A: General, 336 (2008) 23-28.

[134] G. Kinger, D. Majda, H. Vinek, n-Heptane hydroisomerization over Pt-containing mixtures of zeolites with inert materials, Applied Catalysis A: General, 225 (2002) 301-312.
[135] R. Le Van Mao, Hybrid catalyst containing a microporous zeolite and a mesoporous cocatalyst forming a pore continuum for a better desorption of reaction products, Microporous and mesoporous materials, 28 (1999) 9-17.
[136] J. Kim, W. Kim, Y. Seo, J.-C. Kim, R. Ryoo, n-Heptane hydroisomerization over Pt/MFI zeolite nanosheets: Effects of zeolite crystal thickness and platinum location, Journal of Catalysis, 301 (2013) 187-197.
[137] H. Belatel, H. Al-Kandari, F. Al-Khorafi, A. Katrib, F. Garin, Catalytic reactions of methylcyclohexane (MCH) on partially reduced MoO 3, Applied Catalysis A: General, 275 (2004) 141-147.
[138] P. Mériaudeau, C. Naccache, Dehydrocyclization of alkanes over zeolite-supported metal catalysts: monofunctional or bifunctional route, Catalysis Reviews, 39 (1997) 5-48.
[139] B.H. Davis, Alkane dehydrocyclization mechanism, Catalysis today, 53 (1999) 443-516.
[140] G. Leofanti, A. Marsella, B. Cremaschi, M. Garilli, A. Zecchina, G. Spoto, S. Bordiga, P. Fisicaro, G. Berlier, C. Prestipino, G. Casali, C. Lamberti, Alumina-Supported Copper Chloride: 3. Effect of Exposure to Ethylene, Journal of Catalysis, 202 (2001) 279-295.
[141] D. Guillaume, S. Gautier, F. Alario, J. Deves, Relation Between Acid and Catalytic Properties of Chlorinated Gamma-Alumina. a 31p Mas Nmr and Ftir Investigation, Oil & Gas Science and Technology, 54 (1999) 537-545.

Appendix A

MATLAB codes for theoretical models

Metal uptake over oxides at different SL

```
%%adsorption of PTA on silica at different SL%%

zads=+2; %Charge of metal precursor complex
SL1=[500 5000 10000 25000 50000]; %surface loading in m2/l
T=298.15; %Temperature
F=9.6485309e4; %Faraday constant%
R=8.31451;
rw=1.35e-10; %radius of H2O
rion=2.41e-10;%Radius of metal complex ion
N=6.02214e23; %Avogadro number
nh=2;
gammamax=1/(N*pi*(rion+2*nh*rw)^2); %maximum adsorption density Equation 6
main text
MWPt=195.06; %Molecular weight of metal
Cinit1=[.08 0.820 0.820*2.5 1.64*2.5 1.64*5]; %initial metal concentrations in solution
for p = 1:5
    SL=SL1(p);
    Cinit=Cinit1(p)/MWPt;
x0=[1e-5 4.25 0.01];
Cio=0.25*Cinit;

for k=1:140

    pHi(k)=k*(1/10);

   options=optimset('display','off','TolX',1e-12,'TolFun',1e-12);

[x]=fminsearch(@phshiftfun_silica_PTA,x0,options,pHi(k),SL,F,T,zads,Cio,Cinit);

pHf(p,k)=x(2); % final pH
y(p,k)=x(3); %surface potential
Y1(p,k)=exp(y(p,k)/2);
CO2(p,k)=x(1);
x0=[x(1) x(2) x(3)];
ka= 4.45e-7; Csys=55.56;
CCO2(p,k)= sqrt(0.01*CO2(p,k)*Csys*ka);
```

```
C=fzero(@Cadsorb_fun_PTA_silica,Cio,options,SL,Y1(p,k),pHf(p,k),T,F,R,gammamax,
Cinit,rw,rion,zads,pHi(k),CCO2(p,k));

while abs(Cio-C)/C>1e-8
      Cio=C;
end

Cads(p,k)=C;
ionic(p,k)=CCO2(p,k)+0.5*(10^(-pHf(p,k))+10^(pHf(p,k)-14)+10^(-
pHi(k))+10^(pHi(k)-14)+zads^2*Cads(p,k)+2*Cinit);
kappa(p,k)=3.31e9*sqrt(ionic(p,k));
psix(p,k)=(2*R*T/F).*log(((Y1(p,k)+1)+(Y1(p,k)-1)*exp(-
kappa(p,k)*(rion+2.*nh*rw)))/((Y1(p,k)+1)-(Y1(p,k)-1)*exp(-
kappa(p,k)*(rion+2*nh*rw))));
delGcoul(p,k)=zads*F*psix(p,k);
Keq(p,k)=exp(-delGcoul(p,k)/(R*T));
gam(p,k)=gammamax*Keq(p,k)*Cads(p,k)/(1+Keq(p,k)*Cads(p,k));
end

figure (1)
plot(pHf(p,1:140),y(p,1:140)','-b');
axis([0 14 -10 4])
title ('potential')
xlabel('pHf','FontSize',20)
ylabel('y=ea*potential/kt','FontSize',20)
hold on
figure (2)
plot(pHf(p,1:140),1e6*gam(p,1:140)','-b');
axis([0 14 0 1])
title ('uptake')
xlabel('pHf','FontSize',20)
ylabel('Uptake[micromoles/m2]','FontSize',20)
hold on
grid on
figure (3)
plot(pHf(p,1:140),ionic(p,1:140)','-b');
title('ionic strength')
axis([0 14 0 3.5])
xlabel('pHf','FontSize',20)
ylabel('ionic strength in mol/liter','FontSize',20)
hold on
figure (4)
plot(pHf(p,1:140),Keq(p,1:140)','-b');
title('Equilibrium constant')
axis([0 14 0 1e5])
xlabel('pHf','FontSize',20)
```

```
ylabel('Keq','FontSize',20)
hold on
figure (5)
plot(pHi,pHf(p,1:140)','-b');
axis([0 14 0 14])
xlabel('pHi','FontSize',20)
ylabel('pHf','FontSize',20)
title('pH shift')
hold on
grid on
end

%% pH shift function %%
function [ f ] = phshiftfun_silica_PTA( x,pHi,SL,F,T,zads,C,Cinit)
k=1.380658e-23; %Boltzman constant%
ea=1.60217733e-19; %charge of electron%
DpK=7.25; %ionization constant
K1 = 10^-(PZC - 0.5*DpK); %intrinsic acidity constants for protonation via
[MOH2(+1)]--->[MOH]+[Hs+]%
K2 = 10^-(PZC + 0.5*DpK); %intrinsic acidity constant for deprotonation via [MOH]---
>[MO-]+[Hs+]%
Ns=5; %density of OH groups.
lambdat=10^(-5)*Ns/6.02; %density of charged sites (moles/m^2)%
LHSdenom=(10^(-x(2))/K1*exp(-x(3))-K2/10^(-x(2))*exp(x(3)));
LHSnom=(10^(-x(2))/K1*exp(-x(3))+1+K2/10^(-x(2))*exp(x(3)));
fugvap= 2.09217e-4; %in atm. Search file fugacity_CO2 and link
http://cdiac.ornl.gov/ftp/cdiac74/sop24.pdf%
Psat=67.10; %in atmosphere, at 25degC, link:
http://www.ohio.edu/mechanical/thermo/property_tables/CO2/CO2_PresSat2.html
Ed=78.41; %dielectric constant%
e0=8.854e-12; %Permittivity of the vacuum(Park & Regalbuto, 1995, JCIS)%
Avogadro=6.02214e23;
C0=1; %standard concentration (mol/liter)%
ka= 4.45e-7; Csys=55.56; %Cys in mol/dm^3:considering air has 0.03% CO2%
CCO2= sqrt(0.01*x(1)*Csys*ka);
I=CCO2+0.5*(10^(-x(2))+10^(x(2)-14)+10^(-pHi)+10^(pHi-14)+zads^2*C);
gammat=10^(+0.3*0.51*I-(-0.51*(I)^0.5)/(1+(I)^0.5));
feqn8=(LHSdenom/LHSnom)*(F*lambdat)-
(8*1e3*Ed*k*e0*T*I*Avogadro)^0.5*sinh(x(3)/2); %Equation 1 and Equation 2
feqn9=(LHSdenom/LHSnom)*(SL*lambdat)-(10^(-pHi)-10^(-(14-pHi))+(10^-(14-x(2))-
10^(-x(2)))*(1/gammat)); %Equation 1 and Equation 3
feqn10=fugvap-x(1)*Psat*gammat; %Equation 4
f=feqn8^2+ feqn9^2+feqn10^2;
end

%Adsorption function%%
```

```
function [ f ] = Cadsorb_fun_PTA_silica(
C,SL,Y,pHf,T,F,R,gammamax,Cinit,rw,rion,zads,pHi,CCO2)
ionic=CCO2+0.5*(10^(-pHf)+10^(pHf-14)+10^(-pHi)+10^(pHi-
14)+zads^2*C+2*Cinit); %ionic strength of solution
kappa=3.31e9*sqrt(ionic); %Equation 10
psix=(2*R*T/(F))*log(((Y+1)+(Y-1)*exp(-kappa*(rion+2*2*rw)))/((Y+1)-(Y-1)*exp(-
kappa*(rion+2*2*rw)))); %Equation 9
delGcoul=zads*F*psix; %Equation 8
Keq=exp((-delGcoul)/(R*T)); %Equation 7
f =-C -(1/Keq+SL*gammamax-Cinit)/2+sqrt((1/Keq+SL*gammamax-
Cinit)^2/4+Cinit/Keq); %Modified Equation 5
end
```

Published with MATLAB® 7.10

Codes for parameter estimation

```
%%Fitting for 3P parameter of high SA alumina%%

x0=[4 8 8];
options=optimset('TolX',1e-12,'TolFun',1e-12);
[x]=lsqnonlin(@findDPKfun_3D,x0,[],[],options);
format longE;
   display(x)
   dpkplots_3D(x);
    findDPKfun_3D(x);
   grid on
```

```
x =

   3.903696025091393e+000   8.010661104835277e+000   8.228997527935706e+000
```

```
%%pH shift function%%

function [ f ] = phshiftfun_alumina_DPK_3D_fun( x,pHi,SL,DpK,Ns,PZC) %SL=surface
loading, pHi=pH initial%
k=1.380658e-23; %Boltzman constant%
ea=1.60217733e-19; %charge of electron%
F=9.6485309e4;
T=298.15; %Temperature
K1 = 10^-(PZC - 0.5*DpK); %intrinsic acidity constants for protonation via
[MOH2(+1)]--->[MOH]+[Hs+]%
```

```
K2 = 10^-(PZC + 0.5*DpK); %intrinsic acidity constant for deprotonation via [MOH]--->[MO-]+[Hs+]%
lambdat=10^(-5)*Ns/6.02; %density of charged sites (moles/m^2)%
LHSdenom=(10^(-x(2))/K1*exp(-x(3))-K2/10^(-x(2))*exp(x(3)));
LHSnom=(10^(-x(2))/K1*exp(-x(3))+1+K2/10^(-x(2))*exp(x(3)));
fugvap= 2.09217e-4; %in atm. Search file fugacity_CO2 and link http://cdiac.ornl.gov/ftp/cdiac74/sop24.pdf%
Psat=67.10; %in atmosphere, at 25degC, link: http://www.ohio.edu/mechanical/thermo/property_tables/CO2/CO2_PresSat2.html
Ed=78.41; %dielectric constant%
e0=8.854e-12; %Permittivity of the vacuum(Park & Regalbuto, 1995, JCIS)%
Avogadro=6.02214e23;
C0=1; %standard concentration (mol/liter)%
ka= 4.45e-7; Csys=55.56; %Cys in mol/dm^3:considering air has 0.03% CO2%
CCO2= sqrt(0.01*x(1)*Csys*ka);
I=CCO2+0.5*(10^(-pHi) + 10^(pHi-14)+10^(-x(2))+10^(x(2)-14));
gammat=10^(-0.510*(sqrt(I)/(1+sqrt(I))));
feqn8=(LHSdenom/LHSnom)*(F*lambdat)-(8*1e3*Ed*k*e0*T*I*Avogadro)^0.5*sinh(x(3)/2); %Equation 1 and Equation 2
feqn9=(LHSdenom/LHSnom)*(SL*lambdat)-(10^(-pHi)-10^(-(14-pHi))+(10^-(14-x(2))-10^(-x(2)))*(1/gammat)); %Equation 1 and Equation 3
feqn10=fugvap-x(1)*Psat*gammat; %Equation 4
f=feqn8^2+ feqn9^2+feqn10^2;
end
```

```
%Function for parameter fitting%

function [ f3,f4] = findDPKfun_3D(para )
pHiexpt50k = [1.09 1.99 2.99 4.02 5 5.46 7.63 10.75 11.93 12.99];
pHfexpt50k = [4.05 7.1 8.02 8.16 8.18 8.19 8.18 8.28 9.09 11.65];
pHiexpt12k = [1.02 2.00 3.00 4.06 4.97 5.68  7.22 10.72 11.83 12.93];
pHfexpt12k = [3.82 6.18 7.98 8.25 8.27 8.32 8.35 8.60 9.87 12.55];
SL12k=12500;
SL50k=50000;
for i=1:10
  pHi50k(i)=pHiexpt50k(i);
  pHi12k(i)=pHiexpt12k(i);
options=optimset('display','off','TolX',1e-12,'TolFun',1e-12);
x0=[1e-5 8.3 0.01]; %initial guess for x. Use 3.5 for silica. Not sure whether that matters%
[y]=fminsearch(@phshiftfun_alumina_DPK_3D_fun,x0,options,pHi12k(i),SL12k,para(1),para(2),para(3));
[z]=fminsearch(@phshiftfun_alumina_DPK_3D_fun,x0,options,pHi50k(i),SL50k,para(1),para(2),para(3));
pHfinal50k(i)=z(2);
pHfinal12k(i)=y(2);
```

```
%f(i)=abs((pHfinal50k(i)-pHfexpt50k(i))/14)+abs((pHfinal12k(i)-pHfexpt12k(i))/14);
f1(i)=abs((pHfinal50k(i)-pHfexpt50k(i))/14);
f2(i)=abs((pHfinal12k(i)-pHfexpt12k(i))/14);
end
f3=sum(f1)*100/10;
f4=sum(f2)*10;

end
```

```
%Function for final data plot%

function f=dpkplots_3D(para)%1-DPK,2-PZC,3-Ns
pHiexpt50k = [1.09 1.99 2.99 4.02 5 5.46 7.63 10.75 11.93 12.99];
pHfexpt50k = [4.05 7.1 8.02 8.16 8.18 8.19 8.18 8.28 9.09 11.65];
pHiexpt12k = [1.02 2.00 3.00 4.06 4.97 5.68  7.22 10.72 11.83 12.93];
pHfexpt12k = [3.82 6.18 7.98 8.25 8.27 8.32 8.35 8.60 9.87 12.55];
SL12k=12500;
SL50k=50000;
for i=1:70
   pHi(i)=i/5;
options=optimset('display','off','TolX',1e-12,'TolFun',1e-12);
x0=[1e-5 8.3 0.01]; %initial guess for x. Use 3.5 for silica. Not sure whether that
matters%
[y]=fminsearch(@phshiftfun_alumina_DPK_3D_fun,x0,options,pHi(i),SL12k,para(1),pa
ra(2),para(3));
[z]=fminsearch(@phshiftfun_alumina_DPK_3D_fun,x0,options,pHi(i),SL50k,para(1),par
a(2),para(3));
phfinal12k(i)=y(2);
phfinal50k(i)=z(2);
end
subplot(2,1,1)
plot(pHi,phfinal50k,pHiexpt50k,pHfexpt50k,'o')
title('SL=50,000 m^2/l')
grid on
subplot(2,1,2)
plot(pHi,phfinal12k,pHiexpt12k,pHfexpt12k,'o')
title('SL=12.5k m^2/l')
grid on
end
```

Published with MATLAB® 7.10

Codes for 2-surface model (Low SA alumina and High SA silica)

```
% Codes for PZC of mixed oxide %
for k=1:41 % wt fraction of Al2O3 at 5% interval%
  wtpAl(k)=2.5*(k-1)/100;
   wtpSi(k)=1-wtpAl(k);
fAl(k)=33*8.02*2.5*(k-1)/(33*8.02*2.5*(k-1)+182*5.04*(100-2.5*(k-1))); % Equation
2.5
fSi(k)=1-fAl(k);
sigma=0;
pzcmixexpt=[3.97 5.4 5.79 6.48 6.93  7.44 7.76 8.19]'; %Experimental PZC values
S_Alexpt=[0 10 20 40 60 80 90 100]';%Alumina surface coverage used in expt
wtpAlexpt=(S_Alexpt/33)./((S_Alexpt/33)+((100-S_Alexpt)/182)); %mass fraction of
alumina used in expt

   for i=1:350
  pHf(i)=i*(1/25);   %pHf vales from 0.1 to 14 at 0.1 interval
   options=optimset('display','off','TolX',1e-10);
   x0Al=[0.1 0.1 ]; %initial guess for xAl%
   x0Si=[0.1 0.1 ]; %initial guess for xSi%
   [xAl]=fminsearch(@phshiftfun_alumina_mix_HALS,x0Al,options,pHf(i)); %Solving
for charge and potential of Al2O3
   [xSi]=fminsearch(@phshiftfun_silica_mix_HALS,x0Si,options,pHf(i)); %Solving for
charge and potential of SiO2
sigma_Al=xAl(1);
sigma_Si=xSi(1);
sigmat=fAl(k)*sigma_Al+fSi(k)*sigma_Si;
       if sigmat*sigma<0   % Tracking down PZC value
       break
       end
       sigma=sigmat;
   end
      pzcmix(k)=pHf(i);
 figure (1)
p=plot(wtpAl,pzcmix,'-',wtpAlexpt,pzcmixexpt,'x');
set(p, 'color','blue')
axis([0 1 3 9])
grid on
xlabel('mass fraction of Alumina','FontSize',24)
ylabel('PZC','FontSize',24)
hold on
end
```

Published with MATLAB® 7.10

```
%Determination of Surface coverage%

S_Alexpt=[0 0.1 0.2 0.4 0.6 0.8 0.9 1.0]'; %surface fraction% of Alumina used in expt
wtpAlexpt=(S_Alexpt/33)./((S_Alexpt/33)+((1-S_Alexpt)/182));
pzcmixexpt=[3.97 5.4 5.79 6.48 6.93  7.44 7.76 8.19]';
x0Al=[0.1 0.1]; %initial guess for xAl%
   x0Si=[0.1 0.1]; %initial guess for xSi%
for n=1:8
options=optimset('display','off','TolX',1e-10);
   pzcmixpt(n)=pzcmixexpt(n);
   [xAlexpt]=fminsearch(@phshiftfun_alumina_mix_HALS,x0Al,options,pzcmixpt(n));
%Solving for sigma0 and psi0 of Al2O3
   [xSiexpt]=fminsearch(@phshiftfun_silica_mix_HALS,x0Si,options,pzcmixpt(n));
%Solving for sigma0 and psi0 of SiO2
   XSiexpt(n)=xSiexpt(1)/(pzcmixpt(n)-3.47);
   XAlexpt(n)=xAlexpt(1)/(pzcmixpt(n)-8.36);
   Zmodelexpt(n)=(XSiexpt(n)/XAlexpt(n)).*5.04./8.05; %Equation 2.8
   ASCexpt(n)=(Zmodelexpt(n).*((pzcmixexpt(n)-3.47)./(8.36-pzcmixexpt(n)))+1).^-1;
%Equation 2.7
end
wtpAl=linspace(0,1,41);
SL_Al=wtpAl*33./(wtpAl*33+(1-wtpAl)*182);
figure (1)
plot(wtpAl,SL_Al,'-r',wtpAlexpt,(1-ASCexpt),'o')
```

Published with MATLAB® 7.10

```
%pH shift function for alumina%

function [ f ] = phshiftfun_alumina_mix_HALS( x,pHf)
T=298; %Temperature
k=1.38066e-23; %Boltzman constant%
ea=1.6e-19; %charge of electron%
DpK=4.65; %From 3P parameter fitting
PZC=8.36; %From 3P parameter fitting
K1 = 10^-(PZC - 0.5*DpK);
K2 = 10^-(PZC + 0.5*DpK);
F=9.649e4; %Faraday constant%
Ns=8.05; %From 3P parameter fitting
lambdat=10^(-5)*Ns/6.02; %density of charged sites (moles/m^2)%
LHSdenom=(10^(-pHf)*exp(-ea*x(2)/(k*T))/K1)-(K2*exp(ea*x(2)/(k*T))/10^(-pHf));
%see eqn 6%
LHSnom=(10^(-pHf)*exp(-ea*x(2)/(k*T))/K1)+1+(K2*exp(ea*x(2)/(k*T))/10^(-pHf));
%see eqn 6%
feqn6=x(1)-(LHSdenom/LHSnom)*(F*lambdat); %the areal surface charge,
sigma0(C/m^2) expressed in terms of the charged groups%
```

```
fugvap= 2.09217e-4;
Psat=67.10;
Ed=78.41; %dielectric constant%
e0=8.854e-12; %Permittivity of the vacuum(Park & Regalbuto, 1995, JCIS)%
Avogadro=6.022e23;
I=0.5*(10^(-x(2)) + 10^(x(2)-14)+10^(-pHf)+10^(pHf-14));
gammat=10^(-0.510*(sqrt(I)/(1+sqrt(I)))); %activity coefficient from extended Debye
Huckel equation%
feqn8=x(1)-sqrt(8*Ed*e0*1e3*k*Avogadro*T*I)*sinh(ea*x(2)/(2*k*T)); % see equation
8%
f=feqn6^2+feqn8^2;
end

%pH shift function for silica%

function [ f ] = phshiftfun_silica_mix_HALS( x,pHf)
T=298; %Temperature
k=1.38066e-23; %Boltzman constant%
ea=1.6e-19; %charge of electron%
DpK=6.84; %From 3D parameter fitting
PZC=3.47;%From 3D parameter fitting
K1 = 10^-(PZC - 0.5*DpK);
K2 = 10^-(PZC + 0.5*DpK);
F=9.649e4; %Faraday constant%
Ns=5.04; %From 3D parameter fitting
lambdat=10^(-5)*Ns/6.02; %density of charged sites (moles/m^2)%
LHSdenom=(10^(-pHf)*exp(-ea*x(2)/(k*T))/K1)-(K2*exp(ea*x(2)/(k*T))/10^(-pHf));
LHSnom=(10^(-pHf)*exp(-ea*x(2)/(k*T))/K1)+1+(K2*exp(ea*x(2)/(k*T))/10^(-pHf));
feqn6=x(1)-(LHSdenom/LHSnom)*(F*lambdat); %the areal surface charge,
sigma0(C/m^2) expressed in terms of the charged groups%
fugvap= 2.09217e-4;
Psat=67.10;
Ed=78.41; %dielectric constant%
e0=8.854e-12; %Permittivity of the vacuum(Park & Regalbuto, 1995, JCIS)%
Avogadro=6.022e23;
ka= 4.45e-7; Csys=55.56;
I=0.5*(10^(-x(2)) + 10^(x(2)-14)+10^(-pHf)+10^(pHf-14));
gammat=10^(-0.510*(sqrt(I)/(1+sqrt(I)))); %activity coefficient from extended Debye
Huckel equation%
feqn8=x(1)-sqrt(8*Ed*e0*1e3*k*Avogadro*T*I)*sinh(ea*x(2)/(2*k*T)); % see equation
8%
f=feqn6^2+feqn8^2;
end
```

Published with MATLAB® 7.

Appendix B

XPS enigma: Where is the alumina

In Figure 2.5 of the main text, surface coverage of physically mixed oxides determined from XPS has been included in only one of the three subplots for comparison with model's prediction. However, for HH and HL physical mixture sets containing higher surface area of porous alumina (SBa200), XPS yielded unusually low alumina signal. As a result, alumina composition of those physical mixtures from XPS analysis turned out to be reasonably low. This discrepancy or disappearance of alumina from XPS could be observed in Figure B.1. For LA-HS physical mixture set (Low SA alumina + High SA silica) one could see that XPS could quite accurately predict the surface composition. However, for HA-HS set (High SA alumina + High SA silica) XPS exhibited drastically lower composition of alumina. Disappearance of alumina from XPS was still recorded when physical mixtures were prepared using SBa200 alumina with other oxides (e.g., Titania) as shown in Figure B.2. Even when, physical mixture was prepared with meshed particles which were subsequently pelletized or calcined no improvement in alumina signal could be recorded (Figure B.3). Genesis of such low XPS intensity from Al in the porous HA support remained a mystery although both XRD (Figure B.4) and 2-surface model (showed in main text). were able to detect its presence at varying composition in a physical mixture. List of components and their abbreviations used in this study has been listed in Table B.1.

Table B.1. List of silica and alumina samples used.

Nature	Name & Manufacturer	BET m^2/g	Abbvr.
Pure	High surface area silica (Aerosil, TT600)	182	HS
Pure	High surface area alumina (Sasol, SBa200)	157	HA
Pure	Low surface area silica (Aerosil, OX50)	50	LS
Pure	Low surface area alumina (Sasol, APA0.2)	40	LA
Pure	High surface area titania (Hombikat, UV100)	345	HT
Pure	Low surface area titania (P25)	45	LT
Phys mix	Physical mixture of HA and HS	-	HA-HS
Phys mix	Physical mixture of LA and HS	-	LA-HS

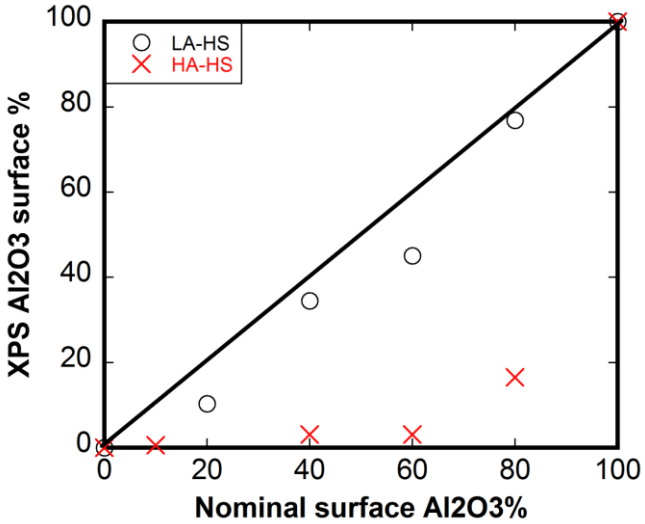

Figure B.1. Discrepancy in XPS estimation when HA is present in physical mixtures of silica and alumina.

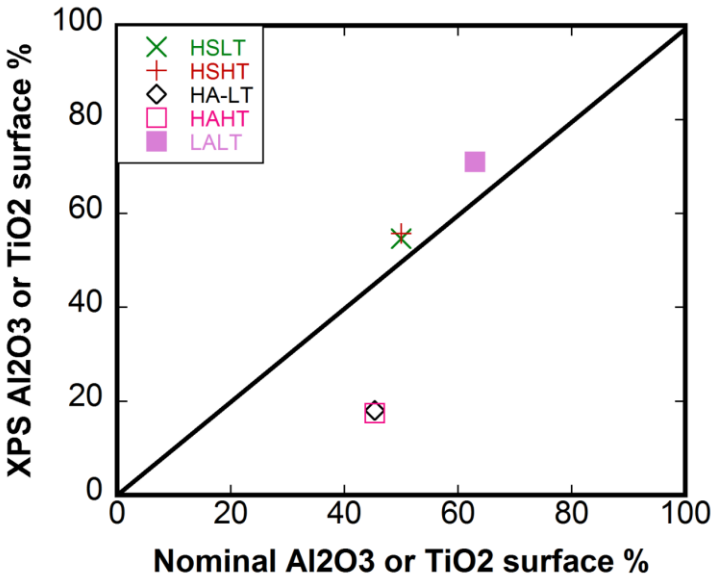

Figure B.2. XPS estimation of surface coverage of silica-titania and alumina-titania physical mixtures. HA alumina with titania once again showed significant discrepancy.

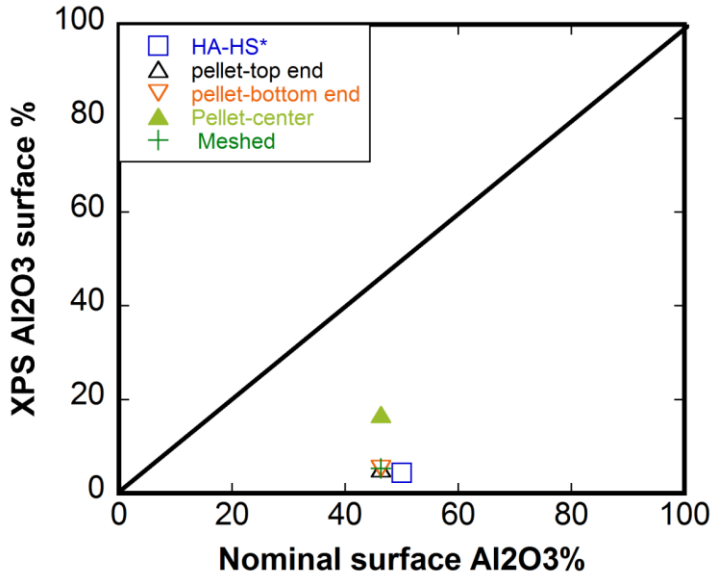

Figure B.3. Discrepancy between nominal and XPS surface coverage for pretreated HA: HA-HS* = HA pretreated at 1200°C for 24h. Surface area reduced from 159 to 40m^2/g. Pellet-top/bottom/center = HA-HS physical mixtures pelletized and surface of the pellet gradually scraped off to expose surface at different depths. Meshed = HA and HS meshed between 75-105micron size and physically mixed.

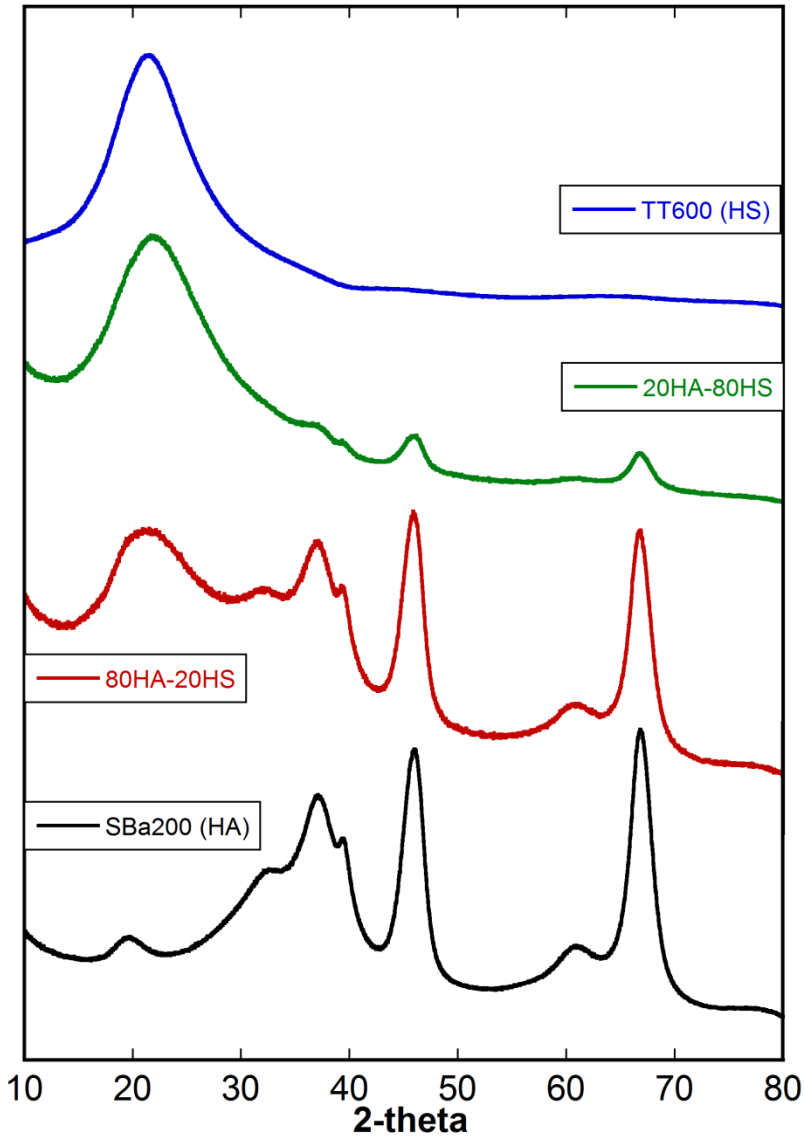

Figure B.4. XRD patterns of different compositions of HA-HS with intensities of silica and alumina peaks commensurate with respective composition. Nominal surface compositions [wt%] are included with each label.

Both XPS and SIMS were performed on HA alumina. XPS spectrum of HA alumina presented in Figure B.5 showed very weak signal from Al2s and Al2p in comparison with LA (low surface area alumina). Similar observation was also noted from SIMS (Figure B.6). Also upon deconvulating O1s peaks of 80% HA-20% HS physical mixture sample one could see that the O1s signal contributed by Al is significantly lower

than that by Si (Figure B.7). Since this physical mixture contained 80% alumina by surface a significantly higher O1s signal intensity coming from Al was anticipated. On the other hand, with LA, O1s peak contributions from Al and Si were quite commensurate to the composition i.e., 40% alumina (LA) and 60% silica (LS) as seen in Figure B.7.

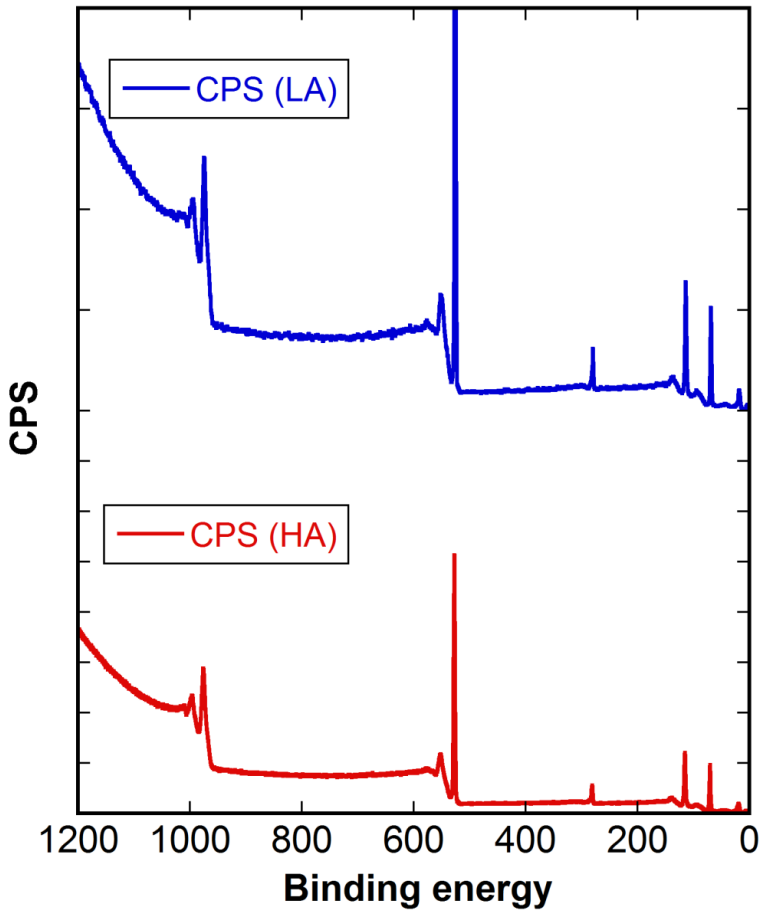

Figure B.5. XPS spectra of HA and LA alumina showing significantly low Al2p and Al2s signal intensity (Counts per second, CPS) for HA.

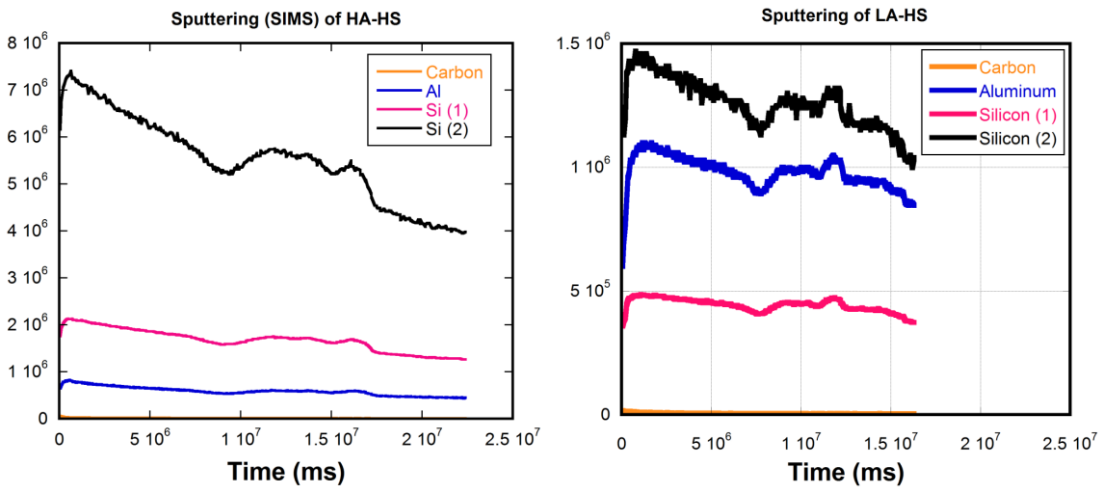

Figure B.6. SIMS plots of HA-HS (left) and LA-HS (right) physical mixtures showing low Al signal in HA-HS.

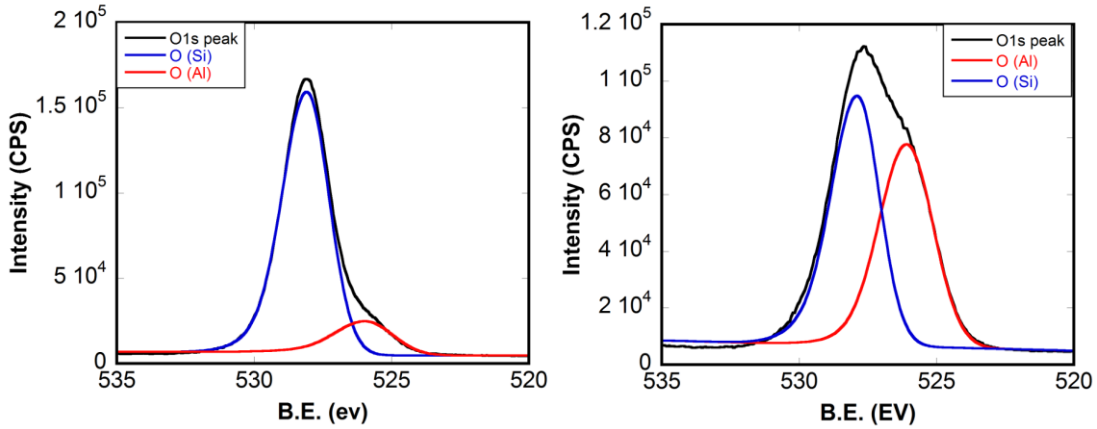

Figure B.7. Deconvulation of O1s peaks of (left) HA-HS (80% alumina by surface) and (right) LA-HS (40% alumina by surface) physical mixture showing contributions from Al and Si.

Appendix C

Anionic platinum adsorption on boehmite

SEA application on boehmite support has been studied here and compared to a γ-alumina support (SBa200). At first, the PZC of boehmite (Catapal B, SA=240m^2/g. Sasol) was measured using EPHL method with 3 pH points. PZC of boehmite was found to be 6.9±0.3. Upon calcination at 550°C for 3h, boehmite completely transformed to γ-alumina (Figure C.1). After calcination the PZC of the calcined boehmite was elevated to 7.3. However, this value was nearly one pH unit lower than the PZC of typical γ-alumina (e.g., 8.3 for SBa200 alumina).

Adsorption uptake survey of anionic $PtCl_6^{2-}$ precursor was studied over uncalcined and calcined (550°C/3h) boehmite at SL=1000m^2/l. From the results, summarized in Figure C.2, it is evident that uptake versus pH_f plots of both calcined and uncalcined boehmite are fairly identical to γ-alumina (results included in Figure C.2 for comparison).

Finally metal dispersion and particle size of 2% Pt ($PtCl_6^{2-}$)/boehmite was measured using XRD (Figure C.1) and H_2 pulse chemisorption. Unlike Pt/γ alumina catalysts, particle size over Pt/boehmite catalysts was reasonably larger. Surprisingly, even when boehmite was calcined and fully transformed to γ-alumina, Pt dispersion on the resulting support (C-Boh) did not improve.

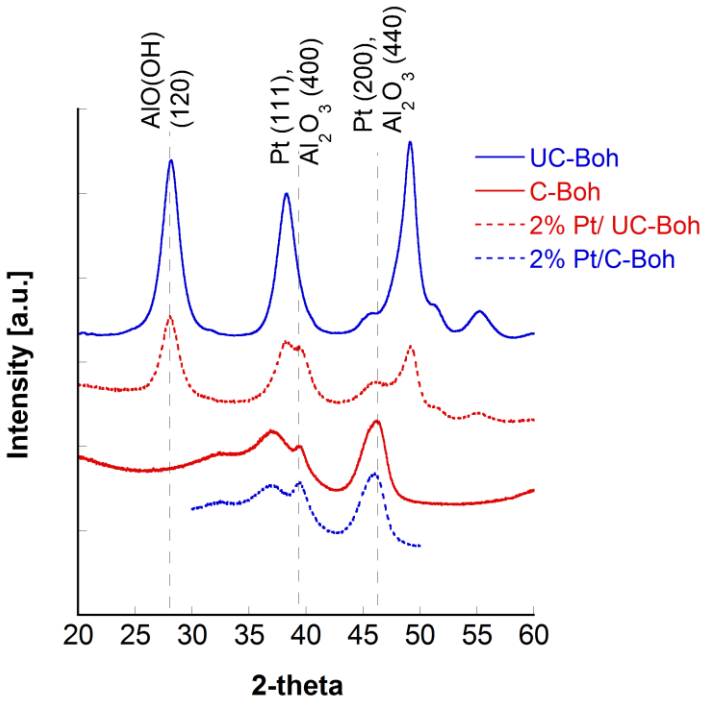

Figure C.1. XRD patterns of different Pt-free and Pt-loaded uncalcined (UC-Boh) and calcined (C-Boh) samples.

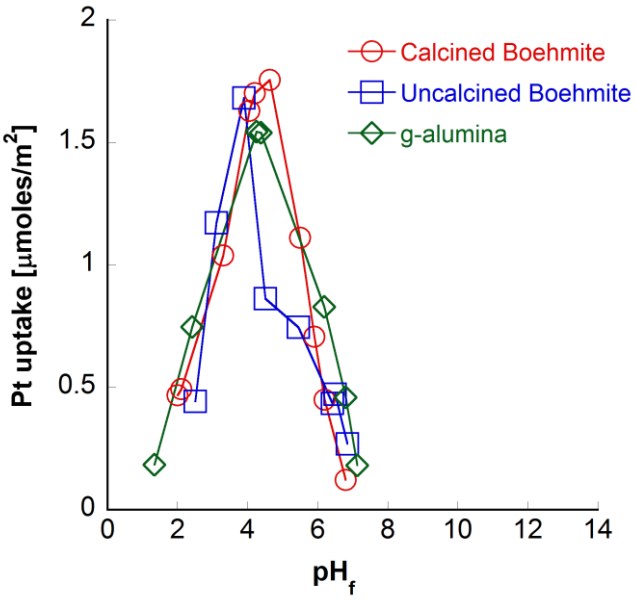

Figure C.2. $PtCl_6^{2-}$ adsorption uptake survey over uncalcined and calcined boehmite and γ-alumina.

Appendix D

Further characterization on aluminosilicates

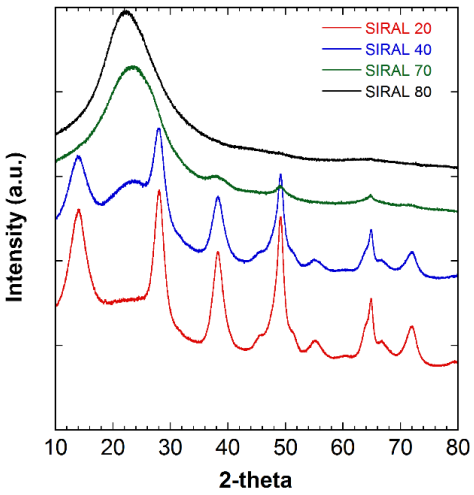

Figure D.1. XRD patterns of uncalcined (prior to activation to γ-alumina phase) SIRAL Al-Si composites showing presence of boehmite phase. Post-calcination patterns are included in main text.

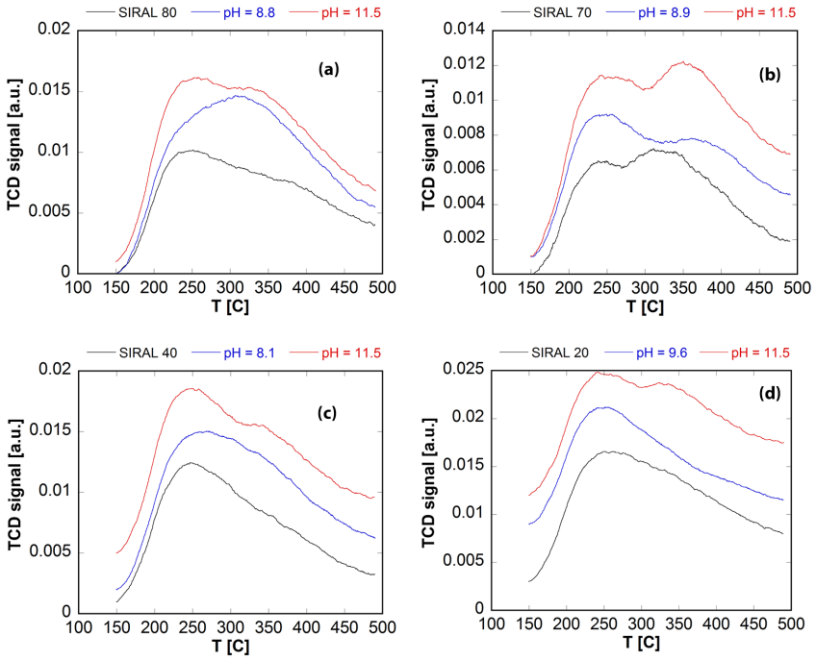

Figure D.2. NH_3-TPD patterns of SIRAL 80 –SIRAL 20 treated at different pH.

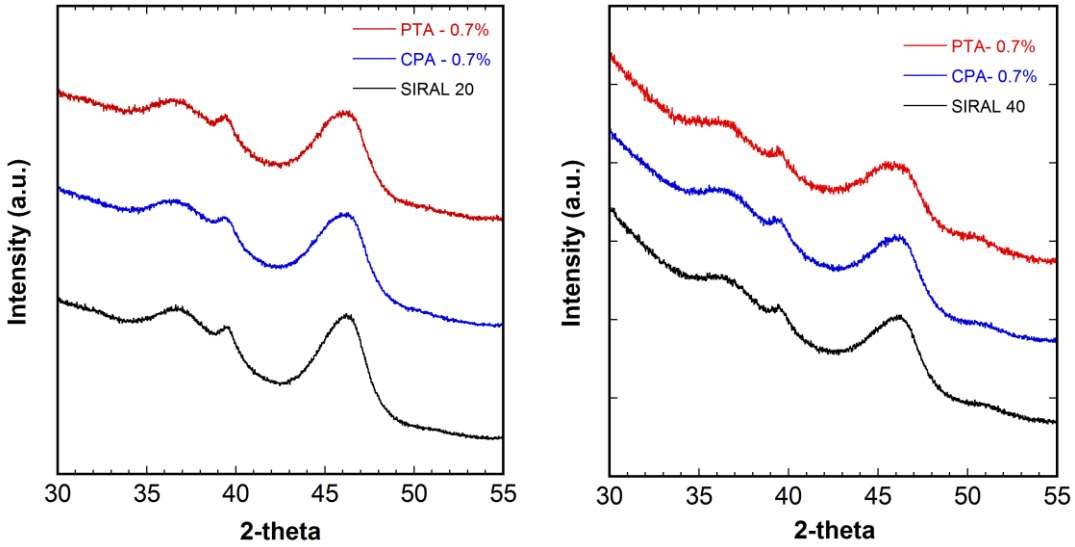

Figure D.3. XRD patterns of Al-rich SIRAL composites and catalysts synthesized over them.

Appendix E

Additional STEM images

$PtCl_6^{2-}$ on AlSi-50 (Figure 3.9b)

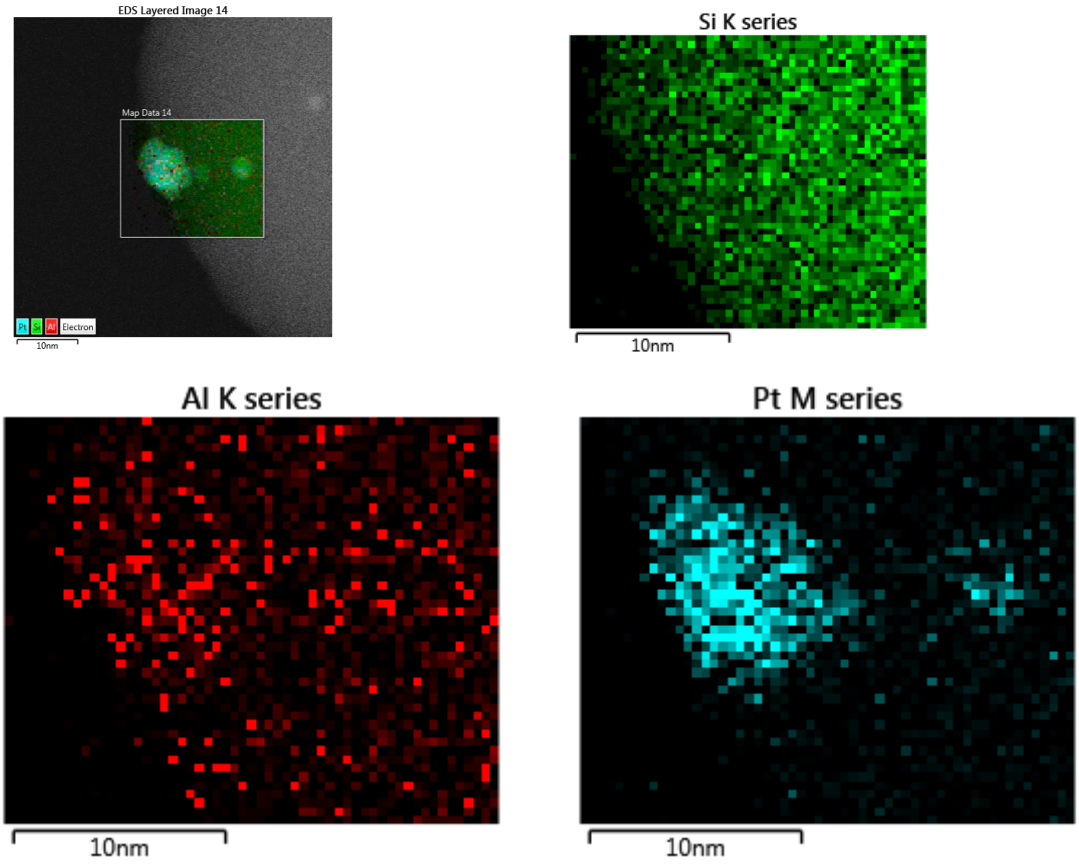

Figure E.1. Elemental mapping image # 1

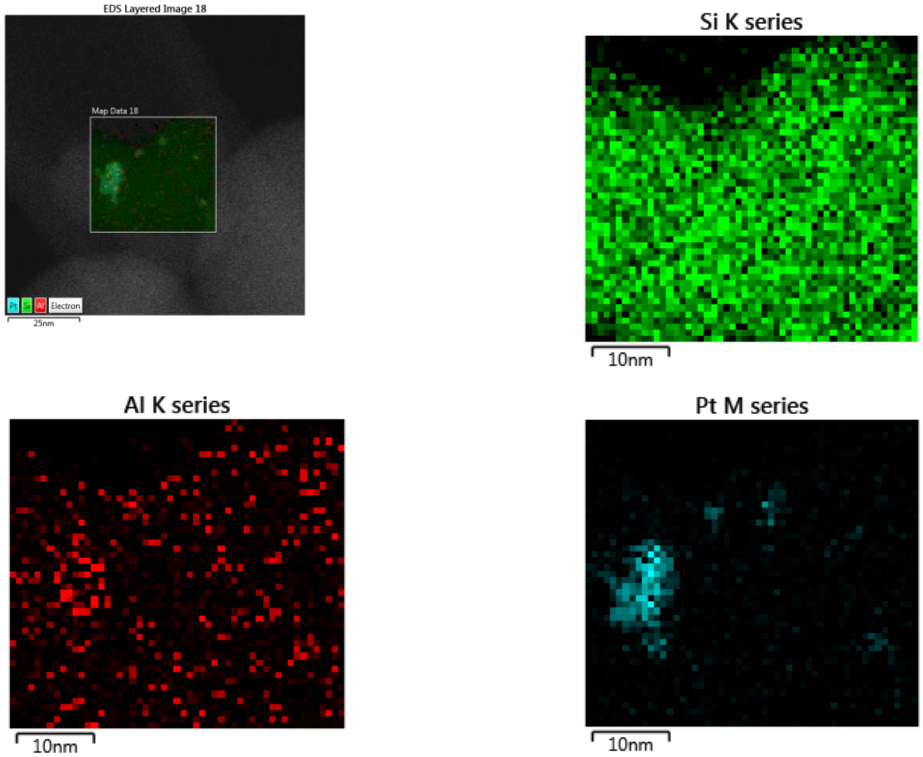

Figure E.2. Elemental mapping image # 2

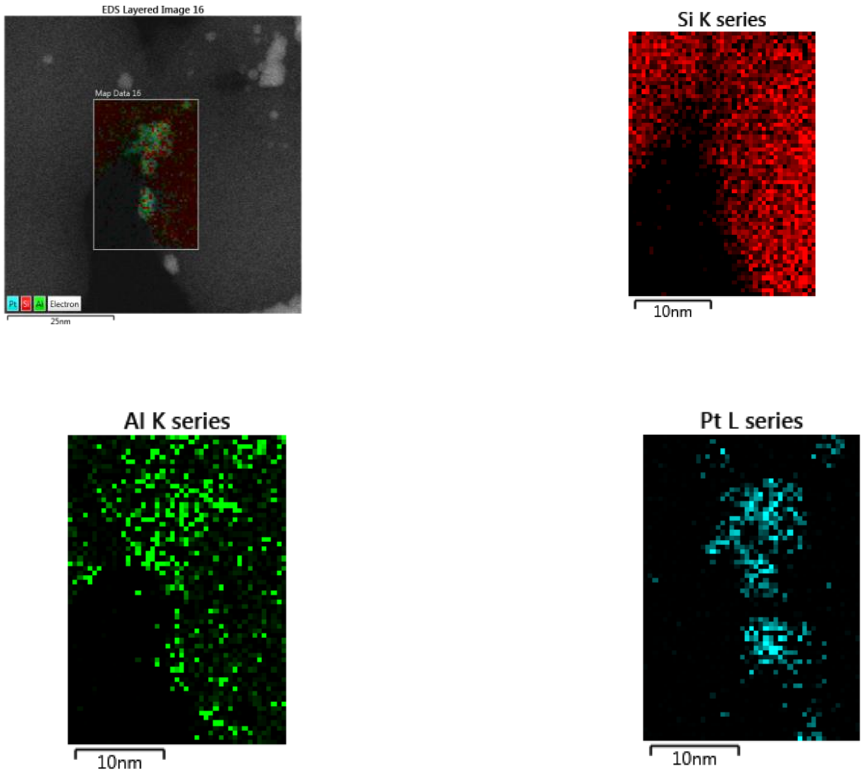

Figure E.3. Elemental mapping image # 3.